

**TECHNICAL QUARTERLY PROGRESS REPORT**

Prepared By

***Advanced Gas Turbine Systems Research***  
Clemson University Research Foundation

For

U. S. Department of Energy  
National Energy Technology Laboratory

Contract No. DE-FC21-92MC29061

Reporting Period: July 1, 2001 – September 30, 2001

***Advanced Gas Turbine Systems Research***  
South Carolina Institute for Energy Studies  
Clemson, South Carolina

# **Technical Quarterly Progress Report**

Advanced Gas Turbine Systems Research  
Cooperative Agreement DE-FC21MC29061

July 1, 2001 to September 30, 2001

## **SUMMARY**

The activities of the Advanced Gas Turbine Systems Research (AGTSR) program for this reporting period are described in this quarterly report. The report is divided into discussions of Membership, Administration, Technology Transfer (Workshop/Education), Research and Miscellaneous Related Activity. Items worthy of note are presented in extended bullet format following the appropriate heading.

## **MEMBERSHIP**

- At the close of the reporting period, the AGTSR Performing Membership held firm at 100 universities represented in 38 states. No new inquiries were received this reporting period.
- The following IRB Membership fees have been received for CY2001:

<u>Full Member</u>
General Electric
Pratt & Whitney
Rolls Royce
Siemens Westinghouse
Solar Turbines

<u>Associate Member</u>
Parker Hannifin
RAMGEN
Southern Company Services
Woodward FST

- The Associate membership of EPRI is in a state of confusion. Early in the year EPRI advised SCIES they would drop membership. Just prior to the Materials Workshop, SCIES was advised that EPRI would maintain Associate membership. Follow-up with EPRI is now underway.
- No other membership activities occurred during this reporting period.

## **ADMINISTRATION**

- The AGTSR Quarterly Report for the reporting period, April to June 2001 was submitted to NETL on July 31, 2001. The report was submitted via hard copy and disk.
- The Annual AGTSR Program Review was held at NETL on Friday, August 24, 2001. The attendees at this meeting included representatives from the DOE-NETL Product Team and Dr. Richard Wenglarz, AGTSR Program Manager, and Dr. Lawrence P. Golan, Program PI. The focus of this meeting was AGTSR continuation issues, not technical discussion. The discussion of continuation issues focused on:
  - modifying the by-laws to enable broader industry representation on the IRB
  - increasing the number of university performing members
  - increasing the number of industry members and expanding participation of associate members
  - modifying the RFP process and scope to accommodate the DOE technology roadmaps for the NGT Program
  - improving the identification and reporting of successes of the university program, possibly involving the establishment of a panel of experts or a staff addition to SCIES.
- The handout material used at the Annual AGTSR Program review meeting is included as ***Attachment I***. This same information was used for presentation to the IRB and IRB comment requested.
- Normal administrative functions continued throughout the reporting period.

## **TECHNOLOGY TRANSFER (Workshops and Education)**

- The AGTSR Combustion Workshop VII was conducted in Charleston, SC on July 31, August 1 and 2, 2001. This workshop included presentations by representatives of the turbine industry on needed gas turbine combustion research and by university representatives on results of AGTSR sponsored gas turbine combustion research projects. The DOE also presented the status of the Combustion Roadmap for the NGT Program. A gas turbine user panel session with following discussions occurred on the afternoon of July 31. The panelists described field experience and issues concerning the operation of gas turbine combustors. About 69 participants from the government, gas turbine industry, and academia attended the workshop.
- Proceedings for Combustion Workshop VIII are now in the final stages of assembly in preparation for release. The delay in release was caused by a lack of speaker response in submitting presentation material.

- Final preparations were made for the AGTSR Materials Workshop II, co-hosted with Professor Maurice Gell of the University of Connecticut, to be conducted in Greenville, SC on October 8-10, 2001. This workshop is organized for discussion of the DOE Materials Roadmap for the NGT Program, presentations by representatives of the turbine industry on needed gas turbine materials research, and presentations by university representatives on results of AGTSR sponsored gas turbine materials research projects.

The final agenda for the workshop had to was significantly altered due to speaker cancellations and schedule changes caused by company travel restrictions resulting from the economic turndown and the tragic events of September 11. A number of attendees also cancelled their registrations for the same reasons.

- Summary reports for the nine AGTSR Faculty Fellowships at IRB organizations were compiled into a booklet. The Faculty Fellowship booklets were distributed in mid July to IRB Focal Points and the DOE.
- **Table 1** contains a list of the 12 AGTSR Industrial Interns supported this year. The Internships have been completed. AGTSR is waiting for receipt of all intern reports. One Central Florida student, Michael Durham, worked at Siemens Westinghouse Power Corporation, and during his term developed a 5-year project to evaluate advanced cooling methods for turbine airfoils and endwalls between UCF/SWPC.

This was submitted as an AGTSR success story to NETL.

- The Success Stories submitted to NETL during this reporting period are contained in **Attachment II a-b-c**.
- In early May 2001, AGTSR released a request for comment on published AGTSR Success Stories. The IRB comments have been received. Most of the IRB comments on the AGTSR were general, but favorable. For example, one turbine manufacturer stated that “The AGTSR is highly successful, effective approach for maintaining US leadership in producing high performance, high quality, environmentally superior, cost competitive gas turbine engines.” And “AGTSR . . . a proven program that is critical to the future success of US industry and academic.” Another IRB company stated that the AGTSR is “one of the more impressive DOE success stories.” Another gas turbine company responded about the AGTSR that the “most tangible benefit . . . (has been) closer contact with universities, access to student talent and a source of employees.”

Most of the IRB companies did not comment on the individual Success Stories. Only one company commented on numerous (10) Success Stories out of the total of about forty-five (45). Five of the ten projects were rated as successful/significantly beneficial, three were rated moderately successful, and two were rated not reliable/inaccurate. Low ratings might have reflected limited interest by the company in the project subject. Since projects are chosen by gas turbine company consensus, some projects with high overall interest might have a

relatively low priority for one of the companies. The company that rated the 10 projects also commented that “Not every project has been a resounding hit but that is the nature of research . . . winners have certainly made our participation worthwhile.”

Several of the reviewers of the Success Stories recommended quantification of the university project benefits to overall improvements in gas turbines and to society.

## **RESEARCH**

- **Table II** contains a list of the AGTSR research reports issued this reporting period. Copies of all Table II reports are included in **Attachment III**.

- The AGTSR Industrial Review Board (IRB) met on September 20 and 21 at SCIES to short list for awards the proposals in response to the year 2001 RFP No. NGT 01-01. The rankings by the individual companies and the overall IRB rankings as a group had been compiled by SCIES for use as a starting point for the selection process in the IRB meeting. The top ten of the thirty-five (35) proposals that had been received were ranked in order. Four of these proposals are in the technology area of Aero/Heat Transfer, four are in the area of Materials, and two are in the area of Combustion. Each of these three technology areas is represented in the top three ranked proposals.

The budget requirements for the ten ranked proposals are likely beyond the available funding. Consequently, the cutoff for awards to the top ranked projects will depend on the available budget for CY2002. The university principal investigators will be conducted in October to examine their budgets for possible reductions to potentially enable more awards.

- The AGTSR continuation issues discussed with the NETL Product Team were also discussed at the IRB meeting (see Administration – second dot). The IRB was asked for comment on all topics. The AGTSR research for the continuation period will be mostly effected by the desire to follow NETL Roadmaps. No immediate difficulty in focusing research on Roadmaps was observed by the IRB.

## **RELATED MISCELLANEOUS ACTIVITY**

Executive summaries for active AGTSR projects and project abstracts from workshops were provided to Abbie Layne at her request for use in discussions concerning possible collaborations on gas turbine research with the European Union.

# AGTSR Annual Program Meeting

August 24, 2001

U.S. DOE NETL  
Morgantown, WV

---

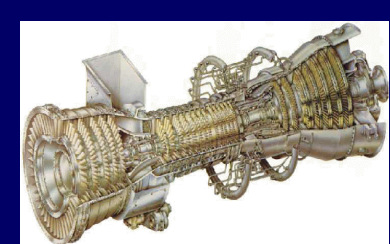
---

**R. Wenglarz, Program Manager**

**L.P. Golan, PI**

**SCIES**

**Tom George, COR**  
**NETL**



# TWO-PHASE AGENDA

---

Review of 2000-2001  
AGTSR Continuation  
Issues



# **REVIEW OF 2000-2001**

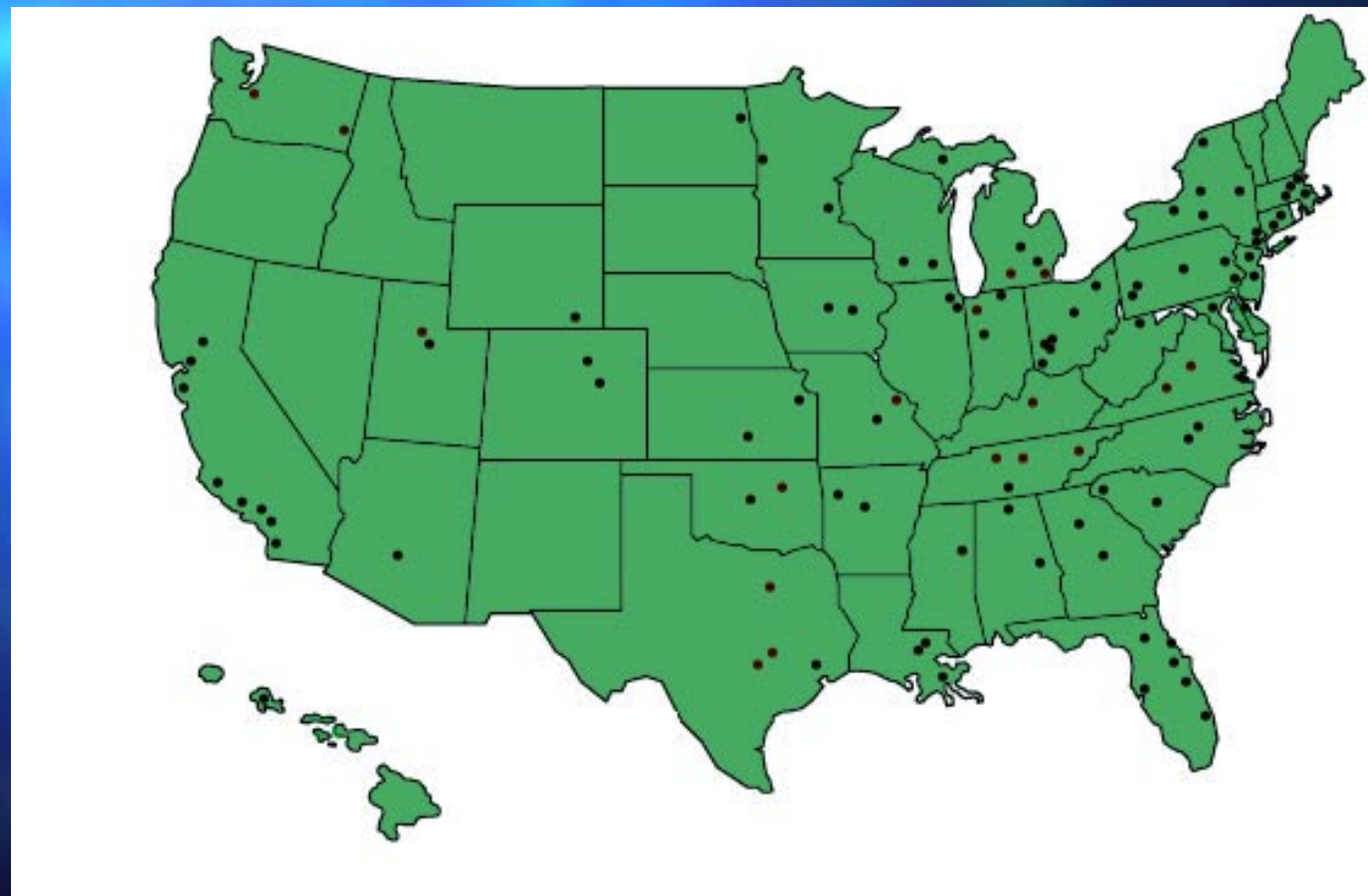
---

- ✓ AGTSR Membership
- ✓ ✓ Administration
- ✓ ✓ ✓ Technology Transfer
- ✓ ✓ ✓ ✓ Research
- ✓ ✓ ✓ ✓ ✓ Related Activities





## AGTSR PERFORMING MEMBERS

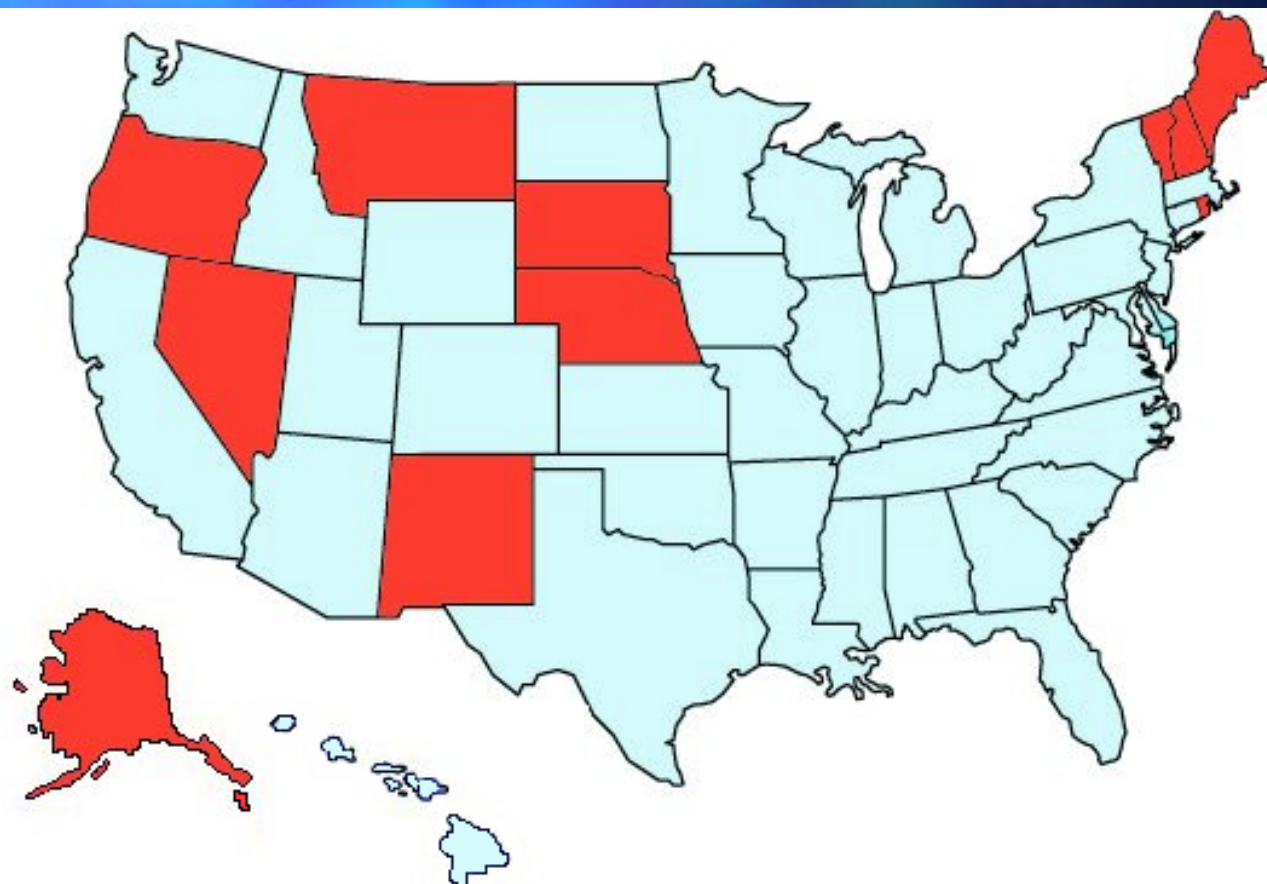




# AGTSR PERFORMING MEMBERS

## NON MEMBER STATES:

Alaska  
Maine  
Montana  
Nebraska  
Nevada  
**New Hampshire**  
New Mexico  
Oregon  
Rhode Island  
South Dakota  
Vermont



# ✓ AGTSR IRB MEMBERS

## VOTING MEMBERS

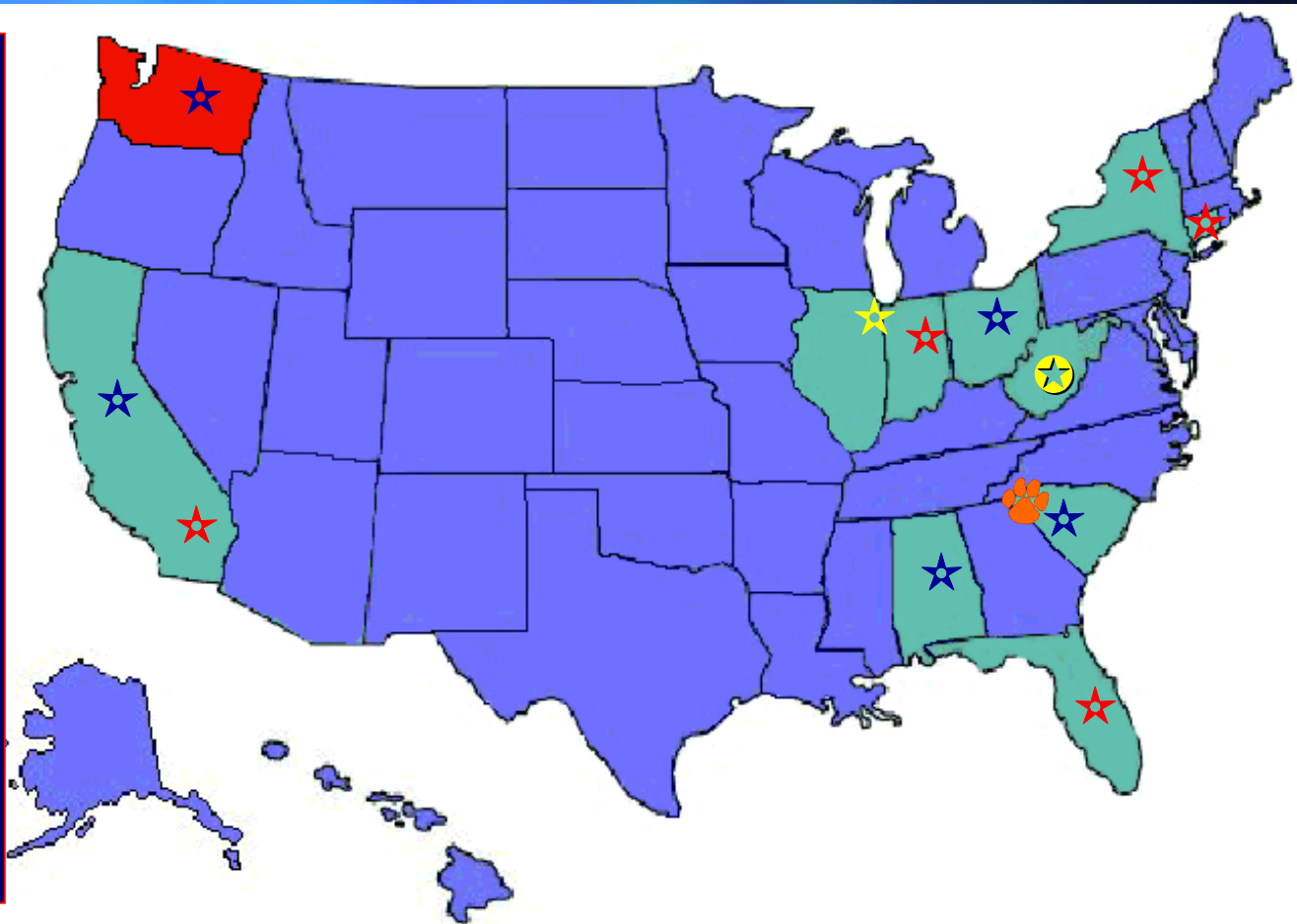
General Electric  
Pratt & Whitney  
Rolls Royce  
Siemens Westinghouse  
Solar Turbines

## ASSOCIATE MEMBERS

EPRI  
Parker Hannifin  
Ramgen Power  
Southern Company  
Woodward FST

## ADVISORS

DOE/NETL  
GTI



# ✓✓ ADMINISTRATION - Personnel

---

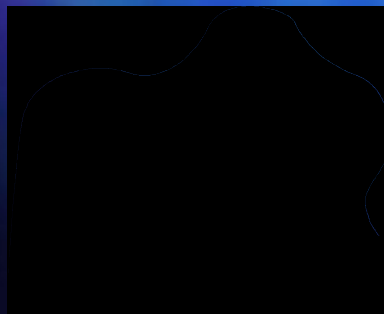
COR Changed

Norm Holcombe to Tom George

SCIES

Leah Hucks - Financial

PI & Program Manager - no change



# ✓ ✓ ADMINISTRATION - Financial

## FINANCIAL OVERVIEW

### (July 31, 2001)

\$

#### INCOME

DOE	34,170,790
IRB	1,307,000
Program	<u>177,181</u>
_____	35,654,971

#### EXPENSES

Administration	5,581,230
Research -	
Requested	29,020,040
Obligated	27,463,090
Expended	25,422,710

(1) Administration (Excluding Project Management) includes:

Workshop/Short Courses	348,635
Interns	453,900
Faculty Fellows	185,912
Special Study	114,680

(2) Research Cost Share - \$542,000; Admin. - \$63,520. Total cost share - \$605,500.



# TECHNOLOGY TRANSFER

---

## Workshops

- Combustion VIII
- Materials II

## Internships

## Faculty Fellowship Booklet

## Success Stories Booklet

## AGTSR Project Report Review by IRB



# RESEARCH

## Status of Existing Projects

### Seven 2000 Awards (RFP 99)

		<u>k\$</u>
UCONN	Materials	285.09
* TEES	AHT	238.63
VIRGINIA	AHT	189.64
* UCI	Combustion	135.94
* PURDUE	Combustion	167.39
N DAKOTA	AHT	193.16
WASHINGTON	Combustion	104.31

\* cost share



# RESEARCH

## Six 2001 Awards (RFP 00)

		<u>k\$</u>
LSU	AHT	228.87
PENN STATE	Combustion	259.39
UCONN	Materials	319.92
UT AT AUSTIN	AHT	324.90
UCSB	Materials	399.25
TEES	AHT	189.25



# RESEARCH - continued

---

## STATUS RFP 01

- 35 proposals received

- 14 heat transfer, 14 combustion, 5 material,  
1 aero, 1 ram

- Schedule

Due date	June 22
SCIES to IRB	June 29
Ranking from IRB	August 10
SCIES to IRB Results	August 24
IRB Meeting at SCIES	September 19-21



# RELATED ACTIVITIES

---

## ESL

**Solar Materials Program Using Mercury 50**

**DG/CHP Conference**

**CoC Meeting Hosted by SCIES**

**GE GT Combustion Tech & Research Symposium**

**ONRL Meeting on US-UK Interaction in Fossil Energy**

**ORNL Invites for Materials Advisory Panels**

## Other

- GTA
- ASERTTI
- CEC
- Oak Ridge

# **AGTSR CONTINUATION ISSUES**

---

**By-Laws**

**University Membership**

**Industrial Membership**

**RFP Process & Scope**

**Identification and Reporting of Successes**

**Key Technical Issues**

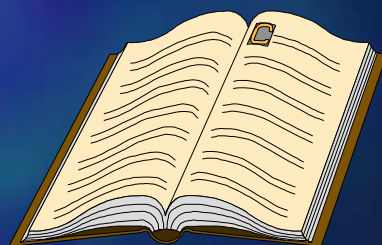
**Process or Project?**



# **BY-LAWS**

---

**Voting Member Requirements  
Expand Base of Associate Members  
Maintain Membership Fees**



# **UNIVERSITY MEMBERSHIP**

---



**Do not change requirements  
Actively seek members in  
non-member states**

# **INDUSTRIAL MEMBERSHIP**

---

**IRB**

**Voting Members**

**Associate Members**

**Expand Base**



# **PERSONNEL EXCHANGE**

---

**Continue Student Internship  
Re-evaluate Faculty Fellowship  
Add Industry Fellowship (??)**



# ESTABLISH UNIVERSITY PANEL OF EXPERTS

---

Purpose: Provide so-what comments on  
research

and

Strengthen critique process for reports

or

Consider staff addition to SCIES

# **KEY TECHNICAL ISSUES**

---

## **CURRENT ISSUES**

- Stable, low emission LPM combustion
- Increased TBC durability/lifetimes
- Reduced rotor tip clearance losses

## **LONGER TERM ISSUES**

- Advanced combustion approaches (TVC, CC)
- New materials (ceramics)
- Advance cooling (mist)

# RFP PROCESS

---

Maintain as is?

**and/or**

Publicize “add on” potential

Develop industry cost-sharing based on  
past successes

Unsolicited proposals

# **PROCESS OR PROJECT?**

---

**PROJECT - Deliverables fixed initially; changes need contract mod**

**PROCESS - Deliverables adapted to changing DOE needs**

**AGTSR more like PROCESS than PROJECT**

Adapted to changing needs

University research topics modified yearly

New activities not in original plan

Windsor Report

Specialized meetings (e.g., Strategic Visioning Workshop)

Faculty Fellowships

Success Stories

**CONTINUATION - PROCESS or PROJECT?**

**Advanced Gas Turbine Systems Research Program**  
**Performing Members**

Air Force Institute of Technology.  
Alabama @ Huntsville, University of  
Arizona State University  
Arkansas, University of  
Arkansas Tech University  
Auburn University  
Brigham Young University  
State University of NY @ Buffalo  
California Institute of Technology  
California @ Berkeley, University of  
California @ Davis, University of  
California @ Irvine, University of  
California, San Diego, University of  
California, Santa Barbara, University of  
Carnegie Mellon University  
Central Florida, University of  
Cincinnati, University of  
Clarkson University  
Clemson University  
Cleveland State University  
Colorado @ Boulder, University of  
Connecticut, University of  
Cornell University  
Dayton, University of  
Delaware, University of  
Denver, University of  
Drexel University  
Duke University  
Embry-Riddle Aeronautical University  
Florida Atlantic University  
Florida Institute of Technology  
Florida, University of  
Georgia Institute of Technology  
Hawaii @ Manoa, University of  
Houston, University of  
Idaho, University of  
Illinois @ Chicago, University of  
Iowa State University  
Iowa, University of  
Kansas, University of  
Kentucky, University of  
Lehigh University  
Louisiana State University  
Maryland @ College Park, University of  
Massachusetts, Lowell, University of  
Mercer University  
Michigan State University  
Michigan Technological University  
Michigan, University of  
Minnesota, University of  
Mississippi State University  
Missouri-Rolla, University of  
MIT (Massachusetts Institute of Technology)  
New Orleans, University of  
State University of NY @ Stony Brook (SUNY)  
North Carolina State University  
North Dakota, University of  
Northeastern University  
Northwestern University  
Notre Dame, University of  
Ohio State University  
Oklahoma, University of  
Pennsylvania State University  
Pittsburgh, University of  
Polytechnic University  
Princeton University  
Purdue University  
Rensselaer Polytechnic Institute  
South Carolina, University of  
Southern University  
Southern California, University of  
South Florida, University of  
Stanford University  
Stevens Institute of Technology  
Syracuse University  
Tennessee, University of Space Institute (UTSI)  
Tennessee, University of  
Tennessee Technological University  
Texas A&M  
Texas @ Arlington, University of  
The University of Texas @ Austin  
Tulsa, University of  
Utah, University of  
Valparaiso University  
Vanderbilt University  
Virginia Polytechnic Institute  
University of Virginia  
Washington University  
Washington, University of  
Washington State University  
Wayne State University  
Western Michigan University  
West Virginia University  
Wisconsin-Madison, University of  
Wisconsin-Milwaukee, University of  
Wichita State University  
Worcester Polytechnic Institute  
Wright State University  
Wyoming, University of  
Yale University

**Advanced Gas Turbine Systems Research Program  
Performing Members**

<b>STATES INVOLVED</b>	<b>STATES NOT INVOLVED</b>
Alabama	Alaska
Arizona	Maine
Arkansas	Montana
California	Nebraska
Colorado	Nevada
Connecticut	New Hampshire
Delaware	New Mexico
Florida	Oregon
Georgia	Rhode Island
Hawaii	South Dakota
Idaho	Vermont
Illinois	
Indiana	
Iowa	
Kansas	
Kentucky	
Louisiana	
Maryland	
Massachusetts	
Michigan	
Minnesota	
Mississippi	
Missouri	
New Jersey	
New York	
North Carolina	
North Dakota	
Ohio	
Oklahoma	
Pennsylvania	
South Carolina	
Tennessee	
Texas	
Utah	
Virginia	
Washington	
West Virginia	
Wisconsin	
Wyoming	

## **AGTSR Points of Contact (POC)**

### **Voting Members:**

#### **GE - Power Generation**

Focal Point: Kathryn Rominger 518-385-0753

<u>Sub Areas</u>	<u>POC</u>	<u>Phone</u>
Combustion (Instability)	*Tony Dean Hukam Mongia	518-387-6478 513-243-2552 (GEAE)
Aero-Optimizaton	Phil Beauchamp Ramani Mani *Kevin Kirtley Phil Andrew	518-385-4933 518-387-6341 518-387-5848 518-385-9328
Materials	Curt Johnson (TBC's) Warren Nelson Mike Henry *Steve Balsone Bob Orenstein	518-387-6421 518-385-3660 518-387-5799 518-387-4141 518-387-4103
Heat Transfer	*Ron Bunker Richard Kehl	518-387-5086
GE - CRD Lab Research	Gene Kimura (mgr.) (oversees all R&D)	518-387-6653
Dynamics (Seals, Bearings)	Imdad Imam	518-387-5043

#### **Pratt & Whitney**

Focal Point: Bill Day 860-610-7228

<u>Sub Areas</u>	<u>POC</u>	<u>Phone</u>
Heat Transfer	*John Calderbank	860-565-2633
Materials	*Kevin Schlichting	860-557-2442
Coatings	Jeanine Marcin Mike Maloney Mladen Trubelja	860-565-4784 561-796-6178 860-565-0249

Combustion	*William Proscia	860-610-7679
Aerodynamics	*John Calderbank	850-565-2633
Sensors & Controls	Bill Lamberti	860-565-9174
Alternative Fuels	Bill Day	860-565-0086

### **Rolls Royce**

Focal Point: Sy Ali 317-230-6864

<u>Sub Areas</u>	<u>POC</u>	<u>Phone</u>
Combustion	Duane Smith *Mohan Razdan M. Anand Sunil James Kumar Abhishek André Marshall	317-230-3683 317-230-6404 317-230-2828 317-230-6195 317-230-3174 317-230-5931
Aero-Optimization	*Bob Delaney Ed Hall	317-230-4624 317-230-3722
Heat Transfer	*John Weaver	317-230-5398
Materials	*Malcolm Thomas Ron Cloyd (single crystals) Subhash K. Naik (TBC's) George Creech Ed Hodge Ray Sinatra	317-230-4545 317-230-6302 317-230-5756 317-230-2269 317-230-2111 317-230-5152
Dynamics	Don Burns Kuk Frey	317-230-2368 317-230-6524
Sensors & Controls	Tom Bonsett Andy Brewington	317-230-3448 317-230-2246

### **Siemens Westinghouse**

Focal Point: \*Ihor Diakunchak 407-736-5115

<u>Sub Areas</u>	<u>POC</u>	<u>Phone</u>
Combustion, Instability Alternate Fuels,	Mike Koenig	407-281-5625

Sensors & Controls	Doug Darling Paul Pillsbury Tom Lippert Anil Gulati Don Newbury	407-249-7638 407-281-2817 412-256-2440 407-281-3316
Materials, Thermal Barriers	Gregg Wagner John Goedjen (TBC's) Steve Sabol	407-281-2362 407-281-5372 407-281-5136
Heat Transfer	Ed North Jim Parsons	407-281-2477 407-249-7511
Aerodynamics	Ihor Diakunchak	407-281-5115
Seals	John Xia	
Bearings	John Brushwood	407-281-5391

### Solar Turbines

Focal Point: \*Eli Razinsky 619-544-5635

<u>Sub Areas</u>	<u>POC</u>	<u>Phone</u>
Sensors & Controls	Tom Burke	619-544-2510
Heat Transfer & Aero	*Hee Koo Moon Eli Razinsky Jerry Stringham Ulrich Stang	619-544-5226 619-544-5198 619-544-2854 619-595-7573
Combustion/ Alternate Fuels	*Ken Smith Mohan Sood Luke Cowell	619-544-5539 619-544-5508 619-544-5916
Materials	*Zaher Mutasim	619-544-5889

### Associate Members:

#### EPRI

Focal Point: \*R. Viswanathan 650-855-2450

## **Parker Hannifin**

Focal Point: \*Michael Benjamin 440-954-8105

<u>Sub Areas</u>	<u>POC</u>	<u>Phone</u>
Combustion	Adel Mansour	440-954-8171
Aero-Optimization	Erlendur Steinthorsson	
Materials	Brad Hartley	
Heat Transfer	Adel Mansour	440-954-8171

## **Ramgen Power Systems**

Focal Point: Rob Steele 425-828-4919, x288

<u>Sub-Areas</u>	<u>POC</u>	<u>Phone</u>
	Blake Chenevert	425-828-4919, x224

## **Southern Company Services**

Focal Point: \*Charles Boohaker 205-257-7537

<u>Sub Areas</u>	<u>POC</u>	<u>Phone</u>
Combustion/Emissions	Charles Boohaker	205-257-7537

## **Woodward FST**

Focal Point: \*George Kalinovich 864-627-7183

<u>Sub-Areas</u>	<u>POC</u>	<u>Phone</u>
	George Kalinovich	864-627-7183

## **Advisors:**

### **DOE**

Tom George  
Abbie Layne  
Bruce Utz

304-285-4825  
304-285-4603  
412-386-5706

### **GTI**

Michael Romanco 773-399-5460

## ATS WORKSHOP EXPENSES

DATE	WORKSHOP	CO-HOST	LOCATION	HOTEL			TOTAL EXPENSES	PROGRAM INCOME	NET EXPENSES
				SERVICES	TRAVEL	SUPPLIES			
Feb-94	Combustion	Vanderbilt	Nashville	\$7,145.32	\$1,492.40	\$676.89	\$9,314.61	\$0.00	\$9,314.61
Mar-95	Heat Transfer	Clemson	Hilton Head	\$11,420.00	\$659.74	\$3,344.73	\$15,424.47	\$0.00	\$15,424.47
Mar-95	Combustion II	Purdue/Allison	Indianapolis	\$10,348.53	\$1,527.88	\$4,676.04	\$16,552.45	\$0.00	\$16,552.45
Feb-96	Materials	DOE HQ	Charleston		\$928.79		\$928.79	\$0.00	\$928.79
Mar-96	Combustion III	UC Irvine	Lake Arrowhead	\$28,707.50	\$3,901.20	\$3,910.45	\$36,519.15	\$25,581.72	\$10,937.43
Apr-96	Sensors & Controls	Oak Ridge	Clemson	\$1,325.80		\$1,003.62	\$2,670.58	\$5,000.00	\$5,000.00
Feb-97	Heat Transfer II	Clemson	Isle of Palm	\$13,680.26	\$406.15	\$3,021.52	\$17,107.93	\$3,240.00	\$13,867.93
Mar-97	Combustion IV	GA Tech	Atlanta	\$10,810.73	\$958.26	\$3,116.20	\$14,885.19	\$6,480.00	\$8,405.19
Jun-97	IGTI Expo		Florida		\$4,980.79	\$800.00	\$2,640.00	\$8,420.79	\$8,420.79
Aug-97	Film-Cooling SC	CU	Clemson	\$1,931.56	\$2,489.63	\$1,222.28	\$4,000.00	\$9,643.47	\$7,900.00
Mar-98	Combustion V	UCBerkeley	San Francisco	\$21,340.51	\$3,400.44	\$931.81	\$4,031.77	\$29,704.53	\$7,410.00
Apr-98	Metallics	Stevens	Hoboken,NJ	\$9,109.00	\$1,739.88			\$10,848.88	\$3,410.00
Jan-99	TBC	UCSantaBarb	Santa Barb,CA	\$11,114.44	\$1,947.35		\$2,408.32	\$15,470.11	\$3,920.00
Mar-99	Strategic Visioning		Austin,TX	\$28,225.65	\$1,085.00	\$770.19	\$1,492.00	\$31,572.84	\$15,050.00
Mar-99	Heat Transfer III	Texas	Austin,TX	\$36,040.91	\$2,768.00	\$1,921.55	\$1,708.00	\$42,438.46	\$18,490.00
Apr-99	Combustion VI	VPI	Virginia	\$16,175.92	\$1,040.59	\$200.00	\$2,905.03	\$20,321.54	\$12,250.00
Sep-00	Combustion VII	UC Berk	Calif	\$19,846.56	\$3,040.30	\$210.84	\$690.86	\$23,788.56	\$28,800.00
Oct-00	Heat Transfer IV	Univ of Minn	Minn	\$11,897.56	\$1,282.31	\$805.95	\$638.20	\$14,624.02	\$15,100.00
Jul-01	Combustion VIII		Charleston, SC	\$24,897.02	\$873.71	\$298.97	\$0.00	\$26,069.70	\$24,550.00
Oct-01	Materials II		Greenville, SC						\$1,519.70

\$348,635.49 \$177,181.72 #####

notes:

Indirect office supp/serv do not appear here, such as phone, copier usage, generic supplies

15-Aug-01  
**Financial Status of AGTSR Subcontracts**  
 RFP93, RFP94, RFP95, RFP6, 97 Interns,  
 RFP97, RFP98, RFP99, RFP00

	Institution	Term in years	End Date	a Requested AGTSR Funding	b	c	d	e
				Obligated to Date	Expenditures to:	a-c Balance	b-c Balance	
<b>RFP93</b>								
c SR007	Cal-Berkeley	3	3/31/97	\$518.20	\$518.20	3/97f	\$0.00	\$0.00
c SR008	Vanderbilt	3	12/31/96	\$862.60	\$862.60	12/96f	\$0.00	\$0.00
c SR009	Purdue	3	2/27/97	\$801.69	\$801.69	2/97f	\$0.00	\$0.00
c SR010	Lehigh	3	12/31/96	\$748.39	\$748.39	12/96f	\$0.00	\$0.00
c SR011	Texas A&M	3	2/28/97	\$585.88	\$585.88	2/97f	\$0.00	\$0.00
c SR012	Penn State	3	12/31/96	\$628.81	\$628.81	12/97f	\$0.00	\$0.00
c SR013	Virginia Tech*	3	3/31/97	\$462.01	\$462.01	3/97f	\$0.00	\$0.00
c SR014	Brigham Young	4	12/31/97	\$1,040.99	\$1,040.99	12/97f	\$0.00	\$0.00
c SR015	LSU	3	2/28/97	\$478.18	\$478.18	2/97f	\$0.00	\$0.00
c SR016	Clarkson	2	3/31/96	\$522.80	\$522.80	3/96f	\$0.00	\$0.00
	<b>Subtotal</b>			<b>\$6,649.55</b>	<b>\$6,649.55</b>		<b>\$0.00</b>	<b>\$0.00</b>
<b>RFP94</b>								
c SR017	MIT	1	8/31/95	\$156.46	\$156.46	7/95f	\$0.00	\$0.00
c SR018	Cornell	2	8/31/96	\$165.70	\$165.70	8/96f	\$0.00	\$0.00
c SR019	Purdue	3	2/28/98	\$675.69	\$675.69	4/98f	\$0.00	\$0.00
c SR020	Cal-Irvine	3	03/31/98	\$529.47	\$529.47	3/98f	\$0.00	\$0.00
c SR021	Minnesota	3	12/31/97	\$670.27	\$670.27	12/97f	\$0.00	\$0.00
c SR022	Central Fla	1	8/18/95	\$73.84	\$73.84	8/95f	\$0.00	\$0.00
c SR023	Carnegie Mellon	3	8/31/97	\$537.37	\$537.37	7/97f	\$0.00	\$0.00
c SR024	Clemson	3	8/31/97	\$601.19	\$601.19	8/97f	\$0.00	\$0.00
c SR025	Wyoming	1	7/15/95	\$69.26	\$69.26	7/95f	\$0.00	\$0.00
c SR026	Michigan State	1	8/31/95	\$178.42	\$178.42	7/95f	\$0.00	\$0.00
c SR027	Georgia Tech	3	4/15/98	\$432.48	\$432.48	4/98f	\$0.00	\$0.00
c SR028	Maryland	3	4/16/98	\$573.14	\$573.14	4/98f	\$0.00	\$0.00
c SR029	Oklahoma	2	6/30/97	\$297.71	\$297.71	6/97f	\$0.00	\$0.00
	<b>Subtotal</b>			<b>\$4,961.00</b>	<b>\$4,961.00</b>		<b>\$0.00</b>	<b>\$0.00</b>
<b>RFP95</b>								
c SR030	Conn	3.5	2/28/99	\$500.00	\$500.00	2/99f	\$0.00	\$0.00
c SR031	Georgia Tech	3	8/31/98	\$571.52	\$571.52	8/98f	\$0.00	\$0.00
c SR032	Penn State	3	2/28/99	\$600.63	\$600.63	1/99f	\$0.00	\$0.00
c SR033	Arizona State	4	1/31/00	\$327.70	\$327.70	1/00f	\$0.00	\$0.00
c SR034	Clemson	4	2/29/00	\$538.04	\$538.04	2/00f	\$0.00	\$0.00
c SR035	Conn	1	5/22/97	\$88.48	\$88.48	5/97f	\$0.00	\$0.00
c SR036	Penn State	3	09/30/00	\$450.00	\$450.00	9/00f	\$0.00	\$0.00
c SR037	Syracuse	2	2/28/98	\$170.97	\$170.97	2/98f	\$0.00	\$0.00
c SR038	MIT	1	8/31/96	\$151.79	\$151.79	8/96f	\$0.00	\$0.00
c SR039	Central Fla	2	3/31/98	\$178.21	\$178.21	3/98f	\$0.00	\$0.00
c SR040	Michigan State	1	12/31/96	\$140.00	\$140.00	12/96f	\$0.00	\$0.00
c SR041	Wyoming	0.25	8/31/96	\$5.50	\$5.50	10/96f	\$0.00	\$0.00
	<b>Subtotal</b>			<b>\$3,722.84</b>	<b>\$3,722.84</b>		<b>\$0.00</b>	<b>\$0.00</b>
<b>RFP96</b>								
SR042	Cleveland State	3	12/12/00	\$313.68	\$313.68	12/00f	\$0.00	\$0.00
c SR043	Wisconsin	3	6/12/00	\$370.56	\$370.56	6/00f	\$0.00	\$0.00
c SR044	Purdue	2	5/12/00	\$204.07	\$204.07	5/00f	\$0.00	\$0.00
c SR045	MIT	3	12/15/00	\$276.98	\$276.98	12/00f	\$0.87	\$0.87
c SR046	Pittsburgh	3	6/12/00	\$500.10	\$500.10	6/00f	\$0.00	\$0.00
SR047	Northwestern	4	6/12/01	\$545.01	\$545.01	03/01f	\$0.00	\$0.00
T SR048	California/Davis	3	06/12/98	\$17.98	\$17.98	1/98f	\$0.00	\$0.00
c SR049	Cornell	3	06/12/00	\$594.22	\$594.22	6/00f	\$0.00	\$0.00
c SR050	Penn State	3	6/12/00	\$317.81	\$317.81	8/99f	\$0.00	\$0.00
	<b>Subtotal</b>			<b>\$3,140.41</b>	<b>\$3,140.41</b>		<b>\$0.87</b>	<b>\$0.87</b>
<b>1997 issued(interns &amp; add-on)</b>								
c SR051	Univ of Buffalo	8/31/97		\$5.50	\$5.50	8/97f	\$0.00	\$0.00
c SR052	USC	8/31/97		\$5.53	\$5.53	7/97f	\$0.00	\$0.00
c SR053	Univ of Washing	9/15/97		\$6.65	\$6.65	9/97f	\$0.00	\$0.00
c SR054	Purdue	8/31/97		\$5.50	\$5.50	8/97f	\$0.00	\$0.00
c SR055	Univ of Arkansas	8/15/97		\$6.91	\$6.91	8/97f	\$0.00	\$0.00
c SR056	Clarkson	12/31/98		\$10.46	\$10.46	11/98f	\$0.00	\$0.00
c SR057	Univ of Cen Flori	8/31/97		\$5.50	\$5.50	8/97f	\$0.00	\$0.00
c SR058	Michigan State	8/31/97		\$6.44	\$6.44	8/97f	\$0.00	\$0.00
c SR059	Univ of Cal-Berk	8/31/97		\$8.25	\$8.25	8/97f	\$0.00	\$0.00
c SR060	Virginia Polytech	8/31/97		\$11.00	\$11.00	8/97f	\$0.00	\$0.00
c SR061	Cal-Berkeley	12/31/97		\$30.04	\$30.04	12/97f	\$0.00	\$0.00
	<b>Subtotal</b>			<b>\$101.78</b>	<b>\$101.78</b>		<b>\$0.00</b>	<b>\$0.00</b>
<b>1998(RFP97)</b>								
SR062	Cal-Irvine	3	12/31/01	\$449.94	\$449.94	9/00f	\$0.00	\$0.00
SR063	CIT	3	06/30/01	\$390.20	\$390.20	01-Jun	\$377.79	\$12.41
c SR064	Purdue	2	07/31/00	\$159.81	\$159.81	7/00f	\$158.23	\$1.58
SR065	VPI	3	04/30/02	\$603.40	\$603.40	01-May	\$532.41	\$70.99

SR066	Ga Tech	3	04/30/02	\$441.00	\$441.00	6/1	\$328.15	\$112.85	\$112.85
c SR067	U Central FL	2	06/30/00	\$198.62	\$198.62	6/00f	\$198.62	\$0.00	\$0.00
SR068	Cal-Santa Barba	3	01/31/01	\$599.94	\$599.94	11/00	\$596.39	\$3.55	\$3.55
SR069	Purdue	3	07/31/01	\$427.94	\$427.94	Jun-01	\$382.36	\$45.58	\$45.58
t SR070	Car Mellon	3	01/31/00	\$374.44	\$374.44	1/00f	\$359.11	\$15.33	\$15.33
SR071	Minn	3	07/31/01	\$600.00	\$600.00	01-Jan	\$570.60	\$29.40	\$29.40
c SR072	CIT(faculty spec)	1	08/31/99	\$25.00	\$25.00	8/99f	\$25.00	\$0.00	\$0.00
SR088	U Pittsburgh	1	07/31/01	\$185.53	\$185.53	12/00	\$6.64	\$178.89	\$178.89
seeSR070	<b>Subtotal</b>			<b>\$4,455.82</b>	<b>\$4,455.82</b>		<b>\$3,985.24</b>	<b>\$470.58</b>	<b>\$470.58</b>

**1999(RFP98)**

SR073	Univ of Conn	3	01/31/02	\$448.66	\$448.66	01-Jun	\$311.38	\$137.28	\$137.28
SR074	UCBerkeley	3	#####	\$185.00	\$130.00	01-May	\$130.00	\$55.00	\$0.00
SR075	GaTech	3	01/31/02	\$449.98	\$449.98	Jun-01	\$348.52	\$101.46	\$101.46
SR076	Miss State Univ	3	#####	\$321.37	\$321.37	Jun-01	\$229.59	\$91.78	\$91.78
SR077	Univ Pittsburgh	3	01/31/02	\$430.64	\$430.64	Jul-01	\$276.88	\$153.76	\$153.76
SR078	PennStateUniv	3	01/31/02	\$450.00	\$450.00	Jun-01	\$330.50	\$119.50	\$119.50
SR079	PennStateUniv	2	#####	\$427.25	\$427.25	Jun-01	\$355.14	\$72.11	\$72.11
SR080	Univ Central Fl	3	01/31/01	\$240.00	\$79.90	7/00	\$39.19	\$200.81	\$40.71
	<b>subtotal</b>			<b>\$2,952.90</b>	<b>\$2,737.80</b>		<b>\$2,021.20</b>	<b>\$931.70</b>	<b>\$716.60</b>

**2000(RFP99)**

SR081	U Conn	2	01/31/02	\$285.09	\$143.04	1/1	\$131.75	\$153.34	\$11.29
SR082CS	TEES	2	03/31/02	\$238.63	\$126.94	01-Jun	\$126.67	\$111.96	\$0.27
SR083	Virginia	2	#####	\$189.64	\$97.72	01-Apr	\$84.83	\$104.81	\$12.89
SR084CS	UCI	2	03/31/02	\$135.94	\$135.94	01-Jun	\$81.94	\$54.00	\$54.00
SR085CS	Purdue	2	#####	\$167.39	\$167.39	01-Jun	\$88.74	\$78.65	\$78.65
SR086	N. Dakota	2	04/31/02	\$193.16	\$103.09	01-May	\$90.77	\$102.39	\$12.32
SR087	Washington	2	06/30/02	\$104.31	\$64.61	4/1	\$35.27	\$69.04	\$29.34
	<b>subtotal</b>			<b>\$1,314.16</b>	<b>\$838.73</b>		<b>\$639.97</b>	<b>\$674.19</b>	<b>\$198.76</b>

**2001 (RFP00)**

SR089	LSU	2	#####	\$228.87	\$114.60	01-Jun	\$3.38	\$225.49	\$111.22
SR090	Penn State	2	#####	\$259.39	\$129.26	06/01	\$89.57	\$169.82	\$39.69
SR091	U Conn	2	#####	\$319.92	\$157.61	06/01	\$29.35	\$290.57	\$128.26
SR092	U Texas at Austi	2	#####	\$324.90	\$160.50		\$0.00	\$324.90	\$160.50
SR093	UCSB	2	#####	\$399.25	\$199.64	06/01	\$75.53	\$323.72	\$124.11
SR094	TEES	2	#####	\$189.25	\$93.55	06/01	\$3.75	\$185.50	\$89.80
	<b>subtotal</b>			<b>\$1,721.58</b>	<b>\$855.16</b>		<b>\$201.58</b>	<b>\$1,520.00</b>	<b>\$653.58</b>

	REQUESTED	OBLIGATED		EXPENDED	BALANCE	BALANCE
<b>GRAND TOTAL ALL</b>	<b>\$29,020.04</b>	<b>\$27,463.09</b>		<b>\$25,422.70</b>	<b>REQUESTED</b>	<b>OBLIGATED</b>
<b>DOE pay</b>	\$28,478.08	\$27,032.82		\$25,125.35	\$3,352.73	\$2,773.89
<b>IRB pay</b>	\$541.96	\$430.27		\$297.35	\$244.61	\$132.92

\* refund rec'd 12/9/99

Notes: These were not research awards: SR041, SR051-SR060, SR072

Total portion of these funds that was for interns: \$91.74

Total portion of these funds that was for faculty fellows: \$25k

## **AGTSR INCOME AND EXPENSE PLAN - BUDGET**

---

08/15/01

## QUARTERLY AND CUMULATIVE PROFILE - \$(000)

	#####				1993				1994				1995				
QTR	3	4	1	2	3	4	1	2	3	4	1	2	3	4	1	2	
<b>INCOME</b>																	
DOE	0	446	0	2032	0	0	0	3993			4800				2800		
IRB	0	0	0	125	25	0	100	0	25	25	25	75	25		125	25	
<b>PROGRAM INCOME</b>																25.6	
TOTAL INC	0	446	0	2157	25	0	100	3993	25	25	25	4875	25	0	125	2851	
CUM INC	446	446	2603	2628	2628	2728	6721	6746	6771	6796	11671	11696	11696	#####	#####	#####	
<b>EXPENSES</b>																	
ADM	15	103	98	64	60.8	60.8	60.8	60.8	62.7	62.7	88.5	58.5	57.1	54.8	54.2		
INDIRECT	7	46	44	29	22.6	22.6	22.7	25.8	27.2	27.2	39.7	30.1	26.2	25.2	25		
CONTRACT INDIREC					110				150					126.5			
Cost Share -Salary																	
TOTAL ADM	0	22	149	142	93	193	83.4	83.5	86.6	239.9	89.9	128.2	88.6	209.8	80	79.2	
<b>CONTRACTS</b>																	
93				76	260	385	482	710	379.9	472	555.7	744.9	164.8	317	421		
94							29.1	261	358.1	306	519.4	556.6	63.7	475	313		
95												8.4	20	334	416		
96																	
97																	
98																	
99																	
00																	
00-Cost Share																	
01																	
TOTAL CONTR	0	0	0	0	76	260	385	511	971	738	778	1075	1310	248.5	1126	1149	
TOTAL EXPENSES	0	22	149	142	169	453	468	594	1058	977.9	867	1203	1399	458.3	1206	1229	
CUM EXPENSES	22	171	313	482	935	1403	1997	3055	4033	4900	6104	7502	7960	9166	#####	#####	
<b>BALANCE</b>		0	424	275	2290	2146	1692	1324	4723	3691	2738	1895	5567	4194	3735	2655	4277
Unobligated Funds					#####	-174	-157	#####	#####	-425	-490	4257	4194	-299	-254	2517	

		1996				1997				1998				1999				2000			
		3	4	1	2	3	4	1	2	3	4	1	2	3	4	1	2	3	4		
1500		1633	2367			4000				4000				3600							
25		75	25		28	82	50	25		32	89			0	96	7	43				
5		9.72	7.9			7.41	3.41			37.5	12.3			0	28.8	15.1					
1530	0	1718	2400	0	28	4089	53.4	25	0	4069	101	0	0	3600	96	35.8	58.1				
#####	#####	#####	#####	#####	#####	#####	#####	#####	#####	#####	#####	#####	#####	#####	#####	#####	#####	#####	32475		
71	57.9	110	39	101	49.8	64.5	75.8	252	67	134	193	140	140	76	328	100	119.44				
32.7	26.6	50.6	17.9	46.6	22.9	30	34.9	116	31	61.8	88.8	64.4	64.4	35	0	46	55				
	7.03				85.1	66.6			138				84.8		-48.2		105.73				
														7.94	7.94	7.94	7.94				
104	91.5	161	56.9	148	158	161	111	367	236	196	282	204	289	119	288	154	288.11				
803	345	202	99.7	172	47.6	0	23.8							-9.49							
552	338	272	290	295	133	75	77.7	42.8	4.35												
405	233	294	238	266	228	126	299	337	133	112	136	51	45.5	31.4	2.5	6.51	0				
0	0	0	0	43.3	143	127	281	340	278	147	500	300	348	235	219	112	7.93				
				29.8	30.2	2.27	8.25	0	1.19	30	0	0	0	0	0	0	0				
						0	73.2	299	479	242	405	549	352	182	352	395	211.63				
										17.3	70.7	107	274	192	170	339	238.02				
														0	0	95.9	67.14				
													6.09		14.2	53.8	57.1	40.06			
														0	0	0	0				
1759	917	768	628	806	581	330	763	1019	895	549	1112	1007	1009	654	798	1006	564.78				
1863	1008	929	685	954	739	491	874	1386	1131	745	1393	1211	1298	773	1086	1159	852.89				
#####	#####	#####	#####	#####	#####	#####	#####	#####	#####	#####	#####	#####	#####	#####	#####	#####	#####	#####	28972		
														*cum ck d							
3944	2936	3725	5440	4486	3775	7373	6553	5191	4061	7385	6093	4882	3584	6411	5422	4298	3503.1				
3944	734	2291	4634	4486	1663	5591	5534	5191	1393	5267	5086	4882	1127	4608	4416	4298	3503.1				

2001				2002				<b>TOTALS</b>	
1	2	3	4	1	2	3	4		
3000								34170.8	
47.5	108							1307	
	24.6							177.18	
3048	108	24.6	0					<b>35655</b>	
#####	#####	#####	35655	35655	35655	35655	35655		
83.6	132	200	200	191	170	100	59.47	4215.96	
38.5	60.5	92	92	87.86	78.2	46	27.36	1767.08	
	69							894.5	
7.94	7.94	7.94	7.94					63.52	
130	269	300	299.94	278.86	248.2	146	86.83	<b>6941.1</b>	
								6649.55	
								4961	
0.49								3722.84	
60								3140.41	
0	0	0						101.78	
236	210	471	0					4455.82	
500	113	311	310.67	310.67				2952.9	
60.2	119	143	143.2	143.2				772.2	
54.1	72.1	122	122.31	0				541.96	
75	127	253	253.33	253.33	253.34	253.34	253.34	1721.58	
985	642	1300	829.51	707.2	253.34	253.34	253.34	<b>29020</b>	
1115	911	1600	1129.5	986.06	501.54	399.34	340.17	<b>35961</b>	
#####	#####	#####	33728	34714	35216	35615	35955		
5435	4632	3057	1927.1	941.01	439.47	40.13	-300		
								<b>35655</b>	
3493	3332	3057	1927.1	941.01	439.47	40.13	-300		

**Table I**

## **2001 AGTSR Industrial Internship Appointments**

<b>APPLICANT</b>	<b>UNIVERSITY</b>	<b>STATUS</b>	<b>COMPANY ASSIGNMENT</b>
Comeaux, Jon Paul	University of New Orleans	SR	Woodward FST
Cao, Thiep X.	Michigan State University	M.S.	Siemens Westinghouse
Durham, Michael G.	University of Central Florida	M.S.	Siemens Westinghouse
Gold, Matthew R.	State University or New York at Stony Brook	M.S.	Solar Turbines
Meyer, Justin D.	Steven Institute of Technology	Ph.D.	GE Aircraft Engines (Evendale Plant)
Hendricks, Adam G.	Virginia Tech	SR	Pratt & Whitney, UTRC
Chukwueloka, Umeh O.	Embry-Riddle University	M.S.	General Electric (Schenectady, NY)
Zygmunt, Steven P.	University of Wyoming	SR	Rolls-Royce
Girard, James W.	Univ. of California, Berkeley	Ph.D.	Solar Turbines
Montgomery, Justin H.	University of Wyoming	SR	Rolls-Royce
Tungseth, Nathan J.	University of Central Florida	SR	Parker Hannifin
Grumstrup, Torben P.	University of Wyoming	SR	Pratt & Whitney

## **Attachment II (a)**

### **COMBUSTOR INSTABILITY SHORT COURSE**

A major reliability issue for low emissions gas turbine combustors has been instabilities. Operation of these lean premixed combustors near their lean blowout limits to limit NOx emissions has resulted in instabilities, excessive combustor noise, structural damage, and removal of commercial turbines from service for repair.

Because lean premixed, low emissions turbine combustors are a relatively recent development, understanding is limited concerning their dynamics and the sources and control of their instabilities.

Under a Faculty Fellowship to Professor F. E. C. Culick of the California Institute of Technology, the Advanced Gas Turbine Systems (AGTSR) program has supported the development of a short course of lectures to equip combustor specialists with a comprehensive understanding of combustion dynamics and control. This course is providing a foundation for engineers at gas turbine companies to design improved stable low emissions combustors. A host gas turbine company (Pratt&Whitney/UTRC) participated in the development of the short course with technical staff providing information on problems encountered in the development of low emissions combustors. Professor Culick presented the short course on periodic visits to UTRC over the six months of the course development. The course is comprehensive (Power Point files with size about 57 MB) in depth and thoroughness with extensive figures and illustrations. It is available to the US gas turbine industry on the Internet.

## **Attachment II (b)**

### **AGTSR INTERNSHIP INITIATES FIVE YEAR UNIVERSITY/INDUSTRY PROJECT**

The Advanced Gas Turbine Systems (AGTSR) program has supported 78 student internships at companies that produce gas turbines engines and components. Twelve interns were placed for periods of 10 to 12 weeks during the summer of this year.

Michael Durham, an M.S. student at the University of Central Florida (UCF), assessed the feasibility of a turbine cooling test rig and designed the test rig during his AGTSR intern assignment this year at the Siemens Westinghouse Power Corporation (SWPC). This work initiated a five-year UCF/SWPC project to evaluate advanced cooling methods for turbine airfoils and endwalls.

---

*AGTSR Success Story*  
September 12, 2001

## **Attachment II (c)**

### **University of Pittsburgh Identifies Turbine Materials for Operation with Steam and Water Injection**

Under the Advanced Gas Turbine Systems (AGTSR), the University of Pittsburgh (Pitt) has conducted experiments to evaluate how water vapor affects oxidation performance of turbine alloys and coatings. Turbine materials are protected from high temperature combustion products by formation of protective oxide scales that are barriers to further penetration of oxygen to the underlying metal. Without protective scales, turbine materials oxidize at excessive rates, resulting in spallation and excessive material loss. Turbine materials can be classified according to whether they tend to form one or the other of the two most protective scales, alumina or chromia oxides.

Commercial experience has shown that use of water or steam injection to control emissions or augment power has produced accelerated oxidation of turbine airfoils. Oxidation experiments at Pitt have shown that turbine materials that form chromia scales are more protective to steam enhanced oxidation than those that form alumina scales in the 700 C temperature range of downstream turbine airfoils. Conversely, turbine materials that form alumina scales were found to be more protective in steam environments than those that form chromia scales in the 900 C temperature range of upstream turbine airfoils. The experiments at Pitt also revealed relative oxidation performance of a number of turbine materials in the 700 C and 900 C temperature ranges.

The experiments at Pitt provide data to turbine designers for the selection of airfoil materials for engines that operate with water or steam injection to reduce emissions or increase power.

## Table II

**AGTSR Subcontract Progress Reports Received  
Third Quarter of CY 2001**

Purdue University <b>Semi-Annual Report</b> <b>8/1/00-1/31/01</b> Subcontract #98-02-SR069 <a href="#">Link to Report</a>	“Turbine Blade Tip, Endwall, and Platform Heat Transfer Including Rotational Effects” PI-Patrick Lawless
Texas Engineering Experiment Station (TEES) Texas A & M <b>Annual Report 4/1/00-4/1/01</b> Subcontract #00-01-SR082cs <a href="#">Link to Report</a>	“Rotating and Stationary Rectangular Cooling Passage Heat Transfer and Friction with Ribs, Pins and Dimples” PI- J.C. Han
Pennsylvania State University <b>Semi-Annual Report</b> <b>1/1/01-7/1/01</b> Subcontract #99-01-SR079 <b>Paper Version Only</b>	“Turbine Tip Clearance Region Desensitization” PI – B. Lakshminarayana
University of North Dakota <b>Annual Report 5/1/00-5/1/01</b> Subcontract #00-01-SR086 <b>Paper Version Only</b>	“Characterization of Catalytic Combustor Turbulence and Its Influence on Vane and Endwall Heat Transfer and Endwall Film Cooling” PI – Forrest Ames
University of California, Santa Barbara <b>Semi-Annual Report</b> <b>2/1/01-8/1/01</b> Subcontract #01-01-SR093 <a href="#">Link to Report</a>	“A Science Based Approach to Enhanced Zirconia-Based Thermal Barrier Coatings for Advanced Gas Turbine Applications” PI – David Clarke
Georgia Institute of Technology <b>Semi-Annual Report</b> <b>1/31/01-7/31/01</b> Subcontract #98-01-SR066 <b>Paper Version Only</b>	“Improvements in Thermal Barrier Coating Durability Via Combustion Chemical Vapor Deposition” PI – Janet Hampikian
University of Minnesota <b>Semi-Annual Report</b> <b>8/1/00-1/31/01</b> Subcontract #98-01-SR071 <a href="#">Link to Report</a>	“Edge Cooling Heat Transfer” PI – Richard Goldstein
University of Pittsburgh <b>Semi-Annual Report</b> <b>2/1/01-7/31/01</b> Subcontract #99-01-SR077 <a href="#">Link to Report</a>	“Interaction of Steam/Air Mixtures With Turbine Airfoil Alloys and Coatings” PI – Fred Pettit
University of California, Berkeley <b>Semi-Annual Report</b> <b>1/1/01-6/1/01</b> Subcontract #99-01-SR074 <b>Paper Version Only</b>	“Fuel-Air Mixing Explored with Optical Probes, Tomography, and Large Eddy Simulations” PI – Robert Dibble
Virginia Commonwealth University <b>Semi-Annual Report</b> <b>2/1/01-8/1/01</b> Subcontract #00-01-SR083	“Improved Performance and Durability in Gas Turbines Through Airfoil Clocking and Hot Stream Management” PI – Eric Sandgren

# **TURBINE BLADE TIP, ENDWALL, AND PLATFORM HEAT TRANSFER INCLUDING ROTATIONAL EFFECTS**

## **Semi-Annual Progress Report**

August 1, 2000 to January 31, 2001

Sanford Fleeter, Principal Investigator

Patrick Lawless, Principle Investigator

Kirk Gallier, Graduate Researcher

Jim Sisco, Undergraduate Intern

School of Mechanical Engineering

Purdue University

West Lafayette, IN 47907-1288

Contract No. 98-02-SR069

Clemson University Research Foundation

South Carolina Energy Research and Development Center

Clemson, South Carolina 29634-5181

# **AGTSR PROGRESS REPORT**

**School of Mechanical Engineering**

**Purdue University**

**West Lafayette, IN 47907-1288**

**Ph. (765) 494-7856 Fax (765) 494-0539**

## **Project Title:**

**TURBINE BLADE TIP, ENDWALL, AND PLATFORM HEAT  
TRANSFER INCLUDING ROTATIONAL EFFECTS**

**AGTSR Subcontract No.** 98-02-SR069

**PI's** Sanford Fleeter  
Patrick B. Lawless

**Period of Performance** January 1, 1998 to July 31, 2000

**Reporting Period** August 1, 2000 to January 31, 2001

## **Program Overview**

Low emission combustors produce turbine gas path radial temperature profiles which are relatively flat. This has resulted in endwall region over-temperature problems, specifically the blade and vane tip and platform regions. The desire to use less film cooling also puts an additional burden on the heat transfer design in these regions. Both data and comparison to CFD solutions are needed to provide a detailed and quantitative definition of both the complex 3-D flow and heat transfer phenomena.

The primary objective of this research is to investigate and quantify airfoil tip, platform and endwall region flow and heat transfer. Specific objectives include the acquisition and analysis of high-quality detailed data quantifying the complex flow in these regions in a research turbine with representative parameters, and comparison of these data to solutions obtained with state-of-the-art CFD tools.

## **Progress in this Reporting Period**

### **Seal Flow Two-Dimensional PIV**

In high temperature turbines, air from disk cavities is forced through the vane-rotor seal to prevent hot gas ingress into these cavities. This purge air plays a role in the effectiveness of platform film cooling as well as interacting with the formation of the horseshoe vortex on the downstream rotor. The objective of this work is to investigate and characterize the aerodynamic signature of this interaction thus comprising a first step towards deeper understanding of the effect on platform heat transfer and the formation of the horseshoe vortex. Toward this end an investigation is performed on the first stage of the Purdue Research Turbine using Particle Image Velocimetry (PIV). The flow field is interrogated in the near hub region of the intra-stage space downstream of the first vane row. In the previous report, data from a measurement spaced between vane wakes were discussed. In this reporting period the measurements describe the influence of the vane wake are presented.

### **Research Turbine**

The Purdue Low-Speed Research Turbine, Figure 1, is a two-stage, axial-flow turbine with constant hub and tip diameters. The blading is of force vortex design, and was designed by the Allison Engine Company (currently Rolls-Royce plc) to recreate the essential features of modern low-solidity turbine airfoils. The significant parameters of the blade rows are presented in Table 1. The facility features a constant tip diameter of 19.18 in. (0.49 m), a hub/tip ratio of 0.739, and a nominal rotational speed of 2500 rpm. Air at ambient pressure and temperature is drawn into the turbine inlet by a centrifugal blower downstream of the test section and powered by a 100-hp (75-kW) electric motor. Air flow rates of 3,000–5,400 cfm (1.4–2.6 m<sup>3</sup>/s) are measured by a 20-in. (0.51-m) diameter venturi flow meter and regulated by a variable inlet vane damper allowing blade row axial velocities ranging 40–110 ft/sec to be achieved. Turbine loading is controlled by a water brake dynamometer that dissipates 40 hp (30 kW) at the highest turbine loading.

The vane-blade gap features a planar seal shown in Figure 2. The purge flow to this seal is supplied by a centrifugal blower and delivered through a tube passing through the turbine inlet forebody, as shown in Figure 3. The flow rate through the seal is metered by a pitot-static velocity measurement made in the delivery tube. The rotor drum face is sealed, and thus the only leakage path for the flow is the planar vane-rotor seal. The nominal seal width is 0.83 mm. The axial gap to disk radius ratio is  $4.5 \times 10^{-3}$ . The seal flow can be controlled to span values for dimensionless seal mass flow rate typical for gas turbine engines.

This investigation employs Particle Image Velocimetry (PIV), a whole field measurement technique that provides quantitative two-dimensional velocity data over a region. The flow is seeded with tracer particles, with the two-dimensional plane of interest illuminated by a laser sheet generated by a timed double pulse of a high-power laser. In the digital PIV technique, a CCD camera synchronized to the laser is used to record the images of the seed particles within the light sheet for both laser pulses. The camera images are then divided into rectangular interrogation regions and correlation algorithms used to determine an average displacement vector for each region. The velocity vectors are then determined by dividing each displacement vector by the specified time between pulses.

## Optical Path

To image the seal flow region, a 1 mm thick laser light sheet introduced through the bellmouth inlet section using a combination of cylindrical lenses. This sheet is brought from the turbine inlet through the first vane to the seal region. Due to the large turning in these blade rows, this necessitates the removal of a single vane and thus a local reduction in solidity. Flow visualization studies were performed to verify that this did not result in any flow separation on the vanes. The measurement planes, shown in Figure 4, spans the distance between vane endwall trailing edge and rotor leading edge, and are located at four positions within the vane spacing. The flow is illuminated in the axial-radial plane, with the measurement thus resolving those components of the flow. The measurement plane dimensions are 21.3 mm in the axial direction by 21.5 mm in the radial direction. To image this region, the digital camera views the flow from an oblique angle through a window located over the first rotor row. Because of the imaging angle, astigmatic corrective optics are employed between the window and the camera lens.

## Data Acquisition and Analysis

The seal flow rates employed in these experiments were selected by dimensionless flow rate (or seal flow Reynolds number) defined as:

$$C_w = \frac{\dot{m}}{\mu r_o}$$

where the actual mass flow rate has been scaled with the fluid viscosity and outer radius of the seal. Typical values for turbine seals range from  $C_w=5\times 10^3$  to  $2 \times 10^4$ . For these experiments, three different seal flow rates of  $C_w=1.2\times 10^4$ ,  $9.2\times 10^3$ , and  $4.6\times 10^3$  were chosen. The turbine operating point during the experiments was near the design point at a flow coefficient of  $\phi=0.515$  and a loading coefficient of  $\psi=1.59$ . The rotational speed was 2500 rpm. This results in a mean inlet velocity to the turbine of 28.7 m/s.

To characterize the unsteady flow field generated by the rotor potential field, the instantaneous flow field is imaged at a fixed time delay from a known position on the rotor drum. This is achieved by triggering the PIV acquisition sequence with a signal generated from a photo-optic sensor on the turbine shaft. The appropriate phase delay calculated from shaft speed readings is introduced by a LaserStrobe 165 Phase Delay Generator. Vernier marks on the rotor drum are also imaged directly with this system to verify the accuracy of the triggering system. The locations where the data are taken are thus indicated by the delay time.

The images corresponding to the first and second laser pulses are divided into rectangular interrogation areas, with cross-correlation software used to determine an average particle displacement for each region. To obtain a high signal-to-noise ratio, the interrogation area must be small enough so that the flow velocity is homogeneous within each region and at the same time large enough to encompass a sufficiently large population of particle pairs. The FFT processing algorithm that computes the cross-correlations generates artificial cyclic background noise at the edges of each interrogation area since this approach assumes that the sampled regions are periodic in space. This can result in the loss of particle pairs due to a low signal-to-noise ratio at the boundaries, with particles near the edges not used in the velocity calculation. However, this information is recovered by over-sampling the images using overlapping interrogation regions. This process does not increase the fundamental spatial resolution, but generates additional vectors as suitable interpolations. For the present investigation 32 x 32 pixel interrogation areas with 50% overlap are used to process the image maps resulting in 3844 raw vectors per image.

To quantify the effects of the rotor motion on the flow field, a phase-locked ensemble average is made of a minimum of one hundred images at each rotor position. This removes the random unsteadiness and preserves that due to blade motion.

## Results: Wake Interaction with Seal Flow

The seal flow was characterized with data taken at three seal mass flow rates, referred to here as high ( $C_w=1.2\times 10^4$ ), midrange ( $C_w=9.2\times 10^3$ ), and low ( $C_w=4.6\times 10^3$ ). In all cases the momentum of the emergent flow, the presence of a vane wake, and the passing rotor potential-field impact the flow development along the hub wall downstream of the seal. To characterize these effects, data in measurement planes A and C are considered, as shown in Figure 4, where Plane A is completely removed from the vane wake convection path and Plane C intersects the vane wake convection path.

A significant alteration of this velocity field occurs when a vane wake crosses the hub seal. For the measurements made in the presence of a vane wake (Plane C) and with high seal flow rate, an area of increased axial velocity over the seal is observed. This high flow condition is likely due to the interaction of the emergent seal flow and the convected wake structures which carry opposite signs of rotation. Higher momentum in the flow near the wall downstream of the seal is observed for both blade positions, as shown by a comparison of the velocity contours of Figures 5 and 6 to those of the corresponding no-wake case, Figures 7 and 8). The wake structure is clearly visible from the negative vorticity observed over the seal in Figures 9 and 10.

The low seal flow case evaluation of velocity magnitude contours shows that in the absence of a vane wake, there is very little boundary layer disruption that can be attributed to the seal flow. Figures 11 and 12 present this no-wake case (Plane A), which shows that in the immediate area of the seal there is a slight reduction in axial velocity. This reduction is more noticeable during the blade pass event. In Plane C, with the vane wake, (Figures 13 and 14) a larger magnitude of axial velocity over the entire measurement field is seen. This is likely due to flow under turning that occurs in the intra-stage space far from the vane exit, as it is an effect that is evident in both the high flow and low flow cases for all rotor positions.

It would be reasonable to expect the same influence of the wake for the low seal flow rate case as that for the high seal flow rate case, but surprisingly Figures 15 and 16 shows otherwise. In this low flow case, the field of high negative normal vorticity associated with the wake appears to be considerably diminished in size. This suggests that the magnitude of the seal flow itself contributes to the size of the wake-generated structure and the resulting degree of influence that the seal – wake interaction has on the downstream flow. In this low flow case, the structure appears to do more than keep the seal flow close to the hub wall, it may act to reinvigorate the platform boundary layer. In fact, referring back to the velocity magnitude plots shown in Figures 13 and 14 for the wake case, an area of increased axial velocity downstream of the seal gap coincides with the region of high negative normal vorticity. Velocity profiles plotted for discrete axial locations around  $x=12\text{mm}$  showed an increasingly smaller boundary layer thickness with increasing axial position.

## Future Work

The above data completes the description of the endwall flow. In the final project period, we hope to conclude measurements in the tip region and prepare a comparison of the seal flow data to results obtained by CFD simulation at Rolls-Royce.

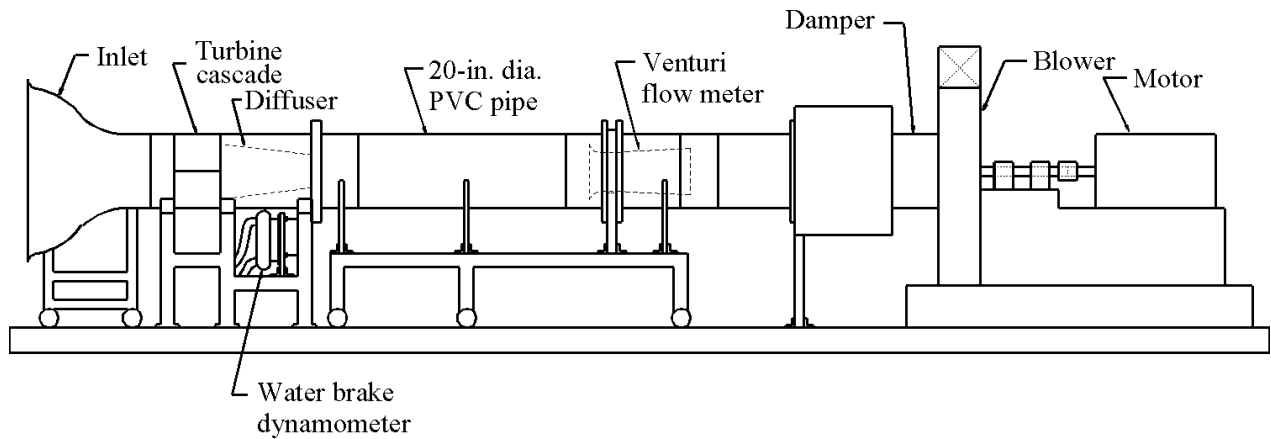


Figure 1. Purdue 2-Stage Research Turbine

Table 1. Turbine Design Geometry

Number of Stages	2
Tip Diameter	19.18 in.
Hub/Tip Diameter Ratio	0.739

### Geometry at 50% span:

	Stator 1	Rotor 1	Stator 2	Rotor 2
Number of Blades	24	32	28	32
Meridional Chord (in.)	2.93	2.23	2.54	2.27
Aspect Ratio	0.85	1.00	1.00	1.00
Solidity	1.288	1.12	0.982	1.100
Camber Angle (deg)	86.0	98.0	98.0	98.0
Thickness/Chord (%)	16	21	21	18

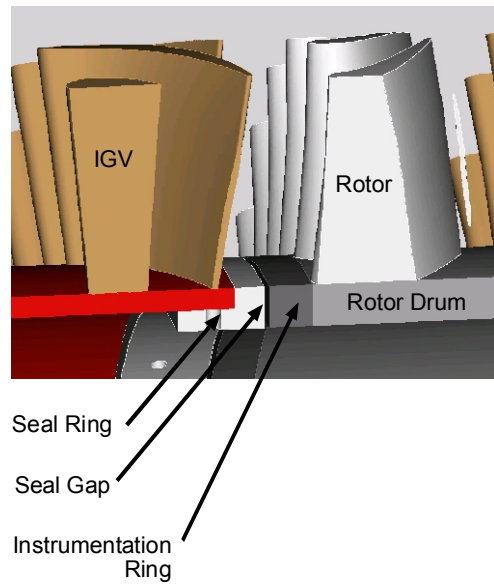


Figure 2. Planar seal between the first vane and the first rotor

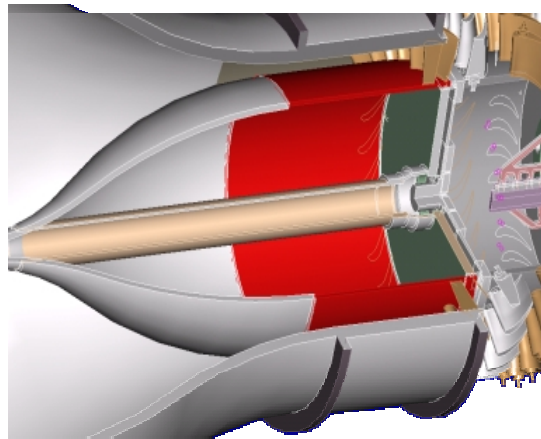


Figure 3. Schematic of delivery path for air supplying the seal flow

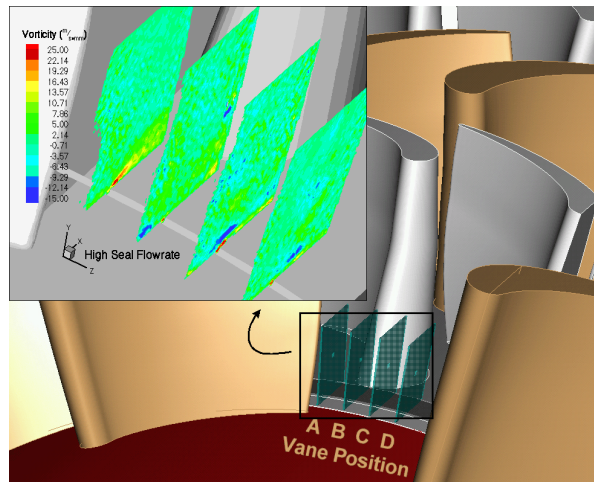


Figure 4. PIV measurement planes.

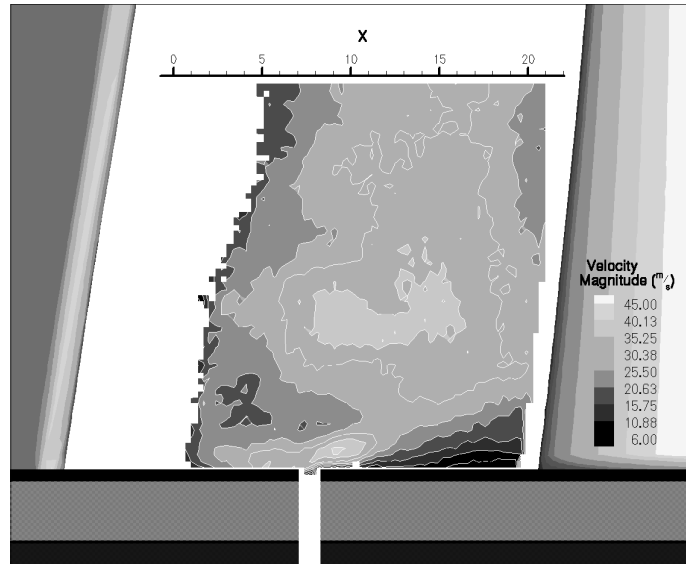


Figure 5. 2-D velocity field, maximum effect of blade potential field ( $t=675\mu s$ ), wake present (Plane C). High seal flow case.

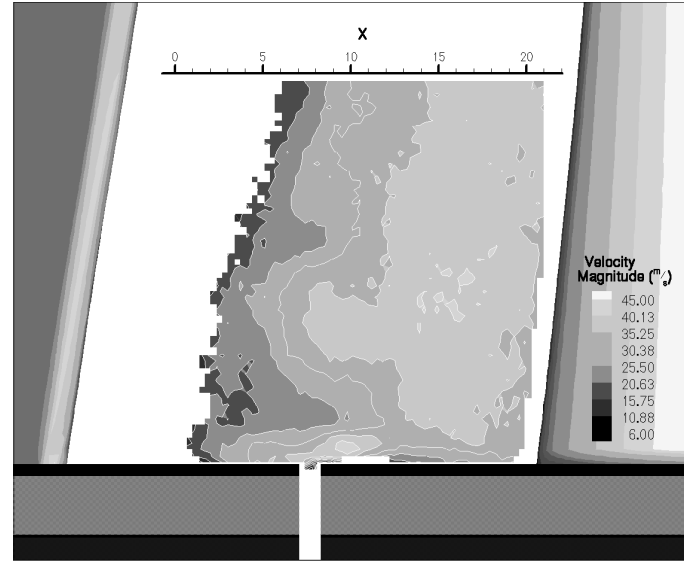


Figure 6. 2-D velocity field, minimum effect of blade potential field ( $t=300\mu s$ ), wake present (Plane C). High seal flow case.

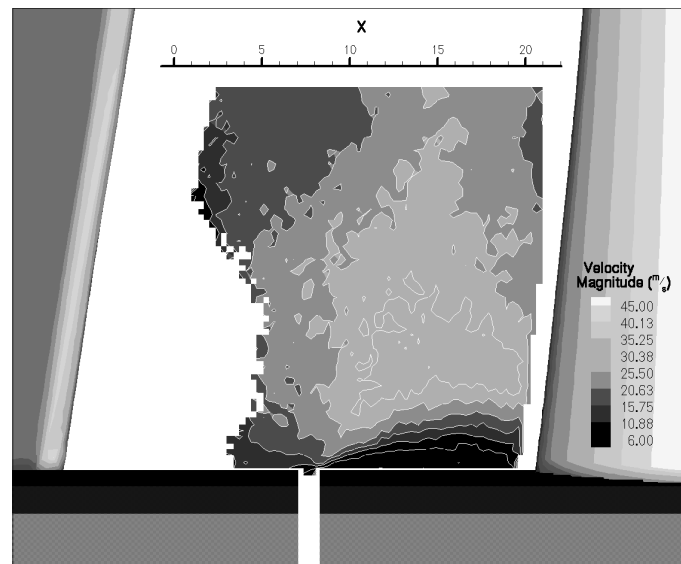


Figure 7: 2-D velocity field, maximum effect of blade potential field ( $t=675\mu s$ ), wake absent (Plane A). High seal flow case.

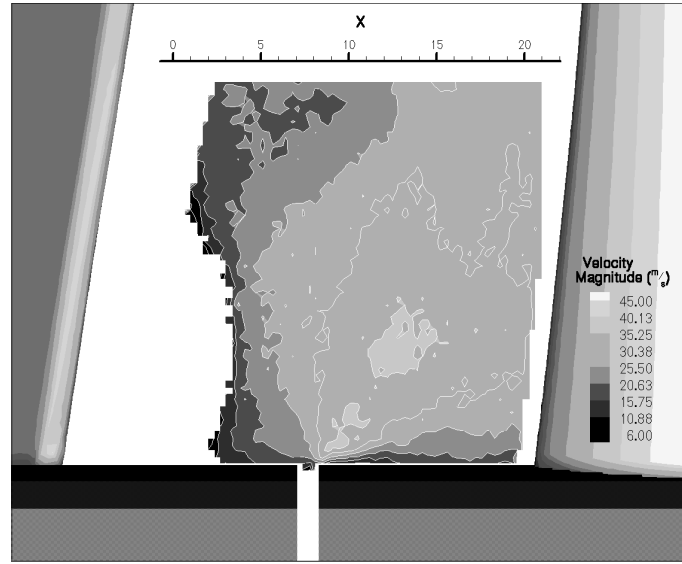


Figure 8. 2-D velocity field, minimum effect of blade potential field ( $t=300\mu s$ ), wake absent (Plane A). High seal flow case.

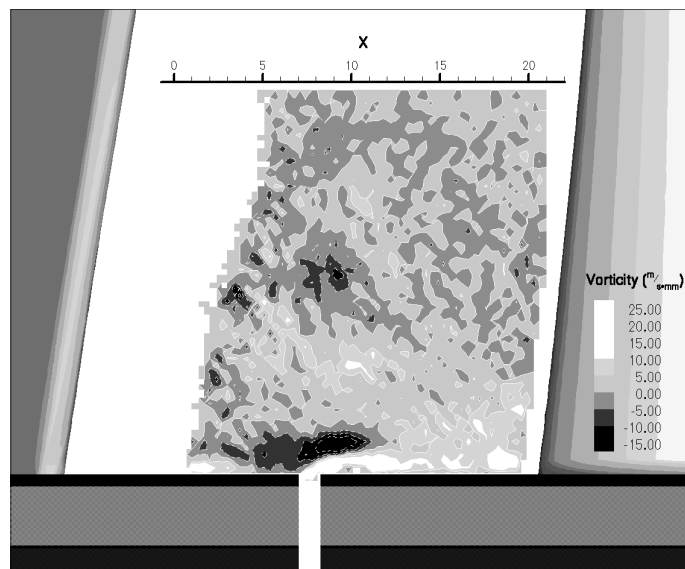


Figure 9. 2-D vorticity field, maximum effect of blade potential field ( $t=675\mu s$ ), wake present (Plane C). High seal flow case.

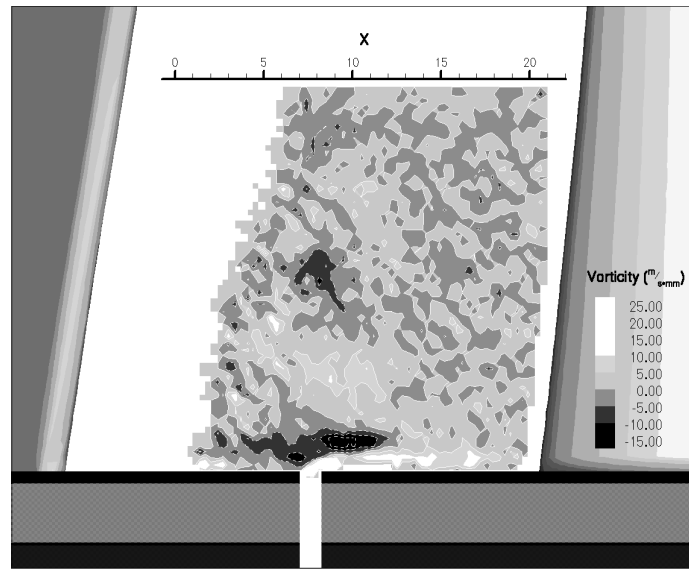


Figure 10. 2-D vorticity field, minimum effect of blade potential field ( $t=300\mu\text{s}$ ), wake present (Plane C). High seal flow case.

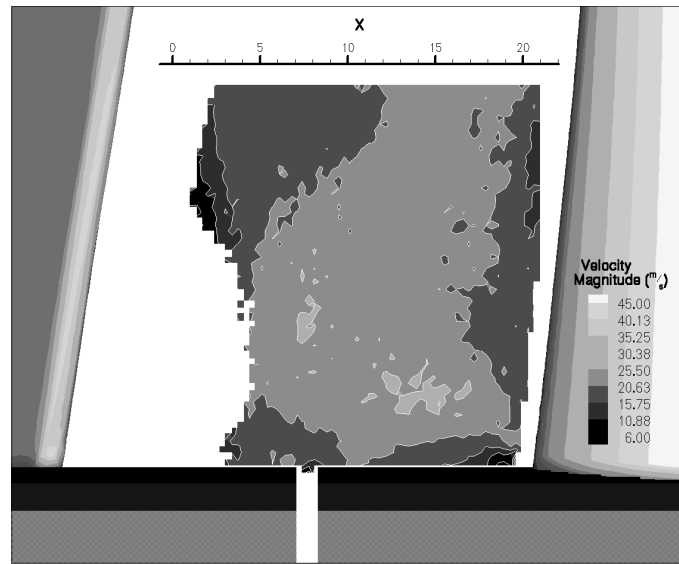


Figure 11. 2-D velocity field, maximum effect of blade potential field ( $t=675\mu\text{s}$ ), wake absent (Plane A). Low seal flow case.

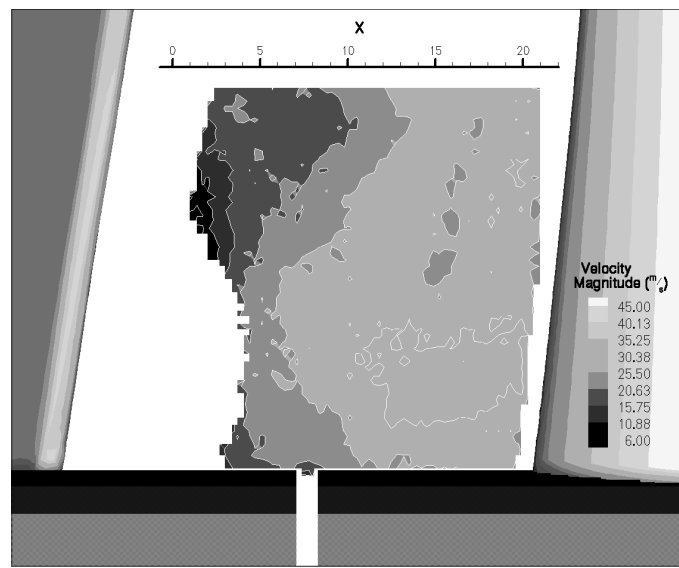


Figure 12. 2-D velocity field, minimum effect of blade potential field ( $t=300\mu s$ ), wake absent (Plane A). Low seal flow case.

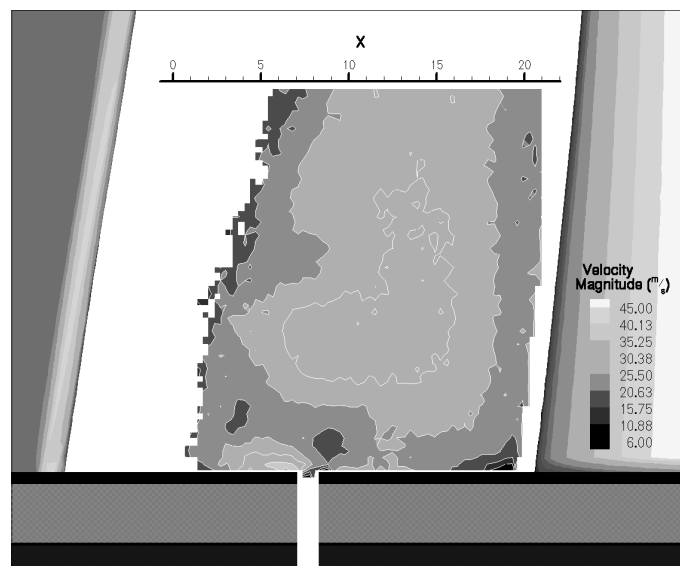


Figure 13. 2-D velocity field, maximum effect of blade potential field ( $t=675\mu s$ ), wake present (Plane C). Low seal flow case.

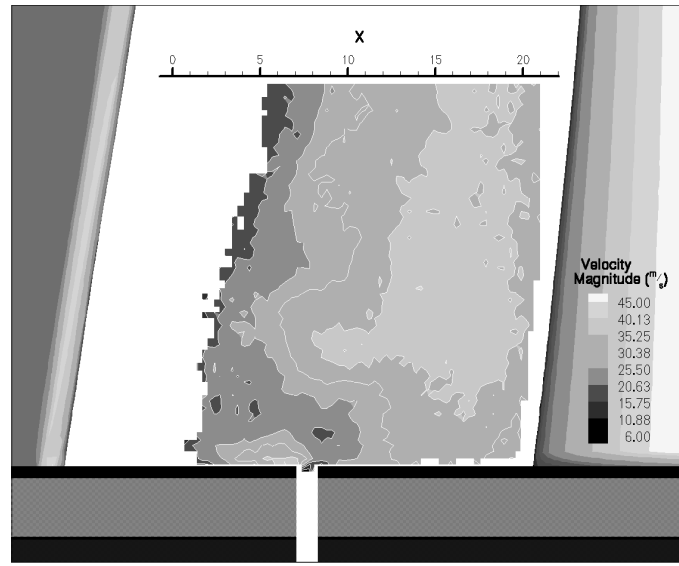


Figure 14. 2-D velocity field, minimum effect of blade potential field ( $t=300\mu s$ ), wake present (Plane C). Low seal flow case.

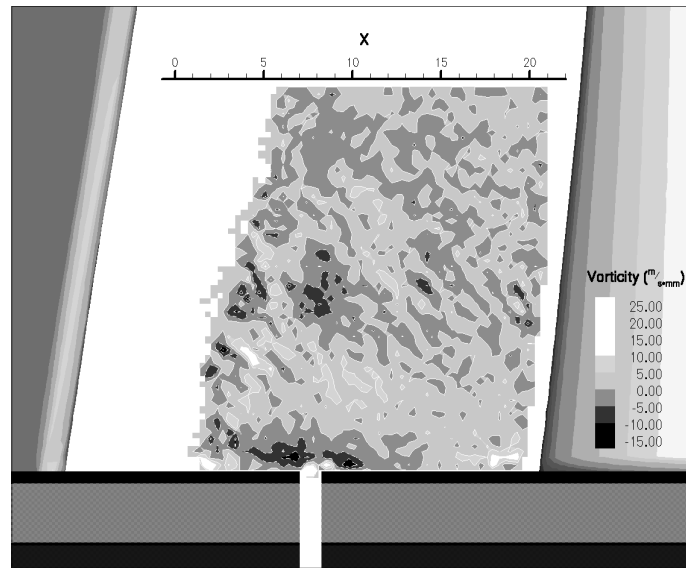


Figure 15. 2-D vorticity field, maximum effect of blade potential field ( $t=675\mu s$ ), wake present (Plane C). Low seal flow case.

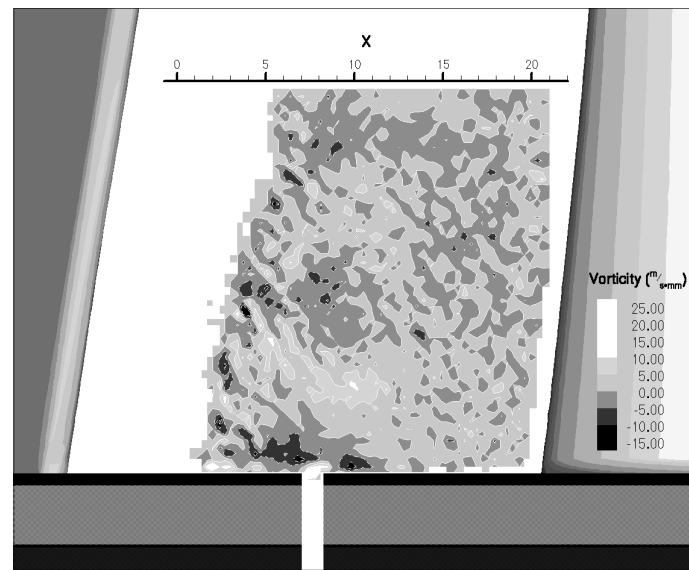


Figure 16. 2-D vorticity field, minimum effect of blade potential field ( $t=300\mu\text{s}$ ), wake present (Plane C). Low seal flow case.

**Annual Progress Report for:  
AGTSR Project No. SR-082**

**Rotating and Stationary Rectangular Cooling Passage Heat  
Transfer and Friction with Ribs, Pins and Dimples:**

**Prepared under the Direction of:**

**J.C. Han**

**(Principal Investigator)**

**Dept. of Mechanical Engineering, Texas A&M University**

Ph: (979) 845-3738 \*\*Fax: (979) 862-2418 \*\*E-mail: JCHan@mengr.tamu.edu

**Phil Ligrani**

**(Principal Investigator)**

**Dept of Mechanical Engineering, University of Utah**

Ph: (801) 581-4240 \*\*Fax: (801) 585-9826 \*\*Email: ligrani@mech.tamu.edu

**and**

**H.C. Chen**

**(Co-Principal Investigator)**

**Dept. of Civil Engineering, Texas A&M University**

**June 30, 2001**

## TABLE OF CONTENTS

PROJECT SUMMARY .....	3
PART I - ROTATING HEAT TRANSFER: .....	3
PART II - STATIONARY HEAT TRANSFER AND FLOW FIELD:.....	4
PART III - COMPUTATIONAL STUDY:.....	5
PART I: ROTATING HEAT TRANSFER .....	6
ABSTRACT .....	7
NOMENCLATURE .....	7
INTRODUCTION .....	8
EXPERIMENTAL FACILITY.....	13
DATA REDUCTION .....	15
RESULTS AND DISCUSSION .....	17
Secondary Flow Behavior:.....	18
Smooth Channel Results:.....	19
Ribbed Channel Results:.....	22
Streamwise Averaged Nusselt Number Ratio:.....	24
CONCLUSIONS .....	26
REFERENCES .....	26
PART II: STATIONARY HEAT TRANSFER AND FLOW FIELD.....	29
SURFACE GEOMETRIES AND OVERALL EFFORTS AT THE U. OF U. ....	30
TEST CONFIGURATIONS .....	31
FLOW PARAMETERS.....	32
EXPERIMENTAL FACILITIES.....	32
TEST SECTIONS-STATUS AND USE .....	32
TEST SECTIONS-DESIGN DETAILS .....	33
EXAMPLES OF FLOW STRUCTURAL RESULTS.....	34
EXAMPLE OF FRICTION FACTOR RESULTS .....	36
EXAMPLES OF HEAT TRANSFER RESULTS .....	36

PART III: NUMERICAL PREDICTION.....	39
ABSTRACT .....	40
NOMENCLATURE .....	40
INTRODUCTION .....	41
Motivation: .....	41
Literature Review: Experimental Studies .....	42
Literature Review: Numerical Studies.....	43
DESCRIPTION OF PROBLEM.....	46
COMPUTATIONAL PROCEDURE .....	47
Overview: .....	47
Chimera RANS Method: .....	48
Boundary conditions:.....	49
Computational grid details:.....	49
RESULTS AND DISCUSSION.....	50
Velocity and Temperature Fields:.....	51
Detailed Local Heat Transfer Coefficient Distribution:.....	55
Spanwise-Averaged Heat Transfer Coefficients and Comparison with Experimental Data.....	58
CONCLUSIONS .....	62
REFERENCES .....	63
 ONGOING WORK.....	69
PART I: ROTATING HEAT TRANSFER .....	69
PART II: STATIONARY HEAT TRANSFER AND FLOW FIELD.....	69
PART III: NUMERICAL PREDICTION .....	70
 APPENDIX I: FIGURES FOR PART 1.....	72
APPENDIX II: FIGURES FOR PART 2 .....	82
APPENDIX III: FIGURES FOR PART 3 .....	100

## **PROJECT SUMMARY**

The objective of this three-part investigation is to provide industry with much needed heat transfer data to assist the designers in improving the cooling performance and thermal efficiency of power generation and industrial turbine engines. More specifically, this investigation ventures into the heat transfer phenomenon of internal cooling channels near the trailing edge of a turbine blade, which has yet to be reported in detail. The research is divided into three parts: Part I - Rotating Heat Transfer; Part II - Stationary Heat Transfer; Part III - Numerical Prediction. This investigation is a collaboration between Dr. J.C. Han and Dr. H.C. Chen of Texas A&M University and Dr. Phil Ligrani of the University of Utah. This report details the first stage of this investigation, namely the channel of aspect ratio AR = 4:1. This investigation also concerns heat transfer investigations into a channel of AR = 8:1 to be completed subsequent to the 4:1 investigation presented in this report. A more detailed breakdown of the investigation of each of the three parts follows.

### ***Part I - Rotating Heat Transfer:***

The objectives of part I are to obtain experimental data from rectangular, internal cooling passages with aspect ratios of 4:1 and 8:1. The following parameters will be varied: (1) Surface geometry (2) Reynolds number, (3) rotation number, (4) rotation angle, and (5) channel aspect ratio. Ribs, pins, and dimples will be installed on the leading and trailing sides of a rectangular internal cooling passage with rotation. The ratio of inlet coolant temperature to surface temperature (TR) will be around 0.8 - 0.9. The experiments is designed so that regionally averaged heat transfer coefficients will be measured at different locations along the cooling

passages under rotating conditions. Both the streamwise and spanwise distribution of the heat transfer enhancement will be obtained. The new heat transfer data will be correlated and compared with numerical predictions in part III. The existing rotating facility and instrumentation available in the Turbine Heat Transfer Laboratory of Texas A&M University is used in this study.

### ***Part II - Stationary Heat Transfer and Flow Field:***

The objectives of Part II are to obtain experimental data from rectangular, internal cooling passages with aspect ratios of 4:1 and 8:1. The following parameters will be varied: (i) surface geometry, (ii) ratio of absolute inlet temperature to wall temperature, (iii) Reynolds number, and (iv) channel aspect ratio. Ribs, pin fins, dimples and smooth surfaces will be installed on the surface of a rectangular internal flow passage (without rotation). The ratio of inlet coolant temperature to surface temperature (TR) will range from 0.6 to 1.0. The experiments will be designed so that: (a) spatially-resolved surface heat transfer coefficients will be measured at different location along the instrumented surface which contains the concavities, and (b) detailed flow structure above the different surface configurations will be measured using existing five-hole pressure probes, flow visualization apparatus, and pressure transducer equipment. Spatially-averaged data will be deduced from the spatially-resolved data. The flow structure data will aid numerical model development in Part III. Two existing test facilities, available in the Convective Heat Transfer Laboratory of the University of Utah, are employed.

### ***Part III - Computational Study:***

The objectives of part III are to predict flow and heat transfer behaviors from rectangular, internal cooling passages with aspect ratios of 4:1 and 8:1. An ongoing Chimera Reynolds-Averaged Navier-Stokes (RANS) code together with an advanced state of the art second-order Reynolds stress (second moment) turbulence model will be used for the prediction of rotating and stationary rectangular cooling channels with ribs, pins or dimples. The present numerical model has been tested to provide much better flow and heat transfer predictions than the standard k- $\epsilon$  turbulence model for rotating multi-pass square channels. The numerical predictions will be calibrated/compared with the part I-rotation at TR = 0.9 and with the part II-stationary at TR = 0.6. The ultimate goal is to predict flow and heat transfer in rotating rectangular channels with ribs (pins or dimples) at very high Reynolds number and buoyancy parameter conditions.

# **PART I: ROTATING HEAT TRANSFER**

Part 1 is conducted at Texas A&M University under the direction of Dr. J.C. Han

## ABSTRACT

An investigation into determining the effect of rotation on heat transfer in a rib-roughened rectangular channel with aspect ratio of 4:1 is detailed in this paper. A broad range of flow parameters have been selected including Reynolds number ( $Re=5000-40000$ ), rotation number ( $Ro=0.04-0.3$ ) and coolant to wall density ratio ( $D_r/r=0.122$ ). The rib turbulators, attached to the leading and trailing surface, are oriented at an angle ( $\alpha=45^\circ$ ) to the direction of flow. The effect of channel orientations of  $\beta = 90^\circ$  and  $135^\circ$  with respect to the plane of rotation is also investigated. Results show that the narrow rectangular passage exhibits a much higher heat transfer enhancement for the ribbed surface than the square and 2:1 duct previously investigated. Also, duct orientation significantly affects the leading and side surfaces, yet does not have much affect on the trailing surfaces for both smooth and ribbed surfaces. Furthermore, spanwise heat transfer distributions exist across the leading and trailing surfaces and are accentuated by the use of angled ribs. The smooth and ribbed case trailing surfaces and smooth case side surfaces exhibited a strong dependence on rotation number.

## NOMENCLATURE

$A_p$  surface area of copper plate ( $m^2$ )

$D$  hydraulic diameter (m)

$e$  rib height (m)

$h$  heat transfer coefficient ( $W/m^2 K$ )

$k$  thermal conductivity of coolant ( $W/mK$ )

$L$  length of duct (m)

$Nu$	regionally averaged Nusselt number, $hD/k$
$Nu_o$	Nusselt number in fully-developed turbulent non-rotating tube flow without ribs
$P$	rib pitch (m)
$Pr$	Prandtl number
$Q$	heat transfer (W)
$q_{net}''$	net heat flux at wall (W/m <sup>2</sup> )
$Re$	Reynolds number, $rVD/m$
$R_o$	rotation number, $WD/V$
$T_{bx}$	local coolant bulk temperature (K)
$T_w$	wall temperature (K)
$V$	bulk velocity in streamwise direction (m/s)
$b$	angle of channel orientation
$W$	rotational speed (rad/s)
$\alpha$	rib angle
$r$	density of coolant (kg/m <sup>3</sup> )
$Dr/r$	coolant-to-wall density ratio, $(T_w - T_b)/T_w$

## INTRODUCTION

As the world becomes increasingly industrialized, there develops an ever-increasing demand for energy. Extensive research efforts have recently focused on methods for reducing the consumption of energy. One area focused on improvements in efficiency is the turbomachinery

industry. There is a constant drive to decrease the cost associated with repairing a gas turbine as well as increasing the fuel efficiency. With the wide spread application of turbines from power generation to aircraft propulsion, the cost saving can be enormous. One method of increasing the efficiency of a turbine as well as the thrust of an aero-turbine is by increasing the combustion temperature. This poses a major problem in the hastened degradation of temperature sensitive components of the turbine, principally the turbine blades. To counter the high turbine inlet temperatures (1600-1800K), the physics of turbulent heat transfer are investigated in a cooling model. Turbine blades incorporate internal cooling passages to extract the thermal energy absorbed from the hot combustion gases. This prolongs the life of the blade as well as allowing for increased combustion temperatures, which ultimately increases performance of the turbine.

A small amount of pressurized air is extracted from the compressor and injected into the turbine blades via the cooling air bypass. This relatively low enthalpy gas is forced through the internal cooling passages of the turbine blades, convectively extracting heat from the internal walls. For further thermal protection of the blade, a portion of the internal cooling air is ejected through tiny holes in the walls and tip of the blade, creating a cool film thermal boundary.

When considering the effects of rotation, certain flow phenomena are exhibited that are not observable in the stationary reference frame. Forces are generated under a rotational reference frame, principally the Coriolis and buoyancy forces. These forces generate secondary flows in the plane orthogonal to the mean flow direction. For radial outward flow, the Coriolis and buoyancy forces combine to shift the velocity profile toward the trailing surface. The coolant flow migrates along with the heat transfer augmentation toward the trailing surface. This rotationally induced migration of the cooler core flow results in the advantageous enhancement of heat transfer at the trailing surface, but it is typically balanced by the disadvantageous

reduction in heat transfer from the leading surface. As with most temperature sensitive components, thermal failure in an isolated region is oftentimes just as problematic as failure of the entire component. This is why it is important to analyze the heat transfer phenomenon segment by segment along the length of the blade.

The aspect ratio of the channel also has a profound impact on the effect of rotation. Moving from the mid-chord to the trailing edge of the blade, the channels must become more rectangular as the blade becomes thinner. The orientation of a 4:1 aspect ratio cooling channel in a gas turbine blade is shown in **Figure 1.1**. This thinning of the channel changes the effective secondary flow pattern from that of a square duct. For this reason, one cannot simply apply the knowledge of the rotationally induced flow patterns in a square channel to that of a rectangular channel. Therefore, an investigation of the rectangular channel is necessary to further understand the heat transfer characteristics of the internal cooling channels in a gas turbine blade.

To promote heat transfer in the internal cooling passage, various types of turbulators are used to trip the boundary layer. The onset of turbulence results in higher heat transfer by promoting mixing of the cooler core jet gases with the hot boundary layer at the walls. The most common and effective type of turbulator is referred to as the "rib" or "trip-strip". These ribs appear as small rectangular surface protrusions, and are typically oriented at  $45^\circ$  to the direction of flow on the internal leading and trailing surfaces of the blade. When combining the effects of tripping the boundary layer (ribbed-turbulator) and rotational forces (Coriolis and buoyancy), entirely different turbulence and flow phenomenon are achieved. Combining into this equation the various shapes and sizes of internal cooling channels, it is clear that there is no one single solution that can be applied universally in the field of turbine heat transfer. For this reason, an experimental investigation into each combination of the previously mentioned parameters is

necessary. Until now, published literature concerning the rotational effect on the regionally averaged heat transfer characteristics has not existed for the 4:1 aspect ratio duct.

There are numerous past studies on turbulent flow and heat transfer in the cooling channels of a gas turbine blade. Han and Park [1] published experimental investigations of the heat transfer phenomenon in a stationary rib roughened rectangular channel. Han et al. [2] performed a study of the effect of the rib angle on heat transfer distributions and pressure drop in a stationary square channel with two opposite in-line ribbed walls. These studies showed that the  $60^\circ$  and  $45^\circ$  V-shaped rib performs better than the  $60^\circ$  and  $45^\circ$  parallel rib. It was also concluded that the V-shaped rib out-performs  $60^\circ$  and  $45^\circ$  crossed ribs as well as the  $90^\circ$  rib. Wagner et al. [3,4] conducted detailed experimental investigation to determine the effects of rotation, or more specifically the effects of Coriolis and buoyancy forces on the regionally averaged heat transfer distribution of a serpentine square channel with smooth walls. This study determined that in the first pass, the effect of rotation created a thinner boundary layer on the trailing surface and a thicker boundary layer on the leading surface.

Parsons et al. [5] and Johnson et al. [6] studied the effects of channel orientation and wall heating condition on the regionally averaged heat transfer coefficients in a rotating two-pass square channel with ribbed walls. Parsons et al. [5] discovered that the heat transfer enhancement for the constant wall heat flux boundary condition was more pronounced when the duct is twisted  $45^\circ$  to the plane of rotation when compared to a channel oriented orthogonal to the plane of rotation. Johnson et al. [6] determined that the model orientation with respect to the rotation plane greatly affected the heat transfer distribution.

Dutta and Han [7] investigated the regionally averaged heat transfer coefficients in a rotating two-pass square channel with three different model orientations. They found that the

orientation of the channel with respect to the plane of rotation affected the heat transfer distribution. More specifically, they determined that orienting the channel at an angle with respect to the plane of rotation reduced the effect of rotation when compared to the orthogonal channel orientation.

Until recently, most of the experimental studies have explored only square ducts. However, it is quite common to find rectangular cooling passages, particularly toward the trailing edge of a gas turbine blade. Since the profile of a turbine blade is curved, the exclusive use of square channels is not practical. Past research focused mainly on the square channel; therefore, published data for a rectangular cooling channel is rare. Al-Qahtani et al. [8] published a numerical prediction of the flow behavoir and heat transfer in a rib-roughened, rotating, two pass rectangular channel of aspect ratio 2:1. An interesting description of the flow physics associated with rib flow is included in their investigation. Taslim et al. [9,10] investigated the heat transfer distribution in square and rectangular rib-roughened channels under rotation. They applied the liquid crystal technique to study the effect of rotation on wall heat transfer. It was discovered that the effects of rotation were more apparent in rib-roughened channels with a larger channel aspect ratio and a lower rib blockage ratio. This investigation studied only the heat transfer distribution in an orthogonal rotating channel.

Willett and Bergles [11] performed a detailed investigation of the heat transfer in a narrow, 10:1 smooth rectangular channel oriented at  $60^\circ$  to the r-z plane. Most of their focus dealt with exploring the contribution of buoyancy forces under rotation. They found that the duct orientation induced a significant variation in the heat transfer coefficient in the spanwise direction. It was also found that the normalized Nusselt number at the far-aft-end of the trailing side (or the trailing-outer equivalent in this paper) is a strong function of rotation number and

buoyancy number. However, they did not perform tests at an angle normal to the plane of rotation in order to determine how changing the duct orientation affects the heat transfer distribution within the rectangular channel, nor did they consider the effect of varying the surface configuration, such as the common ribbed surface. Also, most of their study presented data in streamwise averaged format, even though the data was taken at localized points.

Therefore, it is of interest to experimentally investigate the regionally averaged heat transfer distribution in a rotating, rectangular channel of aspect ratio 4:1. The fact that no such literature exists today on this subject raises the following questions:

1. How does the spanwise heat transfer distribution vary within a smooth and ribbed rectangular channel, and is it significant enough to require consideration when designing the cooling channels of a turbine blade?
2. Does the surface configuration and orientation of the rotating rectangular channel significantly affect the heat transfer distribution?
3. Do the narrow aspect ratio ducts exhibit different heat transfer distributions when compared to the square and rectangular channels of lower aspect ratio?

Answers to these questions are pursued in this paper.

## **EXPERIMENTAL FACILITY**

The experimental test rig previously used by Dutta and Han [7] is utilized in this investigation. A variable frequency motor is connected via a gear-and-belt mesh to a hollow, rotating shaft. This shaft runs from the base of the test rig to the work platform and is attached orthogonal to the hollow, rotating arm. The test section is inserted inside the hollow rotating arm, which rotates in a plane orthogonal to the rotating shaft. A hand held optical tachometer is used to determine the rotational velocity of the arm. Thermocouple and heater wires are connected to a 100-channel slip-ring assembly mounted to the rotating shaft. The output of the thermocouples

is transferred to a data logger. Fuse-protected power input to the heaters from the variac transformers is also transmitted through the slip ring assembly. Cooling air is pumped from a steady flow compressor, through an A.S.M.E. orifice flow meter, then through the hollow rotating shaft, turning 90° and passing into the rotating arm, then through the test section and is finally expelled into the atmosphere.

The test section is a 0.5 inch by 2 inch (1.27x5.08 cm) one-pass rectangular channel of aspect ratio 4:1. The direction of airflow is radially outward from the axis of rotation. Two rows of copper plates are installed on both the leading and trailing surface to provide a grid for analysis of the spanwise variation in the regionally averaged heat transfer coefficient.

**Figure 1.2** shows a detailed top view of the test section. The test section is divided into six cross-sections, each with six copper plates: two for the leading, two for the trailing, one for the outer and one for the inner surface. Moving along the direction of the flow (radially outward), there are six streamwise segments for a total of 36 copper plates in the entire test section. The channel length-to-hydraulic diameter ratio ( $L/D$ ) is 7.5 with a ratio of 1.25 for each of the six cross-section segments. Each plate is separated by a 0.0626 inch (0.159 cm) thin strip of nylon to prevent heat conduction between plates. This is important since the objective is to study the spatial distribution of heat transfer.

The copper plates are mounted in a nylon substrate, which comprises the bulk of the test section. Pre-fabricated flexible heaters are installed beneath the leading and trailing surfaces, two to each surface. The outer and inner walls (or side walls) are each heated by a wire-wound resistance heater, which is also installed beneath the copper plates. Sufficient power is supplied in order to maintain a maximum wall temperature of nearly 340K for the corresponding section. The maximum wall temperature, however, will vary between 338-344K in order to maintain the

coolant to wall density ratio at 0.122. This active control is necessary because of a variation in the inlet temperature, which is a function of the time of day and the seasonal variation in room temperature. Thermal conducting paste is applied between the heater and copper plates to promote heat transfer from the heater to the plate. Each plate has a blind hole drilled on the backside in which the thermocouple is installed with thermal conducting glue.

Two different surface configurations (smooth and 45° ribs) are studied as well as two different channel orientations with respect to the direction of rotation ( $b=90^\circ$  and  $135^\circ$ ). Figure 1.2 shows the ribbed surface configuration. The parallel rib configuration was chosen due to the widespread use of 45° parallel ribs in turbine blade cooling channels. The ribs are glued to the leading and trailing surfaces of the channel, resulting in a rib height-to-hydraulic diameter ratio ( $e/D$ ) of 0.078 and a pitch-to-rib height ( $P/e$ ) ratio of 10. The rib flow-attack angle, defined as the angle between the mean flow direction and the rib angle orientation ( $\alpha$ ), is maintained at 45°. The experiments were conducted for Reynolds numbers of 5000, 10000, 20000 and 40000. The test section rotates at a speed of 550 rpm, resulting in a range of rotation number ( $Ro$ ) from approximately 0.04-0.3.

## DATA REDUCTION

This investigation focuses on detailing the regionally averaged heat transfer coefficient at various locations within the internal cooling channel. This heat transfer coefficient is determined by the net heat flux from the heated plate to the cooling air, the surface area of the plate ( $A_p$ ), the regionally averaged temperature of the plate, and the local bulk mean air temperature by the following:

(1)

The net heat flux is calculated using the measured voltage and current supplied to the heater multiplied by the area fraction exposed to the respective plate minus the previously determined amount of heat losses due to external conduction, convection, and radiation energy escaping from the test section. This heat loss calibration is performed for both stationary and rotation experiments with a piece of insulation inserted inside the test section to inhibit natural convection. For this calibration, by knowing the amount of power supplied to the heater and measuring the temperature of the plate, it is possible to determine how much the heat is being lost into the environment using the conservation of energy principle. Equation 1 is used throughout the experiment, neglecting the change of area effect with the addition of ribs. That is, the heat transfer coefficient is calculated based on the projected area.

The regionally averaged wall temperature ( $T_w$ ) is measured directly by the thermocouple installed in the blind hole on the back of each plate. The local bulk mean air temperature ( $T_{b,x}$ ) is determined by a linear interpolation between the measured bulk air inlet and the average of two outlet temperatures (each installed at the midpoint of the two spanwise sections) due to the applicable constant heat flux assumption. Another method used to check the interpolation values is by performing an energy balance; however, the linear interpolation method is used in the calculation of the results presented in this paper. The energy balance equation is:

(2)

To provide a common reference for each analysis, a correlation is used comparing the Nusselt number for the specific duct case to that of fully developed flow through a smooth stationary

circular pipe at the same mass flow rate. For this investigation, the Dittus-Boelter correlation for heating ( $T_w > T_{bx}$ ) is used:

(3)

All air properties are taken based on the mean bulk air temperature with a Prandtl number ( $Pr$ ) for air as 0.71.

Overall uncertainty for the regionally averaged heat transfer is predominantly dependent upon the difference between the wall temperature and the bulk air temperature, the net heat flux input and the ability to maintain a steady mass flow rate. As with most experiments, the uncertainty for this investigation decreases with the increasing magnitude of input parameters. For higher Reynolds numbers, the uncertainty has been determined to be nearly 7%. However, for lower Reynolds numbers ( $Re=5000$ ), the uncertainty could be as much as 20%. The uncertainty analysis was performed using the Kline and McClintock [12] uncertainty analysis procedure. However, it is reassuring to note that performing an energy balance to calculate the expected outlet temperature resulted in a close match to that of the average measured exit temperature value to within 5% at low Reynolds numbers and nearly 1% for higher Reynolds numbers in the case of the ribbed surface configuration.

## RESULTS AND DISCUSSION

Before any discussion of the physics associated with the thin rectangular duct proceeds, it is important to set up a labeling scheme for the various surfaces in the duct. This labeling scheme, seen in **Figure 1.3**, will be used throughout this paper. The inner and outer surface side walls are

named according to their location in the turbine blade. That is, the inner surface is closer to the mid-chord position of the blade (a relatively internal position), and the outer surface is closer to the trailing edge of the blade, and thus is closer to an external surface of the blade. The leading and trailing surfaces of the blade follow the conventional definitions of these surfaces, however each surface is subdivided into two surfaces in order to investigate the span-wise distribution of heat transfer along the major surfaces (leading and trailing). Therefore we have a total of six surfaces: leading-outer, leading-inner, trailing-outer, trailing-inner, outer, and inner. Because of the many intrinsic differences between square and rectangular ducts, a brief discussion on the secondary flow patterns generated by rotation and the ribs in a thin rectangular duct follows.

### ***Secondary Flow Behavior:***

**Figure 1.4** shows a conceptualization of the secondary flow patterns of a smooth and ribbed rotating duct. The smooth duct seen in Figure 1.4a shows how the rotational forces (dotted line) induce a migration of the cooler core flow toward the trailing surface in radially outward flow with the channel oriented at  $\beta=90^\circ$  to the plane of rotation. This results in an increase of the heat transfer from the trailing surface, although it typically results in a decrease in heat transfer at the leading surface.

Tilting the smooth duct to  $\beta=135^\circ$  causes the Coriolis forces to shift the secondary flow pattern from the case of  $\beta=90^\circ$ . Now the secondary flow due to rotation travels along the line from the leading most corner of the duct to the trailing most corner of the duct. This results in a significant increase in heat transfer at the outer surface as well as a moderate increase for the entire leading and trailing surfaces. When ribs are installed as seen in Figure 1.4b, the combination of secondary flows produces a flow behavior that is entirely different from the

smooth surface. The ribs induce a flow pattern parallel to the ribs at the wall, traveling from the primary rib surface (the outer surface in this case) to the secondary rib surface, (the inner surface in this case). This rib configuration was chosen because when the channel is tilted to  $\beta=135^\circ$ , the rib-induced secondary flow constructively combines with the rotation induced secondary flows. Past literature has paid little attention to the constructive and destructive combinations of rib- and rotation-induced secondary flows. At  $\beta=90^\circ$ , the rib-induced secondary flow constructively combines with the rotation-induced secondary flows at the leading-outer and trailing-inner surfaces, while the two secondary flows destructively combine at the trailing-outer and leading-inner surfaces. It is impossible to achieve completely constructive rib- and rotation-induced secondary flows in a channel of  $\beta=90^\circ$  when using continuous ribs. If the ribs had been oriented with the primary rib attached from the inner surface and the secondary rib following toward the outer surface, then a completely destructive combination of the rib- and rotation-induced secondary flows would have resulted across the entire leading and trailing surfaces at the  $\beta=135^\circ$  orientation. While it would be interesting to investigate such behavior, this analysis was limited to only the smooth and  $45^\circ$  rib orientation that produces constructive combinations of secondary flow.

### ***Smooth Channel Results:***

Figures 1.5-1.7 contain the smooth duct data for three different channel configurations: stationary, rotation with  $\beta=90^\circ$  and rotation with  $\beta=135^\circ$ . Each case is subdivided into four experiments: (a)  $Re=5000$ , (b)  $Re=10000$ , (c)  $Re=20000$ , and (d)  $Re=40000$ . The corresponding rotation numbers for these cases are 0.305, 0.151, 0.075 and 0.038 respectively. Please reference Figure 1.3 for the data legend and surface locations within the channel. **Figure 1.5** contains data

for the stationary cases. The initial decrease in the normalized Nusselt number plots is attributable to the entrance effect in thermally developing flow. The plots all approach a horizontal asymptote as the flow approached the thermally fully developed state.

**Figure 1.6** shows the results for the rotation cases where the duct is oriented at  $\beta=90^\circ$ , that is, orthogonal to the plane of rotation. As was expected, the trailing surfaces exhibit higher heat transfer enhancement than the leading surfaces due to the migration of the colder core fluid toward the trailing surface caused by the Coriolis rotational forces. At a duct angle of  $\beta=90^\circ$ , the channel can be assumed to hold symmetry about the plane of rotation. This means that both of the leading surfaces (leading-outer and leading-inner) should have identical Nu plots, the trailing surfaces should exhibit identical behavior, and the two side surfaces should be equal. This is validated relatively well as seen in the figures, with a slight bias between the two trailing surfaces. An increase in the Reynolds number tends to suppress the effect of rotation. All six surfaces show very little streamwise variation in the Nu number plots. Both of the side surfaces (inner and outer) have a heat transfer enhancement nearly equal to the value of the two trailing surfaces.

**Figure 1.7** presents the results of the smooth rotation case with the channel oriented at  $\beta=135^\circ$  with respect to the plane of rotation. Figure 1.7a shows that at a low Reynolds number (high rotation number), there are distinguishable differences in the heat transfer trends among the various surfaces. It can be seen that the trailing-outer and outer surface exhibit the highest heat transfer enhancement of all of the surfaces in the duct. This is attributed to the fact that these two surfaces are the primary recipients of the shifting of the cooler core flow under rotation. This phenomenon is illustrated in Figure 1.4 of the preceding section. After the flow impinges on the trailing-outer and outer surfaces, it passes along the leading and trailing surfaces to the inner

surface, where the heat transfer coefficient is the lowest, and the secondary flow slows down dramatically. Then the flow cycles again, passing from the leading most corner diagonally across the channel toward the trailing most corner. At a high rotation number, the inner surface heat transfer follows a trend quite similar to the stationary cases. It appears that this inner surface is barely affected by rotation. Both of the trailing surfaces have higher heat transfer coefficients than the leading surfaces. A new and interesting finding is the substantial difference in the heat transfer coefficient between the two trailing surfaces. Furthermore, this span-wise difference does not come into effect until nearly half-way through the channel for high rotation numbers ( $Ro=0.305$ ). It is also shown that the leading surface heat transfer increased when compared to the orthogonal channel. The overall increase in heat transfer from nearly all surfaces can be attributed to the fact that twisting the channel greatly increased the linear distance along which the main Coriolis force is directed (from leading most to trailing most corner) and provides an overall better mixing than the  $\beta=90^\circ$ . In the  $\beta=90^\circ$  case, the principal Coriolis vector in the core region of the flow acts across only a short distance (the short width of the channel) and does not serve to mix the flow as well as the twisted channel.

One evident contrast of the results of the  $\beta=135^\circ$  case (Figure 1.7) compared to the  $\beta=90^\circ$  (Figure 1.6) case is apparent in the side surfaces. For the twisted channel, the trend of the outer surface increases while the inner surface trend decreases with  $X/D$ . Furthermore, the inner surface decreases in a similar way as seen in the stationary case. The outer surface, which trails the inner surface, experiences a heat transfer enhancement of as much as three times that of the inner surface for the  $\beta=135^\circ$  case. This is due to the shift of the primary Coriolis induced flow vector from the center of the trailing surface in the  $\beta=90^\circ$  case to the trailing most corner in the  $\beta=135^\circ$  case. This trailing most corner is adjacent to the outer surface, and therefore the outer

surface benefits greatly in heat transfer enhancement due to the twisting of the duct. This is desirable since the outer surface of the  $\beta=135^\circ$  case is closer to the trailing edge of the turbine blade, and thus is likely to experience a higher external heat flux than the inner surface. The inner surface interfaces with the side surface of the adjacent cooling passage, and therefore is less likely to be considered a critical surface.

### ***Ribbed Channel Results:***

The data plots for the ribbed channel cases are presented in Figures (1.8-1.10). **Figure 1.8** shows the stationary ribbed channel data. It can be seen that the thermal entrance effect (decreasing to horizontal asymptote) that occurred in the smooth duct does not apply to the ribbed duct. This is due to the fact that the flow is no longer hydrodynamically fully developed immediately after the beginning of the test section, as was the case with the smooth duct. The ribs at the test section inlet trip the hydrodynamic boundary layer, and the flow is now considered not only thermally developing at the inlet, but also hydrodynamically developing at the inlet to the test section. In fact, the data curves tend to increase for the ribbed stationary case, whereas the plots decrease for the smooth stationary case.

An extremely important observation of this case is to note that the leading-outer and trailing-outer surfaces experience a significantly higher heat transfer enhancement than the leading-inner and trailing-inner surfaces. This is attributable to the orientation of the ribs. The ribs are attached such that the flow first meets the rib at the leading-outer and trailing-outer surfaces, which are the "primary rib" surfaces (see Figure 1.4). The second half of the rib, or "secondary rib" surface, follows as the rib extends toward the inner surface. Therefore, the ribs can be described as running from the outer to the inner surface at  $45^\circ$  to the main flow. As the

flow first meets the rib at the primary rib surface, the hydrodynamic boundary layer is tripped first at this point. The fluid at the ribbed wall is then channeled between the two ribs, flowing parallel to the ribs. The secondary rib flow is fastest at the primary rib surface, and slowing as it passes along the secondary rib surface toward the inner surface, which acts as a stagnation surface. The primary rib surface is able to convect more heat as the fluid passes quickly across the surface. When the flow slows along the secondary rib surface, less heat is convected away by the secondary rib surface. This explains why the leading-outer and trailing-outer (primary rib) surfaces experience higher heat transfer than the leading-inner and trailing-inner (secondary rib) surfaces. Also, the outer surface has a higher heat transfer enhancement than the inner surface because it is peripherally affected by this faster, cooler, primary rib tripped flow. In contrast, the inner surface experiences the heat transfer diminishing effects of flow stagnation.

The stationary rib cases show dependence on Reynolds number for the leading and trailing surfaces, however, the inner and outer surface exhibit nearly no dependence on Reynolds number. This is because as the Reynolds number increases, the rib is less effective at enhancing the heat transfer of the rectangular duct when compared with the stationary smooth circular duct correlation (i.e. normalized Nu decreases). Since the ribs are attached to the leading and trailing surfaces, they experience much more of the enhancing effects of the ribs, and conversely, are affected more by a reduced enhancement of heat transfer at higher Reynolds numbers.

**Figure 1.9** shows the data plots for the ribbed duct under rotation with an orientation orthogonal to the plane of rotation ( $\beta=90^\circ$ ). Looking to Figure 1.9a, we can see that at higher rotation numbers, there is clearly a higher heat transfer from the trailing-outer surface, and an increasing trend with X/D. Also, the trend is similar to that of the stationary case. For this reason, the rib-induced flow is observed to dominate the rotation induced secondary flow. Another

important observation is that the leading-inner surface exhibits nearly the lowest heat transfer enhancement at the highest rotation number.

**Figure 1.10** presents the plots for the ribbed,  $\beta=135^\circ$  twisted channel rotation experiments. We immediately can see that by twisting the channel, the leading-outer surface curve rises to meet the trailing-outer surface curve, with the trailing-outer surface maintaining nearly the same trend as seen in the  $\beta=90^\circ$  case. Even the trailing-outer surface trend increases slightly over that of the  $\beta=90^\circ$  case. From this behavior, it seems as though the effects of rotation for the twisted channel serve to better mix the flow than the orthogonal channel, and most of the surfaces benefit from the entirely constructive combining of rib- and rotation-induced secondary flows for the  $\beta=135^\circ$  case. That is, all surfaces benefit except the inner surface, which is the only surface in the twisted channel to exhibit a lower heat transfer when compared with the orthogonal channel. This is expected because the heat transfer at the inner surface is now mitigated by not only its position as the leading most surface, but also by being situated at the end of the secondary rib. Since the inner surface is likely to be the surface exposed to the side wall of an adjacent cooling passage, a low heat transfer is not foreseen to be a significant problem. Therefore, we can say that the attachment scheme for continuous ribs chosen in this investigation will likely provide the most effective heat transfer augmentation at the necessary surfaces.

#### ***Streamwise Averaged Nusselt Number Ratio:***

An overall heat transfer coefficient for each surface is determined by averaging the streamwise data and then plotting the data as a function of rotation number. **Figure 1.11** shows the streamwise averaged data for the smooth duct. Figure 1.11a ( $\beta=90^\circ$ ) shows that the heat

transfer at the trailing surfaces, the inner surface and the outer surface, is a strong function of rotation number. All four of these surfaces exhibit an increasing trend with increasing rotation number. The two leading surfaces show very little dependence on rotation number. Figure 1.11b ( $\beta=135^\circ$ ) shows that the trailing surfaces are strongly dependent on rotation number. The inner surface is the only surface that shows virtually no dependence on rotation number for this case. A comparison of Figures 1.11a and 1.11b reveals that the two leading surfaces for the  $\beta=135^\circ$  case are more dependent on rotation number than for the  $\beta=90^\circ$  case. These results are different than the results of the square channel of Dutta and Han [7] and the 2:1 rectangular channel investigated by Azad et al. [13]. A comparison of the 4:1 duct with the square and the 2:1 duct reveals that the aspect ratio significantly affects the rotational dependence on heat transfer, particularly for the leading surface. The square duct shows a decreasing trend, the 2:1 duct approaches a nearly horizontal trend, while the 4:1 duct shows an increasing trend. Therefore, as the channel becomes narrower, the heat transfer enhancement at the leading surfaces becomes more positive. It is now conclusive that the aspect ratio significantly affects the heat transfer distribution in the channel.

**Figure 1.12** shows the streamwise averaged heat transfer enhancement for the ribbed duct. For the orthogonal channel of Figure 1.12a, the trailing surfaces and outer surface show an increasing trend with increasing rotation number. The trailing-outer surface exhibits the greatest dependence on rotation number, which is a result of the combination of rib- and rotation-induced heat transfer enhancement. The leading surfaces exhibit little dependence on rotation number. Figure 1.12b shows that all surfaces are a function of rotation number except the inner surface. Furthermore, the twisted channel produces a nearly identical trend for the two primary rib surfaces (leading-outer and trailing-outer). Also, the secondary rib surfaces (leading-inner and

trailing-inner) show very similar trends. A comparison of Figures 1.12a and 1.12b shows that the leading surfaces and the inner surface are positively affected by the channel orientation. The trailing surfaces and the outer surface appear to be unaffected by the channel orientation.

## CONCLUSIONS

This investigation revealed that spanwise heat transfer differences of up to 25% for the smooth tilted channel and 50-75% for the ribbed channel exist across the leading and trailing surfaces. This observation should be addressed when designing the cooling channels of a gas turbine blade. In addition, the duct orientation significantly affects the leading, the inner, and the outer surfaces, yet does not have much affect on the trailing surfaces for both the smooth and ribbed cases. Furthermore, the smooth and ribbed case trailing surfaces and the smooth case side surfaces show a strong dependence on rotation number. Finally, the aspect ratio was determined to affect the leading surface heat transfer enhancement, where the enhancement increases as the channel becomes narrower. Therefore, this investigation has determined that spanwise variations in the heat transfer distribution of rectangular cooling passages exist and that the enhancement is a function of channel orientation, surface configuration, and aspect ratio.

## REFERENCES

- [1] Han, J.C., and Park, J.S., 1988, "Developing Heat Transfer in Rectangular Channel With Rib Turbulators," International Journal of Heat and Mass Transfer, Vol. 31, No. 1, pp. 183-195.

- [2] Han, J.C., Zhang, Y.M. and Lee, C.P., 1991, "Augmented Heat Transfer in Square Channels With Parallel, Crossed, and V-Shaped Angled Ribs," ASME Journal of Heat Transfer, Vol. 113, pp. 590-596.
- [3] Wagner, J.H., Johnson, B.V., and Hajek, T.J., 1991a, "Heat Transfer in Rotating Passage With Smooth Walls and Radial Outward Flow," Journal of Turbomachinery, Vol. 113, pp. 42-51.
- [4] Wagner, J.H., Johnson, B.V., and Kooper, F.C., 1991b, "Heat Transfer in Rotating Serpentine Passage With Smooth Walls," Journal of Turbomachinery, Vol. 113, No. 3, pp. 321-330.
- [5] Parsons, J.A., Han, J.C., and Zhang, Y.M., 1995, "Effects of Model Orientation and Wall Heating Condition on Local Heat Transfer in a Rotating Two-Pass Square Channel With Rib Turbulators," International Journal of Heat and Mass Transfer, Vol. 38, No. 7, pp. 1151-1159.
- [6] Johnson, B.V., Wagner, J.H., Steuber, G.D., and Yeh, F.C., 1994b, "Heat Transfer in Rotating Serpentine Passage With Selected Model Orientations for Smooth or Skewed Trip Walls," ASME Journal of Turbomachinery, Vol. 116, pp. 738-744.
- [7] Dutta, S., and Han, J.C., 1996, "Local Heat Transfer in Rotating Smooth and Ribbed Two-Pass Square Channels with Three Channel Orientations," ASME Journal of Heat Transfer, Vol. 118, pp. 578-584.
- [8] Al-Qahtani, M., Jang, Y., Chen, H.C., and Han, J.C., 2001, "Prediction of Flow and Heat Transfer in Rotating Two-Pass Rectangular Channels with 45° Rib Turbulators," ASME Paper No. 2001-GT-0187

- [9] Taslim, M.E., Rahman, A., and Spring, S.D., 1991a, "An Experimental Investigation of Heat Transfer Coefficients in a Spanwise Rotating Channel With Two Opposite Rib-Roughened Walls," ASME Journal of Turbomachinery, Vol. 113, pp. 75-82.
- [10] Taslim, M.E., Bondi, L.A., and Kercher, D.M., 1991b, "An Experimental Investigation of Heat Transfer in an Orthogonally Rotating Channel Roughened With 45° Criss-Cross Ribs on Two Opposite Walls," ASME Journal of Turbomachinery, Vol. 113, pp. 346-353.
- [11] Willett, F.T., and Bergles, A.E., 2000, "Heat Transfer in Rotating Narrow Rectangular Ducts with Heated Sides Oriented at 60° to the R-Z Plane," ASME Paper No. 2000-GT-224.
- [12] Kline, S.J., and McClintock, F.A., 1953, "Describing Uncertainties in Single-Sample Experiments," Mechanical Engineering, Vol. 75
- [13] Azad, Gm S., Uddin, J.M., Han, J.C., Moon, H.K., and Glezer, B. 2001, "Heat Transfer in a Two-Pass Rectangular Rotating Channel with 45° Angled Rib Turbulators," ASME Paper No. 2001-GT-0186.

## **PART II: STATIONARY HEAT TRANSFER AND FLOW FIELD**

Part 2 is conducted at the University of Utah under the supervision of Prof. Phil Ligrani.

## **SURFACE GEOMETRIES AND OVERALL EFFORTS AT THE U. OF U.**

A number of different surface geometries are under investigation as part of the effort underway at the University of Utah. These include: (1) rib turbulators (or trip strips), (2) dimples, (3) pin fins, and (4) smooth surfaces. The project involves experimental measurements of flow and heat transfer characteristics in stationary (non-rotating) models, and analyses of these results. Parameters which are being changed in the experimental study are: (i) Reynolds number, and (ii) ratio of inlet temperature to surface temperature.

Test sections for these tests are relatively large with passage hydraulic diameters of 3-8 inches. This allows: (a) installation of these test sections into an existing facility developed for such tests at the U. of U., (b) spatially-resolved surface heat transfer measurements to be conducted using infrared thermography, and (c) detailed measurements of flow features to be conducted, along with visualizations of flow features. The spatially-resolved data will be used to deduce spatially-averaged results. The flow features will aid numerical model development.

The spatially-resolved measurements are being made of surface heat transfer coefficient distributions (and Nusselt number distributions) using infrared thermography used in conjunction with thermocouples, energy balances, and *in situ* calibration procedures. These spatially-resolved data are obtained principally to: (1) allow the determination of accurate spatially-averaged Nusselt numbers and heat transfer coefficients, and (2) provide detailed information on flow physics near each type of turbulator and dimple investigated. Thermal performance characteristics, such as  $(Nu/Nuo)/((f/fo)^{1/3})$ , are also being determined.

Flow visualization, static pressure drop distributions, and distributions of mean velocity and mean vorticity components are being measured at the U. of U. The latter are being measured using an existing miniature five-hole pressure probe, designed exclusively for such

measurements. The tip diameter of this probe is 1.25 mm to minimize flow blockage and spatial-resolution / spatial-averaging effects. These data will be used: (1) to develop and validate prediction models, and (2) to obtain information on flow physics responsible for the measured surface heat transfer coefficient and Nusselt number variations.

## TEST CONFIGURATIONS

Three configurations are being considered in channels with aspect ratios of 8, which model the narrow channels located close to airfoil trailing edges. For all three cases, single pass channels are employed. The surfaces for which measurements are being obtained are: (i) smooth, (ii) pin fins, and (iii) dimples on two opposite walls.

Three configurations are also being considered in channels with aspect ratios of 4, which also model the narrow channels located near to airfoil trailing edges. For all three cases, single pass channels are employed. The surfaces for which measurements are being obtained are: (i) smooth, (ii) rib turbulators (or trip strips), and (iii) dimples on two opposite walls.

These data will also provide information on the influences of surface geometry on portions of the two pass / serpentine channels. As indicated, different aspect ratios will be employed to obtain data applicable to different interior locations of turbine airfoils employed in utility power engines. The same single passage aspect ratios, turbulator surface geometry, and pin fin surface geometry will be investigated both at the U. of U. and at Texas A&M (scaled to different overall sizes). The channels with smooth surfaces will be used to provide baseline data checks, and to provide data to normalize the Nusselt numbers measured with pin fins, dimples, and rib turbulators.

## **FLOW PARAMETERS**

As mentioned, the following flow parameters are being varied: (i) Reynolds number, and (ii) ratio of inlet temperature to surface temperature.

Different ratios of inlet air temperature to average surface temperature (from about 0.6 to 1.0) are being employed to obtain data on the influences of variable properties and buoyancy on heat transfer in internal cooling passages. A temperature ratio near 1.0 is also being employed so that a baseline data set from the U. of U. can be compared to a baseline data set from Texas A&M. A range of Reynolds numbers (based on hydraulic diameter) from 10,000 to 100,000 are being covered in the experimental tests conducted both at the U. of U. and at Texas A&M.

## **EXPERIMENTAL FACILITIES**

The overall facility employed to obtain the heat transfer data is shown in Fig. 2.1. The rib turbulator test section is currently installed in this facility. The overall facility used to obtain flow structure data and flow visualization results is presented in Fig. 2.2. A test section with dimples on the top and bottom surfaces is currently installed in this facility.

## **TEST SECTIONS-STATUS AND USE**

Photographs of the pin fin test section are shown in Figs. 2.3 and 2.4. This test section is fully instrumented for heat transfer measurements. All flow visualization and flow structure measurements, made with this test section, are completed. Heat transfer measurements with this test section will be starting in July of 2001.

Fig. 2.5 shows a photograph of the smooth surface test section with an aspect ratio of 4, which is to be used for baseline heat transfer measurements. This test section will also be employed for these measurements later in July of 2001.

As mentioned, the rib turbulator test section is currently being tested in the heat transfer facility.

The dimpled test section is currently being fitted with etched-foil heaters at Electrofilm Corp. in Valencia, California. Another dimpled test section is currently being used at the U. of U. for flow visualizations and flow structure measurements.

## TEST SECTIONS-DESIGN DETAILS

Schematic drawings of the rib turbulator test surfaces and test section layouts are shown in Figs. 2.6 and 2.7, respectively. Fig. 2.8 then shows the portion of the rib turbulator test section, which is viewed by the infrared camera to obtain measurements of spatially-resolved surface Nusselt numbers.

Schematic drawings of the pin fin test surfaces and test section layouts are shown in Figs. 2.9 and 2.10, respectively. Fig. 2.11 then shows the portion of the pin fin test section, which is viewed by the infrared camera to obtain measurements of spatially-resolved surface Nusselt numbers.

Schematic drawings of the dimpled test surfaces and test section layouts are shown in Figs. 2.12 and 2.13, respectively. Fig. 2.14 then shows the portion of the dimpled test section, which is viewed by the infrared camera to obtain measurements of spatially-resolved surface Nusselt numbers.

## EXAMPLES OF FLOW STRUCTURAL RESULTS

Examples of flow visualization and flow structural results, obtain for the dimpled and pin fin test sections, are described in this section.

Fig. 2.15 presents flow visualization images recorded downstream of the pin fin test section at a Reynolds number based on channel height of 1,200, or a Reynolds number based on hydraulic diameter of 1,900. The smoke patterns are illuminated over a spanwise-normal plane located downstream of the pin fins, which is positioned 15.99 hydraulic diameters downstream from the leading edge of the test section (which is a total of 13.64 hydraulic diameters in length). The smoke wires, used to produce the smoke are located just downstream of the last row of pin fins, at a streamwise location which is 13.92 hydraulic diameters from the leading edge of the test section. The central portion of the illuminated visualized plane, where the data in Fig. 2.15 are obtained, is positioned immediately downstream of a pin fin. The images in Fig. 2.15 are arranged in a time sequence and are spaced apart by  $1/15^{\text{th}}$  of one second. Numerous vortices, vortex pairs, and other convoluted flow patterns, indicating significant secondary flow patterns, are apparent. Note that a vortex pair, with the flow region between the vortices pointed downwards, is located on the right-hand side of each image (as a result of formation on the right-hand side of a pin). A second large vortex pair, with the flow region between the vortices pointed upwards, is then located on the left-hand side of each image (as a result of formation on the left-hand side of a pin).

The flow structural results, given in Fig. 2.16, also provide evidence of important secondary flows which develop downstream of the pin fins in the time-averaged flow field. These data are given for a Reynolds number based on channel height of 10,000, or a Reynolds number based on hydraulic diameter of 16,000. The miniature five-hole probe, used to obtain these data, is

traversed over a spanwise-normal plane, positioned at the exit plane of the test section (13.64 hydraulic diameters downstream from the leading edge of the test section). Presented in Fig. 2.16 are surveys in spanwise-normal planes of: (a) streamwise velocity, (b) total pressure, (c) static pressure, (d) normal velocity, (e) spanwise velocity, and (f) streamwise vorticity. Note that the streamwise vorticity distributions in Fig. 2.16f are consistent with the large vortices described earlier, which are evident in Fig. 2.15.

Fig. 2.17 presents flow visualizations conducted above the thirteenth row of dimples along the dimpled test section at a Reynolds number based on channel height of 2,100, or a Reynolds number based on hydraulic diameter of 3,400. For these data, dimpled surfaces are placed on the top and bottom surfaces of the channel, and smoke wires are arranged above the fifth row of dimples to visualize flow structure only near the bottom wall of the test section. These smoke wires are located from 2.3 to 2.5 hydraulic diameters from the leading edge of the test section, which is a total of 6.39 hydraulic diameters in length. The illuminated spanwise-normal flow visualization plane is then positioned 6.11 hydraulic diameters from the leading edge of the test section. Note that the streamwise extent of this test section is shorter than the one to be employed for heat transfer measurements (which is a total of 13.64 hydraulic diameters in length). The images in Fig. 2.17 are arranged in a time sequence and are spaced apart by 1/15<sup>th</sup> of one second. Three vortex pairs are evident above the dimple, which is located at the bottom of each flow visualization image of the sequence. One of these vortex pairs is fairly large and is located over the central portion of the dimple, whereas the other two vortex pairs are smaller and are located above the spanwise edges of the dimple. When compared to other flow visualizations obtained above dimpled surfaces at the same Reynolds number, it becomes evident that the vortices form more quickly, and become more fully developed at locations farther upstream,

when dimples are placed at the top and bottom surfaces of the channel, compared to a channel with one smooth surface and one dimpled surface.

## EXAMPLE OF FRICTION FACTOR RESULTS

Friction factor ratios for the duct with aspect ratio of 4, and the rib turbulators on two walls, as dependent upon Reynolds number based on hydraulic diameter, are given in Fig. 2.18. Baseline  $f_o$  values are determined using existing correlations for smooth ducts. The figure shows that friction factor ratios are about constant with Reynolds number, with slightly higher values as the Reynolds number decreases.

## EXAMPLES OF HEAT TRANSFER RESULTS

Examples of local and spatially-averaged Nusselt number data, measured along the rib turbulator test surface at different Reynolds numbers, are presented in Figs. 2.19-2.26.

Fig. 2.19 gives local Nusselt number ratios  $Nu/Nu_o$  (measured using thermocouples employed to obtain surface temperatures), at two different Reynolds numbers. Included in this figure are comparisons with data from Han and Park (1988) for a channel with smooth surfaces, and for a channel with turbulated surfaces, with no rotation. The present rib turbulator test section geometry matches the geometry employed by Han and Park (1988). The present thermocouple data are obtained near the spanwise centerline of the rib turbulator test section, and are somewhat spaced out the streamwise direction because thermocouples are not placed continually along the test surface. Instead, most of the thermocouples are located at the upstream and downstream ends of the test surface, where they are used to aid *in situ* calibration of infrared images. Thus,

the present thermocouple data do not show evidence of multiple rib turbulators along the test surface because they are not spaced together closely enough in the streamwise direction. Instead, our infrared data are used to provide detailed Nusselt number variations, as shown by results presented later in this part of the progress report.

Fig. 2.19 shows that the present data are in approximate agreement with the data of Han and Park for  $X/D_h > 6$ , where their Reynolds numbers based on hydraulic diameter is 30,000, compared to 16,000 and 144,300 for the present study. Note that the thermocouple data from the present study, which are given in Fig. 2.19, are not intended to provide a complete distribution of Nusselt number ratios along the surface, as mentioned, rather, they are used to provide *in situ* calibration data to process the infrared images. The present results are significantly higher than the Han and Park (1988) data on tops of the rib turbulators. In addition, the differences near the upstream portion of the test surface are due to the different flow development lengths employed in the two studies.

Figs. 2.20-2.21 give local Nusselt number ratios measured along the rib turbulator test surface using infrared thermography for Reynolds numbers based on channel height of 10,000, and 90,000, or Reynolds numbers based on hydraulic diameter of 16,000, and 144,000, respectively. Note that color and black and white versions of Figs. 2.20 and 2.21 are included. Fig. 2.22 then gives local Nusselt number ratios, as dependent upon normalized streamwise direction (for  $Z/D_h = 0$ ), determined from the data in the previous two figures, for two different Reynolds numbers. Fig. 2.23 then gives local Nusselt number ratios, as dependent upon normalized spanwise direction (for  $X/D_h = 6.90$ ), determined from the data in Figs. 2.20-2.21, for different Reynolds numbers. From these data, it is evident that the highest local Nusselt numbers are present along the tops of the rib turbulators, and that the lowest values are present just

downstream of each rib turbulator. Important changes with Reynolds number are also evident, especially where Nusselt number ratios are lowest, just downstream of the rib turbulators.

Fig. 2.24 shows Nusselt number ratios, for four different Reynolds numbers based on hydraulic diameter, measured using infrared thermography and averaged in a direction *parallel* to a rib turbulator. These data are presented as dependent upon  $(W/D_h)/(W/D_h)_{max}$ , which is a normalized coordinate oriented in a direction *perpendicular* to a rib turbulator. This coordinate is thus rotated 45 degrees from the direction of the nominal streamwise and spanwise coordinates along the test surface, where the streamwise coordinate is in the direction of the bulk flow. As for the local data described earlier, the spatially-averaged data in Fig. 2.24 show important variations on the top of a rib and on the flat region just downstream of the rib (where  $Nu/Nu_o$  values are lowest), as the Reynolds number (based on hydraulic diameter) varies.

Figs. 2.25 and 2.26 give globally-averaged Nusselt number ratios measured using infrared thermography and averaged over an area amounting to one period of surface geometry. The data in these two figures are given as dependent upon Reynolds number based on channel height, and Reynolds number based on hydraulic diameter, respectively. The globally-averaged Nusselt number ratios in these figures range from 2.85 to 3.36, and thus, are in agreement with magnitudes expected for channel test sections with rib turbulators on two opposite walls.

## **PART III: NUMERICAL PREDICTION**

Part 3 is conducted at Texas A&M University under the direction of Dr. H.C. Chen and Dr. J.C.

Han.

## ABSTRACT

Computations were performed to study three-dimensional turbulent flow and heat transfer in a rotating smooth and 45° ribbed rectangular channels for which heat transfer data were available. The channel aspect ratio (AR) is 4:1, the rib height-to-hydraulic diameter ratio ( $e/D_h$ ) is 0.078 and the rib-pitch-to-height ratio ( $P/e$ ) is 10. The rotation number and inlet coolant-to-wall density ratios,  $\Delta\rho/\rho$ , were varied from 0.0 to 0.28 and from 0.122 to 0.40, respectively, while the Reynolds number was fixed at 10,000. Also, two channel orientations ( $\beta = 90^\circ$  and  $135^\circ$  from the rotation direction) were investigated with focus on the high rotation and high density ratios effects on the heat transfer characteristics of the  $135^\circ$  orientation. A multi-block Reynolds-Averaged Navier-Stokes (RANS) method was employed in conjunction with a near-wall second-moment turbulence closure. In the present method, the convective transport equations for momentum, energy, and turbulence quantities are solved in curvilinear, body-fitted coordinates using the finite-analytic method.

## NOMENCLATURE

$AR$  channel aspect ratio

$D_h, D$  hydraulic diameter

$e$  rib height

$h$  heat transfer coefficient

$k$  thermal conductivity of coolant

$Nu$  local Nusselt number,  $hD/k$

$Nu_o$  Nusselt number in fully-developed turbulent non-rotating tube flow,  $hD/k$

$Pr$	Prandtl number
$Re$	Reynolds number, $rW_bD_h/\mathbf{m}$
$Ro$	rotation number, $WD_h/W_b$
$R_r$	radius from axis of rotation
$S$	streamwise distance
$T$	local coolant temperature
$T_o$	coolant temperature at inlet
$T_w$	wall temperature
$W_b$	bulk velocity in streamwise direction
$\alpha$	rib angle
$\beta$	angle of channel orientation measured from direction of rotation
$\rho$	density of coolant
$\Delta\rho/\rho$	inlet coolant-to-wall density ratio, $(T_w - T_o)/T_w$
$\omega$	rotational speed
$q$	dimensionless temperature, $(T - T_o)/(T_w - T_o)$
$\mu$	dynamic viscosity of coolant

## INTRODUCTION

### ***Motivation:***

To improve thermal efficiency, gas-turbine stages are being designed to operate at increasingly higher inlet temperatures. A widely used method for cooling turbine blades is to bleed lower-temperature gas from the compressor and circulate it within and around each blade.

The coolant typically flows through a series of straight ducts connected by 180° bends and roughened with ribs or pin fins to enhance heat transfer. These cooling ducts may not only be square in cross section or normal to the rotational direction of the blade. In fact, the aerodynamic shape of the turbine blade dictates the use of cooling channels that are rectangular in cross section (with different aspect ratios) and are at an angle,  $\theta$ , from the direction of rotation. Rotation of the turbine blade cooling passages adds another complexity to the problem. It gives rise to Coriolis and buoyancy forces that can significantly alter the local heat transfer in the internal coolant passages from the non-rotating channels. The presence of rib turbulators adds a further complexity since these ribs produce complex flow fields such as flow separation, reattachment and secondary flow between the ribs, which produce a high turbulence level that leads to high heat transfer coefficients.

### ***Literature Review: Experimental Studies***

The complex coupling of the Coriolis and buoyancy forces with flow separation/reattachment by ribs has prompted many investigators to study the flow and temperature fields generated in heated, rotating ribbed wall passages. Most experimental studies on internal cooling passages have focused on non-rotating ducts. See, for example, Han and Park [1], Han et al. [2] Ekkard and Han [3] and Liou et al. [4] and the references cited there. Experimental studies on rotating ducts have been less numerous. Wagner et al. [5], Dutta and Han [6], Soong et al. [7] and Azad et al. [8] investigated rotating ducts with smooth walls. Wagner et al. [9], Johnson et al.[10 and 11], Parsons et al.[12] and Zhang et al.[13] reported studies on rotating square channels with normal and angled ribs while Griffith et al. [14] and Azad et al. [8] studied the effect of channel orientation on rotating smooth and ribbed rectangular

channels with different aspect ratios. Griffith et al. [14] investigated a broad range of flow parameters including Reynolds number ( $Re=5000\text{-}40000$ ), rotation number ( $Ro=0.04\text{-}0.3$ ) and coolant to wall density ratio ( $D_r/r = 0.122$ ). Their experimental results provided a data basis for the present work.

### ***Literature Review: Numerical Studies***

***Smooth Surfaces:*** In addition to the experimental studies mentioned above, several studies have been made to predict numerically the flow and heat transfer in radially rotating smooth and ribbed ducts. Iacovides and Launder [15], Prakash and Zerkle [16], Dutta et al. [17] and Bo et al. [18] studied one passage smooth ducts with normal channel orientation from the direction of rotation i.e.,  $\mathbf{b} = 90^\circ$ . Sathyamurthy et al. [19], Stephens et al. [20], Iacovides et al. [21] and Bonhoff et al. [22] reported numerical predictions for rotating smooth two passage ducts and  $\mathbf{b} = 90^\circ$ . The differential Reynolds stress model (RSM) with wall function in FLUENT code was used in the calculation of Bonhoff et al. [22]. Chen et al. [23, 24] predicted the flow and heat transfer in a rotating smooth two-pass square channel which is the first two passages of the four-pass serpentine passage that was experimentally investigated by Wagner et al. [5]. They used two turbulence models: a two-layer  $k\text{-}\epsilon$  isotropic eddy viscosity model and a near-wall second-moment closure model. The near-wall second-moment closure model accurately predicted the complex three-dimensional flow and heat transfer characteristics resulting from the rotation and strong wall curvature. They provided the most reliable predictions in comparison with the data of Wagner et al. [5]. Al-Qahtani et al. [25] predicted the flow and heat transfer in a rotating smooth two-pass rectangular channel with a  $180^\circ$  sharp turn and an aspect ratio of 2:1 which was also experimentally investigated by Azad et al. [8]. Two channel orientations were

studied:  $b = 90^\circ$  and  $135^\circ$ . They also investigated the effect of the rotation number,  $Ro$ , and inlet coolant-to-wall density ratio  $D_r/r$ .

Ribbed Surfaces: Stephens et al. [26, 27] studied inclined ribs in a straight non-rotating square duct. Stephens and Shih [28] investigated the effect of angled ribs on the heat transfer coefficients in a rotating two-passage duct using a low-Re number  $k-w$  turbulence model. They studied the effects of Reynolds numbers, rotation numbers, and buoyancy parameters. Prakash and Zerkle [29], employing a high Reynolds number  $k-e$  turbulence model with wall function, performed a numerical prediction of flow and heat transfer in a ribbed rectangular duct ( $90^\circ$  rib) with and without rotation. However, their calculations used periodicity and neglected buoyancy effects. They suggested that a low Reynolds number model is necessary to simulate real gas turbine engine conditions and a Reynolds stress model is required to capture anisotropic effects. Bonhoff et al. [22] calculated the heat transfer coefficients and flow fields for rotating U-shaped coolant channels with angled ribs ( $45^\circ$ ). They used a Reynolds stress turbulence model with wall functions in the FLUENT CFD code. Using the periodicity of the flow, Iacovides [30] computed flow and temperature fields in a rotating straight duct with normal ribs. Two zonal models of turbulence were tested: a  $k-e$  with a 1-equation model of  $k$  transport across the near-wall region and a low-Re differential stress model. He concluded that the differential stress model thermal computations were clearly superior to those of the  $k-e/1$ -equation.

Using the same model and method of Chen et al. [23, 24], Jang et al. [31, 32] studied flow and heat transfer behavior in a non-rotating two-pass square channels with  $60^\circ$  and  $90^\circ$  ribs, respectively. Their results were in good agreement with Ekkad and Han's [3] detailed heat

transfer data which validated their code and demonstrated the second-moment closure model superiority in predicting flow and heat transfer characteristics in the ribbed duct. In a later study, Jang et al. [33] predicted flow and heat transfer in a rotating square channel with 45° angled ribs by the same second-moment closure model. Heat transfer coefficient prediction was well matched with Johnson et al. [11] data for both stationary and rotating cases. Al-Qahtani et al. [34] predicted flow and heat transfer in a rotating rectangular channel with 45° angled ribs by the same second-moment closure model of Chen et al. [23, 24]. Heat transfer coefficient prediction was compared with the data of Azad et al. [8] for both stationary and rotating cases. It predicted fairly well the complex three-dimensional flow and heat transfer characteristics resulting from the angled ribs, sharp 180° turn, rotation, centrifugal buoyancy forces and channel orientation.

This affirmed the superiority of the second-moment closure model compared to simpler isotropic eddy viscosity turbulence models. This model solves each individual Reynolds stress component directly from their respective transport equation. The primary advantage of this model is that it resolves the near-wall flow all the way to the solid wall rather than using log-law assumption in the viscous sublayer. With this near-wall closure, surface data like heat transfer coefficients and friction coefficients can be evaluated directly from velocity and temperature gradients on the solid wall.

In practice, the aerodynamic shape of the turbine blade dictates the use of cooling channels that are rectangular in cross section and are at an angle  $\mathbf{b}$  from the direction of rotation. The effect of rotation, channel orientation and large aspect ratio on the secondary flow and heat transfer in rectangular channels may vary from the square channels. Non of the previous studies predicted the characteristics of fluid flow and heat transfer in rotating rectangular channels that

have an aspect ratio,  $AR$ , of 4:1 and are either perpendicular or at an angle from the direction of rotation.

The objective of this study is to use the second moment RANS method of Chen et al. [23, 24] to (1) predict the three-dimensional flow and heat transfer for rotating smooth and ribbed one-pass rectangular ducts ( $AR = 4:1$ ) and compare with the experimental data of Griffith et al. [14] and (2) to investigate the effect of high rotation and high density ratios on the secondary flow field and the heat transfer characteristics in a ribbed duct at  $135^\circ$  orientation.

## DESCRIPTION OF PROBLEM

A schematic diagram of the geometry is shown in Figure 3.1. It has a rectangular cross section with channel aspect ratio,  $AR$ , of 4:1. Two geometries are investigated, one with smooth walls (Figure 3.1a) and the other one with ribs (Figure 3.1b). Two of the four side walls, in the rotational direction, are denoted as the leading and trailing surfaces, respectively, while the other two side walls are denoted as the top and bottom surfaces. The channel hydraulic diameter,  $D_h$ , is 0.8 in. The distance from the inlet of the channel to the axis of rotation (Y-axis) is given by  $R_r/D_h = 20.0$  and the length of the channel is given as  $L/D_h = 22.5$ . The channel consists of unheated starting smooth length ( $L_1/D_h = 9.92$ ), heated smooth or ribbed section ( $L_2/D_h = 7.58$ ) and unheated exit smooth section ( $L_3/D_h = 5.00$ ). The arc length  $S$  is measured from the beginning of the heated section to the end of it. In the ribbed section, the leading and trailing surfaces are roughened with nine equally spaced ribs of square cross section. The rib height-to-hydraulic diameter ratio ( $e/D_h$ ) is 0.078 and the rib-pitch-to-height ratio ( $P/e$ ) is 10. All ribs are inclined at an angle  $\alpha = 45^\circ$  with respect to the flow. Two channel orientations are studied:  $\mathbf{b} = 90^\circ$  corresponding to the mid-portion of a turbine blade and  $\mathbf{b} = 135^\circ$  corresponding to the serpentine

passages in the trailing edge region of a blade. A summary of the cases studied is given in Table 1.

Table 1  
Summary of cases studied,  $Re = 10,000$ .

Case #	Surface	Ro	Dr/r	b	Compare with Exp.
1	Smooth	0.00	0.122	-	yes
2	Smooth	0.14	0.122	90°	yes
3	Smooth	0.14	0.122	135°	yes
4	Ribbed	0.00	0.122	-	yes
5	Ribbed	0.14	0.122	90°	yes
6	Ribbed	0.14	0.122	135°	NA
7	Ribbed	0.28	0.122	135°	NA
8	Ribbed	0.28	0.200	135°	NA
9	Ribbed	0.28	0.400	135°	NA

## COMPUTATIONAL PROCEDURE

### *Overview:*

The Reynolds-Averaged Navier-Stokes equations in conjunction with a near wall Reynolds stress turbulence model are solved using the chimera RANS method of Chen et al. [23, 24]. The governing equations with the second-moment closure turbulence model were described in detail by Chen et. al. [23, 24] and will not be repeated here. The flow is considered to be incompressible since the Mach number is quite low. However, the density in the centrifugal force terms is approximated by  $\mathbf{r}=\mathbf{r}_o T_o/T$  to account for the density variations caused by the temperature differences.  $\mathbf{r}_o$  and  $T_o$  are the density and temperature at the inlet of the cooling

channel. For completeness, the numerical method will be briefly summarized in the following subsection.

### ***Chimera RANS Method:***

The present method solves the mean flow and turbulence quantities in arbitrary combinations of embedded, overlapped, or matched grids using a chimera domain decomposition approach. In this approach, the solution domain was first decomposed into a number of smaller blocks to facilitate efficient adaptation of different block geometries, flow solvers, and boundary conditions for calculations involving complex configurations and flow conditions. Within each computational block, the finite-analytic numerical method of Chen et al. [35] was employed to solve the unsteady RANS equations on a general curvilinear, body-fitted coordinate system. The coupling between the pressure and velocity was accomplished using the hybrid PISO/SIMPлер algorithm of Chen and Patel [36]. The method satisfied continuity of mass by requiring the contravariant velocities to have a vanishing divergence at each time step. Pressure was solved by using the concept of pseudo-velocities and, when combined with the finite-analytic discretization gives the Poisson equation for pressure. To ensure the proper conservation of mass and momentum between the linking grid blocks, the grid-interface conservation techniques of Chen and Chen [37] were employed to eliminate the unphysical mass source resulting from the interpolation errors between the chimera grid blocks. In the present study, the numerical grids in the block overlap region are fully matched. Therefore, the grid interface conservation is automatically satisfied.

### ***Boundary conditions:***

A uniform velocity profile was used at the inlet of the duct ( $Z = 0$ ). The unheated length ( $L_I$ ) was long enough for the velocity profile to be fully developed turbulent profile before the heating start-point ( $Z = L_I$ ). The flow was assumed to be parabolic at the exit of the duct (i.e. zero-gradient boundary conditions) for mean velocity and all turbulent quantities, while linear extrapolation was used for the pressure field. The coolant fluid at the inlet of the duct is air at uniform temperature  $T = T_o$  (i.e.,  $\mathbf{q} = (T - T_o) / (T_w - T_o) = 0$ ). The wall temperature of the unheated sections is kept constant at  $T = T_o$  ( $\mathbf{q} = 0$ ) while the wall temperature of the heated section is kept constant at  $T = T_w$  ( $\mathbf{q} = 1$ ).

### ***Computational grid details:***

Figure 3.2a and 3.2b show the computational grid for the smooth duct and around the ribs for the ribbed duct. The grid was elliptically generated using an interactive grid generation code GRIDGEN [38]. It was then divided into five overlapped chimera grid blocks (three for the case of smooth duct) to facilitate the implementation of the near-wall turbulence model and the specification of the boundary conditions. To provide adequate resolutions of the viscous sublayer and buffer layer adjacent to a solid surface, the minimum grid spacing in the near-wall region is maintained at  $10^{-3}$  of the hydraulic diameter which corresponds to a wall coordinate  $y^+$  of the order of 0.5. The number of grid points in the streamwise direction from inlet to outlet is 50 for the smooth case and 394 for the ribbed duct. Whether smooth or ribbed, the number of grid points in the cross-stream plane is  $33 \times 75$ . The number of grid points and their distributions were obtained based on extensive grid-refinement studies that were performed in Chen et al. [23, 24] and Al-Qahtani [25] for similar smooth channels of a square and rectangular cross sections

and Jang et al. [31-33] for similar ribbed channels. The interested reader is referred to references [23-25] for the details of the grid refinement studies performed on the smooth surface channels. For the ribbed ducts, Jang et al. [31 and 32] performed grid refinement studies on 90° and 60° ribbed two-pass square channels with nine ribs and a total grid points of 1,060,000 and 1,020,000 ( $Re = 30,000$ ) respectively. Also, Jang et al. [33] performed a grid independence study on a 45° ribbed one-pass square channel with 13 ribs ( $Re = 25,000$ ). The numerical grids used in these studies were shown to yield nearly grid-independent results. Also, their results were in close agreement with the experimental data. Note that the number of grid points used in the present rectangular configuration is  $33 \times 75 \times 394$  grid points with a total number of approximately 1,000,000 points which is comparable to the above mentioned geometries. In addition, the Reynolds number used in the present study ( $Re = 10,000$ ) is lower than the one used in the previous studies. Therefore, it is believed that the present grid will produce nearly grid-independent results with accurate resolution of the boundary layer profile and Nusselt number distribution. In all calculations, the root-mean-square (rms) and maximum absolute errors for both the mean flow and turbulence quantities were monitored for each computational block to ensure complete convergence of the numerical solutions and a convergence criterion of  $10^{-5}$  was used for the maximum rms error.

## RESULTS AND DISCUSSION

As summarized in Table 1, computations were performed for one Reynolds number (10,000), rotation numbers ranging from 0 to 0.28 and inlet coolant-to-wall density ratios  $Dr/r$  ranging from 0.122 to 0.40 with two channel orientations of  $\beta = 90^\circ$  and  $135^\circ$ . The Nusselt numbers presented here were normalized with a smooth tube correlation by Dittus-

Boelter/McAdams (Rohsenow and Choi [39]) for fully developed turbulent non-rotating tube flow:

$$Nu_o = 0.023 Re^{0.8} Pr^{0.4}$$

### ***Velocity and Temperature Fields:***

Before discussing the detailed computed velocity field, a general conceptual view about the secondary flow patterns induced by angled ribs and rotation is summarized and sketched in Figure 3.3. The parallel angled ribs in the non-rotating duct (Figure 3.3a) produce symmetric counter rotating vortices that impinge on the inner surface. The Coriolis force in the 90° rotating duct (Figure 3.3b) produces two additional counter-rotating vortices that push the cooler fluid from the core to the trailing surface. For the 135° rotating duct (Figure 3.3c), the Coriolis force produces two long vortices parallel to the ribbed surfaces and a third small vortex in the corner of the top-trailing surfaces. The effect of this rotation secondary flow is to combine destructively with the rib induced secondary flow along the whole leading and trailing surfaces. This is an important concept that will help explain some of the coming heat transfer characteristics.

*Smooth Duct:* At two axial stations as defined in Figure 3.1a, Figures 3.4 through 3.5 show the calculated secondary flow vectors and constant temperature contours for the smooth cases as mentioned in Table 1. Note that these axial stations are viewed from upstream of the channel. It can be seen from Figure 3.4a that secondary corner vortices are generated as a result of the Reynolds stress anisotropy. It can be noticed from the corresponding temperature contour plots that the cooler fluid is located in the core region of the channel cross section. Further

downstream (Figure 3.4b), the level of the secondary corner vortices is the same and the fluid in the duct core is heated more.

In Figure 3.5, the Coriolis forces produce a cross-stream two vortex flow structure (Figure 3.5a) that pushes the cold fluid from the core toward the trailing surface and then brings it back along the inner and outer surfaces to the leading surface. This means that the thermal boundary layer starts at the trailing surface, grows along the two side surfaces and ends at the leading surface. This results in small temperature gradient near the leading surface (hence lower heat transfer coefficients) and steeper one near the trailing surface (hence higher heat transfer coefficients) as seen from the corresponding contour plot of Figure 3.5a. Moreover, the cooler heavier fluid near the trailing surface will be accelerated by the centrifugal buoyancy force while the hotter lighter fluid near the leading surface will be decelerated to maintain the continuity in the streamwise direction. The Coriolis forces, in the  $135^\circ$  smooth duct (Figure 3.6a), produce a secondary flow that pushes the cold fluid away from the corner of the leading and top surfaces. This produces two counter rotating vortices with the one near the leading surface larger than the one near the trailing surface. It can also be noticed that a small vortex is generated at the corner of the top and trailing surfaces. As a result of this secondary flow, the fluid is pushed toward the bottom surface at which part of the secondary flow will move back along the trailing-top surfaces while the other part move along the bottom-leading surfaces such that they meet again at the leading corner. This means that the thermal boundary layer starts at the trailing corner, grows along the trailing-top surface and the bottom-leading surface and ends at the leading corner. This can be seen from the corresponding temperature contour plots where high temperature contours are located near the leading corner.

***Ribbed Duct:*** At several axial stations as defined in Figure 3.2a, Figures 3.7 through 3.10 show the calculated secondary flow vectors and constant temperature contours for the ribbed cases as mentioned in Table 1. Figure 3.7 shows the calculated secondary flow vectors and constant temperature contours for the non-rotating case (case 4). Since the ribs are oriented at a negative  $45^\circ$  angle, the fluid adjacent to the top and ribbed surfaces will reach the ribs first and change direction along the ribbed surfaces toward the bottom surface (Figure 3.7a). It then returns back to the top surface along the centerline of the inclined cross-stream plane. In the same figure, one can also notice the early stages of two symmetric counter-rotating vortices, which become two full symmetric counter-rotating vortices in the midsection of any two ribs (Figure 3.7b). Along the streamwise direction, the size of these two vortices oscillate from the largest in the middle of each inter-rib distance to the smallest on the rib tops (Figure 3.7c). This pattern keeps repeating until the last rib (Figure 3.7d and 3.7e). The effect of the secondary flow on the temperature field is convecting the cooler fluid from the top surface and along the ribbed surfaces towards the bottom surface. It then moves back to the top surface which results in steep temperature gradients and high heat transfer coefficients on both the top and ribbed surfaces as seen in the corresponding temperature contours.

Figure 3.8 shows the cross-stream velocity vectors and temperature contours for case 5 ( $Ro = 0.14$  and  $\beta = 90^\circ$ ) at the same planes as in the non-rotating ribbed duct (case 4). As the flow approaches the first rib, this Coriolis force induced secondary flow starts to distort the secondary flow started by the inclined ribs. This effect can be clearly seen by comparing Figures 3.7a through 3.7e with Figures 3.5a through 3.5e. From this comparison, the following conclusions can be drawn. (1) The magnitude of the Coriolis force induced secondary flow is weaker than the rib induced secondary flow. (2) In the midsections of each of two ribs, the rib

induced vortex near the bottom surface is distorted slightly in the midsection of rib 1 and 2 (Figure 3.8b) but this distortion increases as the fluid proceeds downstream the duct (Figure 3.8d). (3) On the ribs (Figure 3.8c), both vortices shrink in size and get distorted only near the bottom. This pattern repeats itself until the last rib (Figure 3.8e). The general effect of the Coriolis force induced secondary is to distort the rib induced vortices. Consequently, the temperature contours are shifted toward the trailing surface, which affects the heat transfer coefficients from both the leading and trailing surfaces as seen from the corresponding temperature contour plot.

Figure 3.9 shows the cross-stream velocity vectors and temperature contours for case 6 ( $\text{Ro} = 0.14$  and  $\beta = 135^\circ$ ) at the same planes as in the rotating case. The discussion of this Figure is based on comparing Figure 3.9 (case 3 :  $\text{Ro} = 0.11$  and  $\beta = 135^\circ$ ) and Figure 3.8 (case 2:  $\text{Ro} = 0.11$  and  $\beta = 90^\circ$ ). Just before the ribbed section, the rotation induced secondary flow is still dominant as can be seen from comparing Figures 3.9a and 3.8a. However, from rib 1 on, this low rotation induced secondary flow is dominated by the rib induced secondary flow. A careful comparison between the secondary flow fields of case 6 and case 5 (e.g. Figure 3.9d with Figure 3.8d) shows that there is only minor change in the net effect of the secondary flow fields. This minor change appears more clearly in the temperature field. By comparing the temperature contours in Figure 3.9 ( $\text{Ro} = 0.14$  and  $\beta = 135^\circ$ ) with Figure 3.8 ( $\text{Ro} = 0.14$  and  $\beta = 90^\circ$ ), we notice that the cooler fluid is pushed back toward the leading surface, reducing the steep temperature gradients on the trailing surface.

As we increase the rotation number and density ratio, the strength of the rotation-induced secondary flow increases and gradually overcomes the rib induced secondary flow (recall Figure 3.3c). By reaching a rotation number of 0.28 and a density ratio of 0.40 (Figure 3.10), we find

that the rotation-induced secondary flow is dominant over the rib induced secondary flow especially downstream of the channel. This is very clear by comparing the different axial stations in Figure 3.10 and Figure 3.9. This important result has its own consequence on the temperature field and thus the Nusselt number ratio distribution. The rib induced secondary flow is not any more able to drive the secondary flow from the ribs leading side (near the top surface) to the ribs trailing side (near the bottom surface). On the contrary, the rotation induced secondary flow moves the cold fluid from the bottom surface along the ribbed surfaces with the secondary flow along the leading surface is much stronger than the one on the trailing surface. The temperature contours in Figure 3.10 indicate that the cold fluid is moved toward the bottom surface compared to Figure 3.9.

#### ***Detailed Local Heat Transfer Coefficient Distribution:***

Smooth Duct: Figure 3.11a shows the  $Nu/Nu_o$  contour plots on the leading and trailing surfaces for the non-rotating smooth case. The unheated sections were cut to focus on the heated section. The Nusselt number ratios near the beginning of the heated section are high due to the thinner boundary layers. Downstream, they decrease and asymptotically approach the fully developed value.

Figure 3.11b and 3.11c show the  $Nu/Nu_o$  ratio contours on the leading side for the  $90^\circ$  and  $135^\circ$  rotating cases ( $Ro = 0.14$  and  $Dr/r = 0.122$ ). Compared to the non-rotating case, the heat transfer in the  $90^\circ$  case is lower because of the Coriolis force induced secondary flow which pushes the fluid away from the leading surface. For the  $135^\circ$  case, we notice that the  $Nu/Nu_o$  ratios are high next to the bottom surface and then decrease toward the top surface. The reason for this is explained in the velocity section where it was mentioned that part of the cold fluid

comes back from the bottom surface along the leading surface. This means that the thermal boundary layer grows on the leading surface as the secondary flow moves toward the top surface and thus heat transfer will be high at the bottom surface and then decreases towards the top surface.

Figure 3.11d shows the  $Nu/Nu_o$  ratio contours on the trailing side for the  $90^\circ$  rotating case ( $Ro = 0.14$  and  $\mathbf{Dr}/\mathbf{r} = 0.122$ ). The heat transfer is higher on this surface compared to the non-rotating case. This is again a result of the rotation induced secondary flow that pushes the cold fluid toward the trailing surface (see the velocity section). Figure 3.11e shows the  $Nu/Nu_o$  ratios contours on the trailing side for the  $135^\circ$  rotating case ( $Ro = 0.14$  and  $\mathbf{Dr}/\mathbf{r} = 0.122$ ). Except for the entry region, the  $Nu/Nu_o$  ratios are almost constant in the middle portion of the duct.

Ribbed Duct: Figure 3.12a is a plot of the local Nusselt number ratio contours on the leading surface of all ribbed cases for various rotation numbers and density ratios. Figures 3.12b through 3.12e are for  $\beta = 135^\circ$  channel orientation while Figure 3.12f is for  $\beta = 90^\circ$  channel orientation. The entrance and exit regions were cut to focus on the ribbed heated section. First, the effect of increasing the rotation number on the Nusselt number ratio is discussed via Figure 3.12a through 3.12c then the effect of increasing the density ratio is discussed via Figures 3.12c through 3.12e.

Figure 3.12a will be used as the baseline for comparison and discussion. In this figure, the highest Nusselt number ratios were obtained on the top of the ribs, and the lower Nusselt number ratios were obtained right before and after the ribs. Between any two ribs, the Nusselt number ratios are highest near the top surface and decrease as we move towards the bottom surface. This is due to the rib induced secondary flow that moves from the top surface (and

parallel to the ribbed walls) to the bottom surface. Moreover, the Nusselt number ratios between the ribs increase gradually along the duct until the flow approaches the last rib. This is attributed to the secondary flow field which becomes stronger as the flow proceeds downstream and hence the heat transfer is augmented downstream. This feature is a unique characteristic of the angled rib arrangement, which was not found in the normal rib case (Jang [32]).

In Figure 3.12b, the rotation number is increased to 0.14 while the density ratio is kept fixed at 0.122. This causes the Nusselt number ratios to decrease by 19% compared to the non-rotating case (Figure 3.12a). But when the rotation number was increased to 0.28 (Figure 3.12c), we notice that the Nusselt number ratios decrease only by 10% compared to the non-rotating case and high Nusselt number ratios are existing in the middle of the ribbed surface. This is because of the rotation induced secondary flow which gets stronger and gradually overcomes the rib induced secondary flow. In Figure 3.12d, the rotation number is fixed at 0.28 while the density ratio is increased to 0.20. It is seen from this figure that the high Nusselt number ratios are moved further toward the bottom surface. Increasing the density ratio further to 0.40 (Figure 3.12e), we notice that the high Nusselt number ratios are existing now next to the bottom surfaces with a total decrease of only 4% compared to the non-rotating case. Finally, Figure 3.12f shows the Nusselt number ratio distribution for the 90° orientation ( $Ro = 0.14$  and  $Dr/r = 0.122$ ) which are lower by 10% compared to the non-rotating case.

Figure 3.13 shows the same information as in Figure 3.12 but for the trailing surface. Figure 3.13a ( $Ro = 0.00$ ) will be used as the baseline for comparison and discussion. Increasing the rotation number to 0.14 (Figure 3.13b) causes the Nusselt number ratios to increase by only 1% compared to the non-rotating case. This is attributed to the destructive combination of the rotation induced secondary flow with the rib induced secondary flow. In Figure 3.12c, the

rotation number is increased further to 0.28 while the density ratio is kept fixed at 0.122. This causes the Nusselt number ratios to increase by 6% compared to the non-rotating case. Also, it is seen from this figure that the high Nusselt number ratios are spreading toward the bottom surface. Now, the effect of increasing the density ratio will be discussed. In Figure 3.12d, the rotation number is kept fixed at 0.28 while the density ratio is increased to 0.20. In this figure, it is seen that the Nusselt number ratios are pushed slightly more toward the bottom. Increasing the density ratio further to 0.40 (Figure 3.12e) increases the Nusselt number ratios by 12% compared to the non-rotating case. It is seen also from this figure that, upstream of the channel, the high Nusselt number ratios are moved toward the bottom surface while dominate most of the inter-rib regions downstream. Finally, the Nusselt number ratios for the 90° orientation ( $\text{Ro} = 0.14$ ,  $\text{Dr}/\text{r} = 0.122$ ) are shown in Figure 3.13f. The Nusselt number ratios increase by 5% compared to the non-rotating case which is a higher increase compared to the 135° orientation (Figure 3.13b).

### ***Spanwise-Averaged Heat Transfer Coefficients and Comparison with Experimental Data***

*Smooth Duct:* Comparisons of the spanwise-averaged Nusselt number ratios ( $Nu/Nu_o$ ) were made with the experimental data of Griffith et al. [14] in Figure 3.14. In order to compare the effects of the channel orientation on the heat transfer, Figure 3.14 shows the Nusselt number ratios for the three smooth cases: 1, 2 and 3. In this Figure, the inlet coolant-to-wall density ratio was held constant at value of 0.122. The effect of the model orientation can be seen by comparing the 135° Nusselt number ratios with the 90° ones. It can be seen that the 135° Nusselt number ratios are: (a) higher on the leading surface and lower on the trailing surface, and (b) lower on the top surface and higher on the bottom surface. The reason behind that could be explained in the light of Figure 3.6 where it can be seen that the cold fluid received by the 135°

leading surface is cooler than that received by the  $90^\circ$  leading surface. This is because, in the  $90^\circ$  case, the cold fluid reaches the leading surface after it passes over the trailing surface and both of the two side surfaces. However, in the  $135^\circ$  case, the cold fluid moves directly to the bottom surface at which it splits and comes back along the leading surface which means higher heat transfer compared to the  $90^\circ$  case. For the trailing surface, all of cold fluid (in the  $90^\circ$  case) moves directly to the trailing surface after which it splits at its middle. On the other hand, the cold fluid in the  $135^\circ$  case moves first to the bottom surface at which only part of it will come back to the trailing surface which means less heat transfer compared to the  $90^\circ$  case. It can be noticed that the Nusselt number ratios of the top surface of the  $135^\circ$  rotating case are lower than those corresponding to the  $90^\circ$  rotating case. This is attributed to the fact that in the  $135^\circ$  case, most of the top surface behaves as a leading surface in the sense that the fluid is moving away from this surface. Similarly, it can be noticed that the Nusselt number ratios of the bottom surface of the  $135^\circ$  case are higher than those corresponding to the  $90^\circ$  case. This is because the bottom surface in this case behaves as a trailing surface in the sense that it receives the cold fluid directly from the duct core. Comparisons with the experimental values reveals the following. (1) For the non-rotating case, the matching between the experimental and prediction is good on all surfaces. (2) fair agreement on the leading, top and bottom sides is achieved for the rotating cases of  $\beta = 90^\circ$  and  $135^\circ$  but with under-prediction on the trailing surface for both cases.

*Ribbed Duct:* Figures 3.15 shows the spanwise-averaged and regional-averaged Nusselt number ratios ( $Nu/Nu_o$ ) for the ribbed cases 4, 5 and 6. The Reynolds number and the inlet coolant-to-wall density ratio were held constant at values of 10,000, and 0.122, respectively.

Note that the experimental regional-averaged Nusselt number in Griffith et al. [14] is based on the projected area of each copper plate rather than the true heat transfer surface area which includes the 45° rib-increased area. However, the predicted regional-averaged Nusselt Number is based on the true heat transfer area for the test surfaces with 45° ribs which is 1.25 times the projected area. Therefore, the experimental data were divided by 1.25 to reasonably compare with our regional-averaged Nusselt number, except for the inner and outer surfaces where there were no ribs. The overall predicted Nusselt number behavior is in good agreement with Griffith et al. [14] data for the non-rotating case while relatively close in the rotating case. However, the predicted Nusselt numbers on the outer surface are over-predicted. This may be partly attributed to the fact that the predicted Nusselt number ratios are based on a uniform wall temperature boundary condition while the experimental ones are based on a uniform wall heat flux boundary condition

In Figure 3.15 (case 4), the spanwise-averaged Nusselt number distributions on the leading and trailing surfaces show periodic spikes. The higher spikes which occur on the ribs tops are caused by the flow impingement on the ribs, and the lower spikes (which occur right before and after the ribs) are caused by the flow reattachment between the ribs. The Nusselt number ratios are lower just upstream and downstream of the ribs and higher in the regions between the ribs. The Nusselt number ratios increase until the last rib, which is similar to the results obtained in Jang's et al. [33] 45°-ribbed square channel and Al-Qahtani's et al. [34] 45°-ribbed rectangular channel. This phenomenon is caused by the rib-induced secondary flow becoming stronger along the duct as discussed in Figure 3.6. The Nusselt number distribution on the top surface shows that it increases all the way to rib 9 as a result of the secondary flow that pushes the cold fluid towards the top surface. For the same reason, the Nusselt number

distribution on the bottom surface is decreasing since it receives the heated fluid from the ribbed surfaces. Also, it can be noticed that the Nusselt number ratios of the top and bottom surfaces of the  $135^\circ$  case are lower and higher, respectively, compared to the  $90^\circ$  rotating case. This is because the top and bottom surfaces behave as a leading and trailing surfaces in the  $135^\circ$  case as was explained in the smooth case.

Figure 3.16 (case 5) shows that the heat transfer coefficients on the leading surface decreased approximately 10% when compared to the stationary case due to the Coriolis force effect. On the trailing surface, the heat transfer increased approximately 5% as compared to the stationary case

Figure 3.17 (case 6) shows that the heat transfer coefficients on the leading surface decreased approximately 19% when compared to the stationary case, while increased approximately 1% on the trailing surface. The reason why the Nusselt number ratios in case 6 ( $b = 135^\circ$ ) decreased more on the leading and trailing sides and increased more on the leading side and increases less on trailing side compared to case 5 ( $b = 90^\circ$ ) can be understood in light of the conceptual secondary flow diagram in Figure 3.3. The rotation induced vortices in the  $135^\circ$  configuration move along the full face of the leading or trailing surfaces. However, the rotation induced vortices in the  $90^\circ$  configuration move along only one half the face of the leading or trailing surfaces. With this in mind, we notice in Figure 3.3 that the two secondary flows produced by rotation and angled ribs for the rotating  $135^\circ$  duct combine destructively (opposite direction) and thus reduce heat transfer on both the leading surface (a 19% decrease compared to an 10% decrease in  $b = 90^\circ$ ) and the trailing surface (a 1% increase compared to a 5% increase in  $b = 90^\circ$ ). On the other hand, the two secondary flows produced by rotation and angled ribs for the rotating  $90^\circ$  duct combine to (i) constructively (same direction) enhance heat transfer for only

one half of each of the leading and trailing surfaces and (*ii*) destructively (opposite direction) reduce heat transfer for the other half of each of the leading and trailing surfaces.

## CONCLUSIONS

A multi-block RANS method was employed to predict three-dimensional flow and heat transfer in a rotating smooth and ribbed rectangular channel with aspect ratio of 4:1. Two channel orientations are studied:  $b = 90^\circ$  and  $135^\circ$ . The present near-wall second-moment closure model results were compared with the experimental data of Griffith et al. [14]. It predicted fairly well the complex three-dimensional flow and heat transfer characteristics resulting from the large aspect ratio, rotation, centrifugal buoyancy forces and channel orientation. The main findings of the study may be summarized as follows.

*a) Smooth duct:*

- (1) The Coriolis force induces secondary flow, in the  $90^\circ$  rotating case, which pushes the cold fluid from the leading to the trailing surface.
- (2) The Coriolis force induces secondary flow, in the  $135^\circ$  rotating case, which pushes the cold fluid from the leading corner to the bottom surface.
- (3) In the  $135^\circ$  rotating case, most of the top surface behaves as a leading side and thus the Nusselt number ratios on this surface are lower than the corresponding ones on the  $90^\circ$  rotating case. Similarly, most of the bottom surface behaves as a trailing side. Thus, the increase in the Nusselt number ratios is higher on the bottom surface when compared with their counterparts in the  $90^\circ$  rotating case.

*b) Ribbed duct:*

- (1) The inclined ribs start two counter-rotating vortices that oscillate in size along the streamwise direction. For case 4, the secondary flow results in steep temperature gradients and high heat transfer coefficients on both the top and ribbed surfaces
- (2) For case 5 ( $b = 90^\circ$ ), the rotation-induced cross-stream secondary flow distorts the rib induced vortices and consequently, rotation shifts the temperature contours and affects the heat transfer coefficients from both the leading and trailing surfaces.
- (3) For case 4 ( $b = 135^\circ$ ), The rib induced vortices are slightly distorted by rotation-induced secondary flow. The rotation induced vortices have more space along the ribbed surfaces (compared to the  $135^\circ$  case 4) to combine destructively (opposite direction) with the rib induced vortices and thus produce greater Nusselt number ratios decrease (in the case of the trailing surface) and lesser Nusselt number ratios increase (in the case of the leading surface) compared to the  $135^\circ$  rotating case.

## REFERENCES

1. Han, J. C. and Park, J. S., 1988, "Developing Heat Transfer in Rectangular Channel with Rib Turbulators," *Int. J. Heat and Mass Transfer.*, **31**, No. 1, pp. 183-195.
2. Han, J. C., Zhang, Y. M. and Lee, C. P., 1991, "Augmented Heat Transfer in Square Channels with Parallel, Crossed, and V-Shaped Angled Ribs," *ASME Journal of Heat Transfer*, **113**, pp. 590-596.
3. Ekkad S.V. and Han, J. C., 1997, "Detailed Heat Transfer Distributions in Two-pass square Channels with Rib Turbulators," *Int. J. Heat and Mass Transfer.*, **40**, No.11, pp. 2525-2537.

4. Liou T.-M. Tzeng, Y.-Y., and Chen, C.-C., 1998, "Fluid Flow in a 180 Deg Sharp Turning Duct with Different Divider Thicknesses," ASME Paper 98-GT-189.
5. Wagner, J. H., Johnson, B. V. and Kopper, F. C., 1991, "Heat transfer in Rotating Serpentine Passage with Smooth Walls", ASME J. of Turbomachinery, **113**, No. 3, pp.321-330
6. Dutta, S. and Han, J. C., 1996, "Local Heat Transfer in Rotating Smooth and Ribbed Two-Pass Square Channels with Three Channel Orientations", ASME J. of Heat Transfer, **118**, No.3, pp. 578-584.
7. Soong, C. Y., Lin, S. T., and Hwang, G. J., 1991, "An Experimental Study of Convective Heat Transfer in Radially Rotating Rectangular Ducts," ASME J. of Heat Transfer, **113**, pp. 604-611.
8. Azad, GM S., Uddin, M. J., Han, J. C., Moon, H. K., and Glezer, B., 2001, "Heat Transfer in Two-Pass Rectangular Rotating Channels with 45° Parallel and Crossed Rib Turbulators" ASME Paper 2001-GT-0186.
9. Wagner, J. H., Johnson, B. V., Graziani, R. A., and Yeh, F. C., 1992, "Heat Transfer in Rotating Serpentine Passages with Trips Normal to the Flow," ASME J. of Turbomachinery, **114**, No. 4, pp. 847-857.
10. Johnson, B. V., Wagner, J. H., Steuber, G. D., and Yeh, F. C., 1994a, "Heat Transfer in Rotating serpentine Passage with Trips Skewed to the Flow," ASME J. of Turbomachinery, **116**, pp. 113-123.

11. Johnson, B. V., Wagner, J. H., Steuber, G. D., and Yeh, F. C., 1994b, "Heat Transfer in Rotating serpentine Passage with selected Model Orientations for Smooth or Skewed Trip Walls," ASME J. of Turbomachinery, **116**, pp. 738-744.
12. Parsons, J. A., Han, J. C., and Zhang, Y. M., 1995, "Effects of Model Orientation and Wall Heating Condition on Local Heat Transfer in a Rotating Two-Pass Square Channel with Rib Turbulators," Int. J. Heat Mass Transfer, **38**, No.7, pp. 1151-1159.
13. Zhang, Y. M., Han, J. C., Parsons, J. A., and Lee, C. P., 1995, "Surface Heating Effect on Local Heat Transfer in a Rotating Two-pass Square Channel with 60 deg Angled Rib Turbulators," ASME J. of Turbomachinery, **117**, pp. 272-280.
14. Griffith, T. S., Al-Hadhrami, L. and Han, J. C., 2001, "Heat Transfer in Rotating Rectangular Cooling Channels with Angled Ribs," AIAA Paper 2001-2820.
15. Iacovides, H. and Launder, B.E., 1991, "Parametric and Numerical Study of Fully Developed Flow and Heat Transfer in Rotating Rectangular ducts," ASME J. of Turbomachinery, **113**, pp. 331-338.
16. Prakash, C. and Zerkle, R., 1992, "Prediction of Turbulent Flow and Heat Transfer in a Radially Rotating square Duct," ASME J. of Turbomachinery, **114**, No. 4, pp. 835-846.
17. Dutta, S., Andrews. M. J. and Han, J. C., 1996, "Prediction of turbulent heat transfer in rotating smooth square ducts," Int. J. Heat Mass Transfer, **39**, No. 12, pp. 2505-2514.
18. Bo, T., Iacovides, H. and Launder, B. E., 1995, "Developing Buoyancy-Modified Turbulent Flow in Ducts Rotating in Orthogonal Mode," ASME J. of Turbomachinery, **117**, No. 3, pp. 474-484.

19. Sathyamurthy, P. S., Karki, K. C. and Patankar, S. V., 1994, "Prediction of Turbulent Flow and Heat Transfer in a Rotating Square Duct with a 180 Deg. Bend," ASME Paper 94-GT-197.
20. Stephens, M. A., Shih, T. I.-P. and Civinskas, K. C., 1996, "Computations of Flow and Heat Transfer in a Rotating U-Shaped Square Duct with Smooth Walls," AIAA-96-316.
21. Iacovides, H., Launder, B. E. and Li, H-Y., 1996, "The computation of flow development through stationary and rotating U-ducts of strong curvature," Int. J. Heat and Fluid Flow, **17**, No. 1, pp.22-33.
22. Bonhoff, B., Tomm, U., Johnson, B. V. and Jennions, I., 1997, "Heat Transfer Predictions For Rotating U-Shaped Coolant Channels with Skewed Ribs and with Smooth Walls," ASME Paper 97-GT-162.
23. Chen, H. C., Jang, Y. J., and Han, J. C., 2000, "Computation of heat transfer in rotating two-pass square channels by a second-moment closure model," Int. J. Heat and Mass Transfer, **43**, No. 9, May, pp.1603-1616
24. Chen, H. C., Jang, Y. J., and Han, J. C., 2000, "Near-Wall Second-Moment Closure for Rotating Multi-pass Cooling Channels," Journal of Thermophysics and Heat Transfer, **14**, No. 2, pp.201-209.
25. Al-Qahtani, M. S., Jang, Y. J., Chen, H. C., and Han, J. C., 2001, "Flow and Heat Transfer in Rotating Two-Pass Rectangular Channels (AR = 2) by Reynolds Stress Turbulence Model," submitted to the Int. J. Heat and Mass Transfer.

26. Stephens, M. A., Shih, T. I-P., and Civinskas, K. C., 1995, "Computation of Flow and Heat Transfer in a Rectangular Channel with Ribs," AIAA Paper 95-0180.
27. Stephens, M. A., Chyu, M. K., and Shih, T. I-P., 1996, "Computation of Convective Heat Transfer in a Square Duct with Inclined Ribs of Rounded Cross Section," ASME Paper 96-WA/HT-12.
28. Stephens, M. A. and Shih T. I-P., 1997, "Computation of Compressible Flow and Heat Transfer in a Rotating Duct with Inclined Ribs and 180Deg Bend," ASME Paper 97-GT-192.
29. Prakash, C. and Zerkle, R., 1995, "Prediction of Turbulent Flow and Heat Transfer in a Ribbed Rectangular Duct with and without Rotation," ASME J. of Turbomachinery, **177**, pp. 255-264.
30. Iacovides, H., 1998, "Computation of Flow and Heat Transfer Through Rotating Ribbed Passage," International J. of Heat and Fluid Flow, **19**, pp. 393-400.
31. Jang, Y. J., Chen, H. C., and Han, J. C., 2000a, "Computation of Flow and Heat Transfer in Two-Pass Channels with 60° Ribs," AIAA Paper 2000-1036, 38th Aerospace Science Meeting & Exhibit, Reno, NV, January 10-13.
32. Jang, Y. J., Chen, H. C., and Han, J. C., 2000b, "Numerical Prediction of the Flow and Heat Transfer in a Two-Pass Square Duct with 90° Ribs," *The 8th International Symposium on Transport Phenomena and Dynamics of Rotating Machinery (ISROMAC-8)*, Honolulu, HI, March 26-30, **1**, pp. 580-587.

33. Jang, Y. J., Chen, H. C., and Han, J. C., 2000c, "Flow and Heat Transfer in a Rotating Square Channel with 45° Angled Ribs by Reynolds Stress Turbulence Model," ASME Paper 2000-GT-0229.
34. Al-Qahtani, M. S., Jang, Y. J., Chen, H. C., and Han, J. C., 2001, "Prediction of Flow and Heat Transfer in Rotating Two-Pass Rectangular Channels with 45° Rib Turbulators," ASME Paper 2001-GT-0187.
35. Chen, H. C., Patel, V. C., Ju, S., 1990, "Solutions of Reynolds-Averaged Navier-Stokes Equations for Three-Dimensional Incompressible Flows," *J. of Computational Physics*, **88**, No. 2, 305-336.
36. Chen, H. C. and Patel, V. C., 1989, "The Flow Around Wing-Body Junctions", *Proceedings of the 4th Symposium on Numerical and Physical Aspects of Aerodynamic Flows*, Long Beach, CA.
37. Chen, H. C. and Chen, M., 1998, "Chimera RANS Simulation of a Berthing DDG-51 Ship in Translational and Rotational Motions", *International J. of Offshore and Polar Engineering*, **8**, No. 3, pp.182-191.
38. *GRIDGEN User Manual*, Version 13.3, Pointwise Inc., 1999.
39. Rohsenow, W. M., and Choi, H., 1961, *Heat, Mass and Momentum Transfer*; Prentice-Hall, Englewood Cliffs, NJ.

## **ONGOING WORK**

### **Part I: Rotating Heat Transfer**

- Dimple plates of three different dimple depths (10%, 20%, and 30% of dimple diameter) have been manufactured using and CNC mill.
- Heat transfer experiments are currently underway for AR=4:1 channel with 30% depth dimple plates. The 20% and 10% dimple plates will follow.
- Acrylic pins have been obtained for the pin-fin experiments. These experiments will follow the dimple experiments.
- The entry effect will be explored after the pin-fin experiments are finished. All test section inserts necessary to modify the test section inlet have been manufactured.
- Stationary pressure drop experiments are currently underway to determine the pressure drop in the dimple test sections. The test section is made of acrylic and will later be used for liquid crystal thermography experiments.

### **Part II: Stationary Heat Transfer and Flow Field**

- Construction of test sections: The pin fins are completed, the rib turbulators are completed, and the dimples are completed except for heater installation, which is presently underway by Electrofilm Corp. Valencia, Ca.
- Flow structure measurements: The pin fins are completed, the dimples are currently underway, and the rib turbulators are scheduled for the near future.

- Heat transfer measurements (data obtained at one temperature ratio and different Reynolds numbers): The rib turbulators are completed, the pin fins are scheduled for the near future, and the test section is currently being installed for these measurements. Also, the dimples are scheduled for the near future.
- Heat transfer measurements (data obtained at different temperature ratios and one Reynolds number): The rib turbulators are completed, the pin fins are scheduled for the near future, and the test section is currently being installed for these measurements. The dimples are scheduled for the near future.

### **Part III: Numerical Prediction**

- Boundary-fitted numerical grids were generated for a rectangular channel (AR = 4:1) with pin fins using the GRIDGEN code.
- Calculations of flow field, heat transfer coefficients, and pressure drops will be performed for the pin fin configurations under various combinations of rotation number, coolant to wall temperature ratio, and channel orientation. Both the two-layer k- $\epsilon$  model and near-wall second-moment closure model will be used to quantify the effects of Reynolds stress anisotropy.
- The numerical results will be compared to the experimental data obtained in the above-mentioned flow and heat transfer measurements to assess the general performance of the RANS code and turbulence models.
- Boundary-fitted numerical grids will be generated for a rectangular channel (AR = 4:1) with dimples using the GRIDGEN code.

- Calculations of flow field, heat transfer coefficients, and pressure drops will be performed for the dimple configuration under various combinations of rotation number, coolant to wall temperature ratio, and channel orientation. Both the two-layer k- $\epsilon$  model and near-wall second-moment closure model will be used to quantify the effects of Reynolds stress anisotropy.
- The numerical results will be compared to the experimental data obtained in the above-mentioned flow and heat transfer measurements to assess the general performance of the RANS code and turbulence models.

## **APPENDIX I: FIGURES FOR PART 1**

## **APPENDIX II: FIGURES FOR PART 2**

## **APPENDIX III: FIGURES FOR PART 3**



---

## Advanced Thermostructural Materials

Materials Department and  
Department of Mechanical and Environmental Engineering  
University of California  
Santa Barbara, CA, 93106-5050

---

# A SCIENCE BASED APPROACH TO ENHANCED ZIRCONIA-BASED THERMAL BARRIER COATINGS FOR ADVANCED GAS TURBINE APPLICATIONS

**Semi-annual report covering the period**

1 February 2001 - 31 July 2001

Contract No: 01-01-SR093 (DOE-SCERDC)

to

### Advanced Gas Turbine Systems Research Program

South Carolina Institute for Energy Studies  
Clemson, South Carolina 29634-5180  
Program Manager: Dr. Richard A. Wenglarz

*Principal Investigators:*

D.R. Clarke, C.G. Levi, and A.G. Evans

The support of the Department of Energy through the AGTSR program, administered by the South Carolina Institute for Energy Studies, is gratefully acknowledged. The research described in this report has benefited from the active support and advice of the industrial members of the AGTSR consortium, notably Siemens-Westinghouse, Solar Turbines, General Electric CRD/Aircraft Engines, UTRC/Pratt & Whitney, and Howmet.



August 30, 2001

## EXECUTIVE SUMMARY

Work has initiated in the major areas of study aimed towards developing a science-based approach to enhancing the properties of zirconia-based materials for advanced thermal barrier applications in gas turbine engines. This includes: a) the development of refined models for thermal cycling induced damage in plasma sprayed coatings; b) investigation of alternate stabilizers of the tetragonal-prime ( $t'$ ) phase for higher temperature operation; c) the effect of different dopants on the optical absorption properties of zirconia in the infra-red; d) the chemical compatibility between monazite and sodium vanadate and sodium sulfate and the suitability of monazite as a superficial, protective layer against vanadate and sulfate attack; e) the effect of TBC sintering on life.

Substantial progress has been made in both modeling thermal cycling induced damage in plasma sprayed coatings and in the development of phase equilibria for alternate rare-earth element stabilizers and this is described in the attached, more detailed technical summaries. In the area of the effects of different dopants on infra-red absorption, series of samples with different potential absorber ions have been prepared and initial characterization is underway. Thermal barrier coatings with infiltrated monazite have been prepared. These will be used to begin the assessment of chemical compatibility with both sodium vanadate and sodium sulfate. Systematic experiments to quantify the extent of sintering of thermal barrier coatings, attached to a bond-coated superalloy, as a function of time and temperature are underway. A number of sintering mechanisms have been identified and will be evaluated in the coming contract period.

Although not in the original proposal, we have deposited gadolinium zirconate ( $Gd_2Zr_2O_7$ ) thermal barrier coatings by electron beam deposition in our facility and demonstrated that it is possible to use photostimulated luminescence from the underlying thermally grown oxide to probe the oxide itself. This demonstrates that photostimulated luminescence can be used as a non-destructive tool with the new  $Gd_2Zr_2O_7$  coatings just as it being used for zirconia coatings.

Experiments to investigate thermal cycling induced "rumpling" of CoNiCrAlY bond coats that will be used in support of the models of thermal cycling have not yet begun. We await delivery of a series of samples promised by our industrial partners. They themselves, however, are awaiting the requested materials from their vendors. Despite the delays, we prefer to study the bond coats promised rather than make up our own so that the results will be of direct value to our partners.

The education and training aspects of the program are also well underway. Two graduate students are now working exclusively on the program and another is expected to join this Fall. We have been fortunate to have two summer students working in our laboratories over the summer actively involved in several of the experiments. In addition, we have established a weekly meeting in which issues related to TBC are discussed and tutorials on specific topics are given by the faculty. We have also been fortunate to have several visitors speak to this group, including Ken Murphy (Howmet), Ram Darolia and Dave Wortman (GE) and Bertrand Saint-Ramond (SNECMA).

## SUMMARY OF TECHICAL PROGRESS

### **Thermal Cycling of Plasma Sprayed Thermal Barrier Coatings**

Various investigations have probed the failure mechanisms that arise in plasma sprayed TBCs. The generally agreed-upon finding is that failure occurs by delamination, proceeding along a trajectory within the TBC, just above the TGO. Locally, near the peaks of the oscillations, the delamination may penetrate the TGO and extend along the TGO/bond coat interface. The details have been elusive, because of the difficulties in making sequential observations of events occurring near the interface and because all of the phenomena that affect the stress have yet to be included in a simulation scheme. In order to address the latter deficiency, a full numerical simulation scheme has been developed and prototypical stress distributions calculated.

The system comprises a bond coat with sinusoidal oscillations, amplitude A and wavelength,  $2L$ . The TBC is considered to be elastic with anisotropic in-plane Young's modulus in the range,  $E_{tbc} = 20 - 100 \text{ GPa}$ . The bond coat has temperature-dependent yield strength. The strength up to temperature  $T_1$  (taken as 300C in all calculations) is 1 GPa. At temperatures above  $T_2$ , the strength  $\mathbf{S}_{Y\min}^{tbc}$  is allowed to vary in the range 50 to 200 MPa. It changes linearly from  $T_1 \rightarrow T_2$ . The bond coat is assigned a thermal expansion misfit with the superalloy substrate. For most calculations it is taken as:  $\Delta\mathbf{a}_s = +3 \text{ ppm/C}$  ( $\Delta\mathbf{a}_s = \mathbf{a}_{\text{sub}} - \mathbf{a}_{bc}$ ). Stress redistribution in the TGO is simulated by allowing the TGO to yield when the Mises stress reaches  $\pm 1 \text{ GPa}$ , imposing a maximum on the growth stress. On cooling and reheating it behaves elastically, because of the rapid increase in yield strength at lower temperatures. The misfit stress at ambient then equals the sum of that from growth with that from thermal expansion misfit ( $\mathbf{S}_{\text{ambient}} \approx -4.5 \text{ GPa}$ ). From past experiences with EB-PVD systems, these choices of properties appear to capture the principal non-linearities as well as their effect on stresses and displacements. In the simulations the temperature is cycled over a range,  $\Delta T = 1000 \text{ C}$  and the stresses monitored.

The stresses having greatest relevance to delamination are those normal to the interface,  $\mathbf{S}_{zz}^{tbc}$ , since they prescribe the energy release rate experienced by potential delamination cracks. The stresses are normalized by the misfit stress,  $\mathbf{S}_o^* = E_{tbc} \Delta\mathbf{a}_{tbc} \Delta T / (1 - \mathbf{n}_{tbc})$ . A typical result for the stress in the TBC normal to the interface with the TGO,  $\mathbf{S}_{zz}^{tbc}$  (figure 1 A, B), indicates some general features relevant to TBC cracking. At ambient, in a small region around the apex, the stress is compressive. Elsewhere, the TBC experiences a relatively uniform  $\mathbf{S}_{zz}^{tbc}$  tension. The stresses increase as the system cycles, because of the displacements caused by the thickening of the TGO: albeit, within a single cycle, the magnitude is almost the same at both ambient and elevated temperature. The peak  $\mathbf{S}_{zz}^{tbc}$  tension, which occurs just beyond the apex (figure 1), increases in a nominally linear manner with the number of cycles, N. *This increase in stress with N is a prerequisite for cyclic cracking in the TBC.* None of the previous attempts at simulation has demonstrated this systematic stress increase in the TBC.

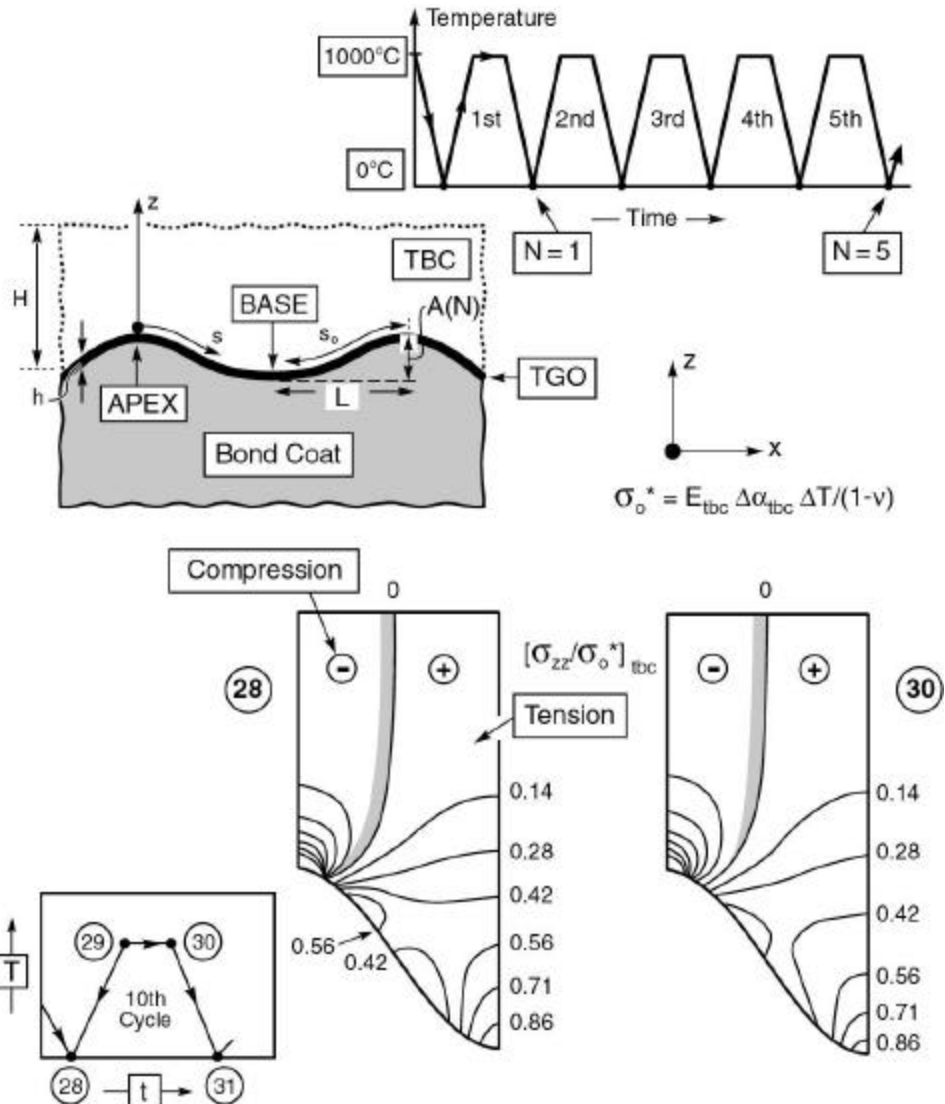


Figure 1A

Ming, Plasma Fig. #3A.

Figure 1A. (Top). The sinusoidal shape used to represent the interface between a plasma-sprayed coating and the bond coat and some of the pertinent parameters used in the analysis. (Bottom) The development of a tensile and compressive stress field in the TBC on thermal cycling. In this example, the stresses are shown for the 28<sup>th</sup> and 30<sup>th</sup> cycle.

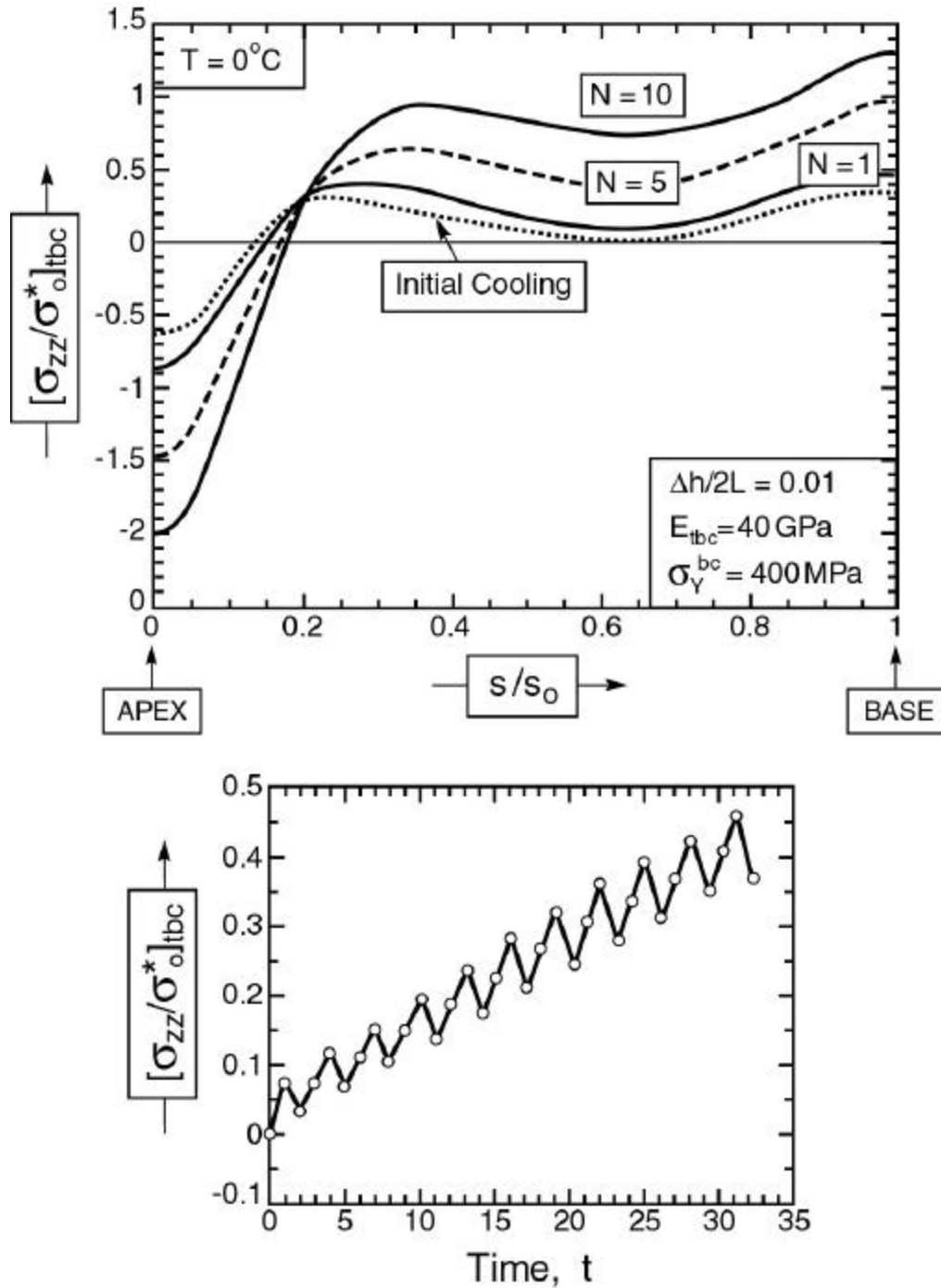


Figure 1B

Ming Plasma, Fig. #3B

Figure 1B. The increase in normal stress with number,  $N$ , of thermal cycles as a function of position along an interface from apex to base (top) and the variation in peak normal stress with number of cycles (bottom)

### **Alternate Stabilizers.**

Studies on the potential use of alternate stabilizers have been initiated, seeking improved understanding of the effects of gradually substituting rare-earth cations for Y. The initial work has focused on two issues:

1. Establishing the basic features of the  $\text{ZrO}_2$ -REO phase equilibrium for the systems and regions of interest, with emphasis on Gd additions as specified in the proposal.
2. Exploring the relative stabilizing efficiency of Y, Gd and La at the same level of cation substitution, corresponding to the nominal concentration of YSZ.

### Phase Equilibria.

The additions of initial interest are Y, Gd and La, representing the conventional YSZ and two alternate stabilizers with different ionic sizes, both larger than Y. The  $\text{ZrO}_2$ - $\text{YO}_{1.5}$  system has been extensively studied but some regions are still under debate, particularly the lower temperature equilibrium on the  $\text{ZrO}_2$ -rich end. There is also a proposed  $\text{ZrO}_2$ - $\text{LaO}_{1.5}$  system, although less studied and arguably more uncertain than that for Y. In contrast, very little is known about the  $\text{ZrO}_2$ - $\text{GdO}_{1.5}$  binary equilibrium, with the exception of some data on the liquidus and the order-disorder transformation for the pyrochlore phase. Hence, the initial goal has been to outline the binary diagram for this system.

Samples with different concentrations of  $\text{GdO}_{1.5}$  and  $\text{YO}_{1.5}$  were prepared from mixed precursor solutions. (The  $\text{YO}_{1.5}$  samples were intended to ascertain the reliability of the method and provide comparison with  $\text{GdO}_{1.5}$  materials of similar composition.) The solutions were flash-dried by spraying them onto a hot (300°C) Teflon-coated surface to minimize segregation. The resulting powders were pyrolyzed at 900°C, pelletized, heated to 1600°C for 24 h, and then to 1200°C for an additional 168 h (one week). Phase composition after this treatment was undertaken by X-ray diffractometry. Some samples were also examined by Raman spectroscopy, which is more sensitive than XRD for detecting small amounts of tetragonal or monoclinic phases.

The results are summarized in Figure 2, which depicts a tentative 1200°C isothermal section in the  $\text{ZrO}_2$ - $\text{YO}_{1.5}$ - $\text{GdO}_{1.5}$  ternary and the corresponding  $\text{ZrO}_2$ -REO binaries. The results for the  $\text{ZrO}_2$ - $\text{YO}_{1.5}$  are in remarkable agreement with the thermodynamic assessment of Du et al.<sup>1</sup>, except for the  $\delta$ -zirconate which retained the disordered fluorite structure even after the relatively lengthy heat treatment. The Gd samples behaved quite similarly to the corresponding Y compositions, although in this case the zirconate phase did show clear evidence of ordering to the pyrochlore form. Based on these preliminary results and the expected behavior of the system, the tentative diagram in Figure 2 is drawn with similar features to the  $\text{ZrO}_2$ - $\text{YO}_{1.5}$  system. Further work is necessary to confirm the proposed diagram and outline the Gd-rich end, but the present results provide sufficient insight to proceed with the exploration of the ternary, which is now ongoing.

---

<sup>1</sup> Y. Du, Z. Jin and P. Huang, J. Am. Ceram. Soc., **74** 1569 (1991).

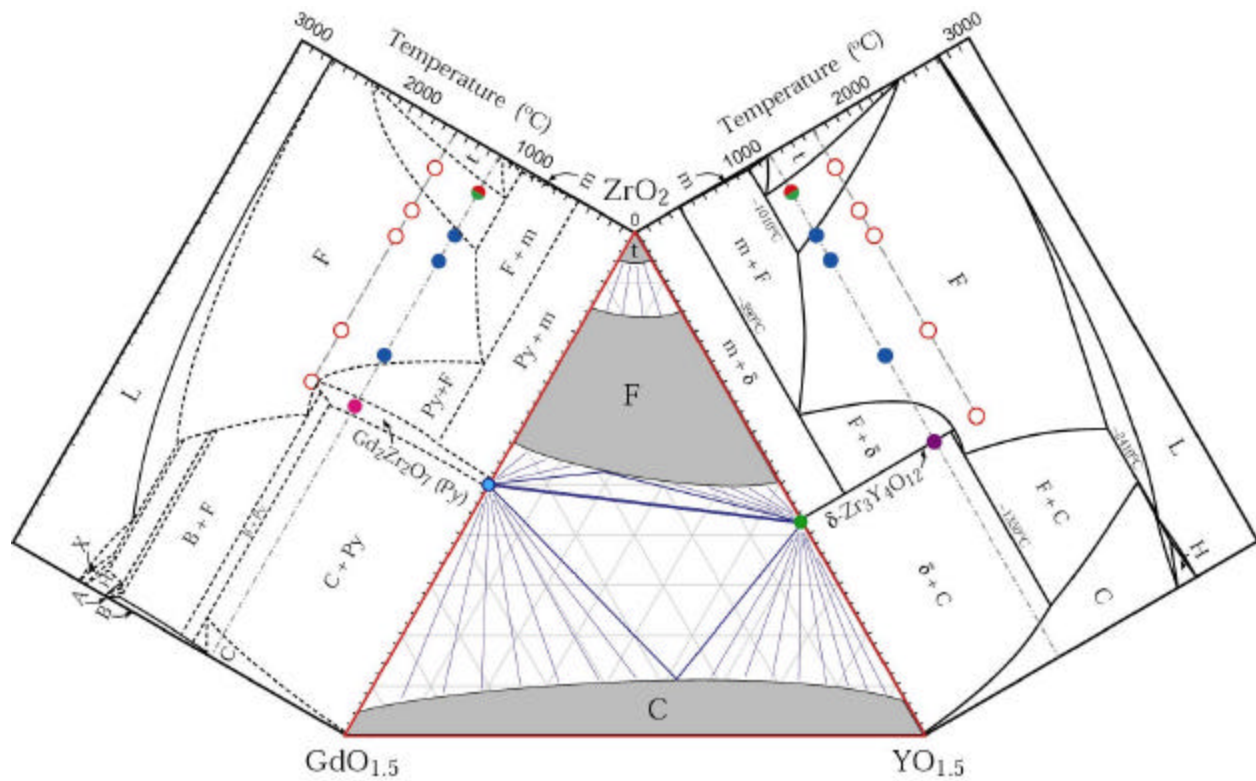


Figure 2. Tentative ternary section for the  $\text{ZrO}_2$ - $\text{GdO}_{1.5}$ - $\text{YO}_{1.5}$  at  $1200^\circ\text{C}$ , and corresponding binaries. The colored circles represent experimental compositions and the heat treatments to which they were subjected. Note that the 7.6% composition exhibits partitioning because of the 24 h exposure at  $1600^\circ\text{C}$ .

The above results, albeit preliminary, are consistent with the proposed strategy based on mixed stabilizer compositions. (Literature results for Sc-Y mixtures are consistent with this view, although in that study the Sc was proposed as the main stabilizer.) The addition of the RE would then be tailored for optimum effect on the optical properties, as noted in the original proposal.

Future work in this area involves the investigation of selected compositions within the t' domain in the ternary systems, i.e. on the ZrO<sub>2</sub>-rich side of the t/F T<sub>0</sub> surface. Compositions will be synthesized with different Y:Gd ratios and different levels of total stabilizer content (still within the t + F field). Following the experience with the binaries, it is anticipated that the boundary of the F ternary field can be readily established. The practical lower bound will be estimated by determining the transformability of single phase tetragonal compositions. The samples will be heat treated and characterized, both in terms of their phase composition as well as their optical properties.

---

<sup>2</sup> This is a requirement that is not always followed in the literature, leading to inappropriate and sometimes misleading comparison of results. The 7.6%REO<sub>1.5</sub> corresponds to the nominal 7 wt.% Y<sub>2</sub>O<sub>3</sub> in commercial TBCs.

### Photostimulated Luminescence Through $\text{Gd}_2\text{Zr}_2\text{O}_7$ Coatings

As a complementary activity to the phase equilibria studies of the  $\text{ZrO}_2\text{-GdO}_{1.5}$  system and their extension to the compatibility with alumina, we have deposited a number of  $\text{Gd}_2\text{Zr}_2\text{O}_7$  coatings using the electron beam deposition facility at UC Santa Barbara. With these films we have demonstrated that the non-destructive technique of photostimulated luminescence that is increasingly being used to probe zirconia coatings can equally be used for non-destructive evaluation with a gadolinium zirconate coatings. An illustrative spectrum is reproduced in figure 3 for a gadolinium zirconate coating on an oxidized FeCrAlY substrate. This will be explored further if it is of interest to any of the industrial partners.

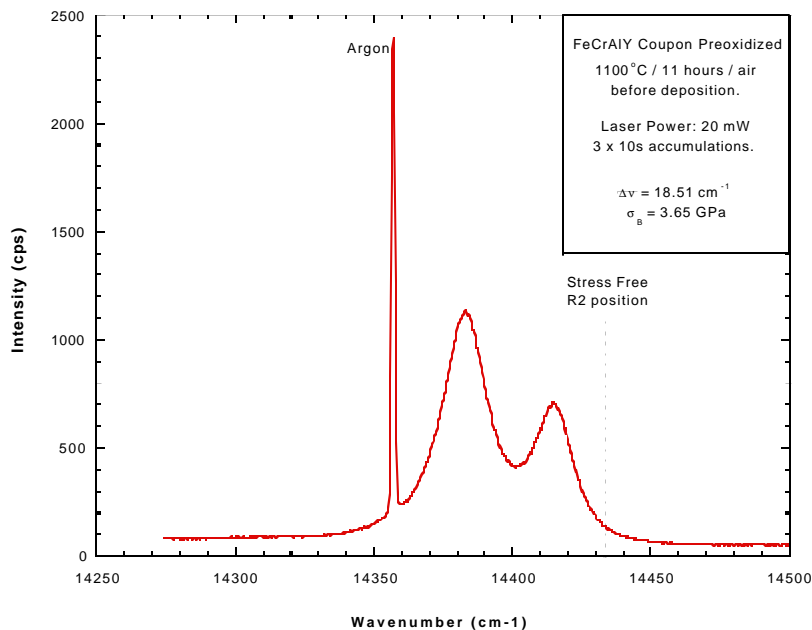


Figure 3. Photostimulated R-line luminescence from a thermally grown oxide formed beneath an electron-beam deposited gadolinium zirconate coating to demonstrate that the viability of non-destructive evaluation of stresses in the TGO is unaffected by replacing the YSZ with a  $\text{Gd}_2\text{Zr}_2\text{O}_7$  material.

**UNIVERSITY OF MINNESOTA**

**Heat Transfer Laboratory**

**Department of Mechanical Engineering**

**Minneapolis MN 55455**

**Report for the Project Entitled**

**EDGE COOLING HEAT TRANSFER**

For the period

1 August 2000–31 January 2001

**Submitted to**

Dr. Richard Wenglarz

AGTSR Program, Clemson University

**Submitted by**

**R.J. Goldstein<sup>1</sup>**, co-principal investigator

**C. Camci<sup>2</sup>**, co-principal investigator

<sup>1</sup> Regents Professor and James J Ryan Professor  
Department of Mechanical Engineering  
University of Minnesota

<sup>2</sup> Professor of Aerospace Engineering  
Center for Gas Turbines and Power  
Pennsylvania state University

Contact person for this report:  
Dr. R.J. Goldstein,  
232 Mechanical Engineering  
111 Church Street SE  
University of Minnesota  
Minneapolis MN 55455  
612 625-5552 rjg@me.umn.edu

This report summarizes the work done in the Heat Transfer Laboratory during the past six months under the proposal on Edge Cooling Heat Transfer.

Various studies in the literature have dealt with the effect of relative motion on the heat transfer to the tip of rotor blades. Most of these studies have found no deviation from the model of Mayle and Metzger(1982) which essentially states that the flow in the tip resembles the entrance flow in a duct, and that the boundary layers on the blade tip and the endwall do not influence each other unless the flow path of the gas in the clearance exceeds about 20 gap heights, in which case a slight increase is predicted. However, recent flow measurements (Yaras and Sjolander, 1992a,1992b) with a moving endwall have pointed out a reduction in the pressure differential across the blade tip that drives the flow. This is probably due to the endwall motion causing changes in the secondary flow structure in the turbine passage, notably dragging of the passage vortex formed due to endwall secondary flows towards the suction side of the blade, and its consequent interaction with the tip leakage vortex. This would likely reduce the leakage strength, and also reduce the magnitude of heat transfer to the blade tip, contrary to the model of Mayle and Metzger.

To test this hypothesis, an apparatus was built that simulates the relative motion between the casing endwall and the blade tip that could be used in the linear cascade in the Laboratory. The apparatus consists of a 2kW 3-phase induction motor, a rubber belt, three rollers on which the moving wall rotates, and two pitch pulleys which transmit power from the motor to the belt. The whole apparatus rests on an aluminium base that fits onto the top wall of the linear cascade.

The belt is made of N-8 Sampla synthetic rubber that is placed flush with the inner top wall of the test section. The belt moves from the direction of the suction side of the stationary blade to the pressure side, thus simulating the rotation of a rotor blade in a gas turbine engine. The third roller has an adjustable axis of rotation and is used to keep the belt tight and to prevent tracking of the belt from side to side. The motor speed is controlled using an Ativar ATV 18 speed drive controller. It was experimentally verified that the flapping effect of the belt due to vibrations during operation resulted in a variation of not more than 0.1% of chord. A schematic diagram of the moving wall apparatus is shown in fig. 1. With the motor operating at its rated speed of 3250 rpm, the reduction in speed through the pulleys produces a belt speed of 25 m/s. In order to simulate engine-representative velocity ratios, the wind tunnel is operated at a speed of 12.5 m/s. Further details of the apparatus are available in srinivasan (2000).

## Results

Mass transfer tests conducted with and without the moving endwall in operation show that the effect of relative motion on mass/heat transfer from the blade tip is, at best, slight at low clearances, and negligible at larger clearances. Figs. 2 and 3 show the effect of relative motion on the blade tip mass transfer at various chordwise locations for a clearance of 0.6% of chord ( $\tau/C=0.6\%$ ). It can be seen that there is a slight reduction in local mass transfer at each location with the introduction of the moving wall. At a larger clearance of 0.86% (figs. 4 and 5), the slight reduction is observed over the forward half of the blade, while there is an increase due to rotation over the rear half of the blade. At all higher clearances, there is virtually no effect of endwall

motion on the blade tip mass transfer. Fig. 6 shows data obtained for a clearance of 1.72% of chord with and without endwall motion. Tests at all higher values of tip clearance ( $\tau/C=3.45\%, 6.9\%$ ) showed the same behaviour.

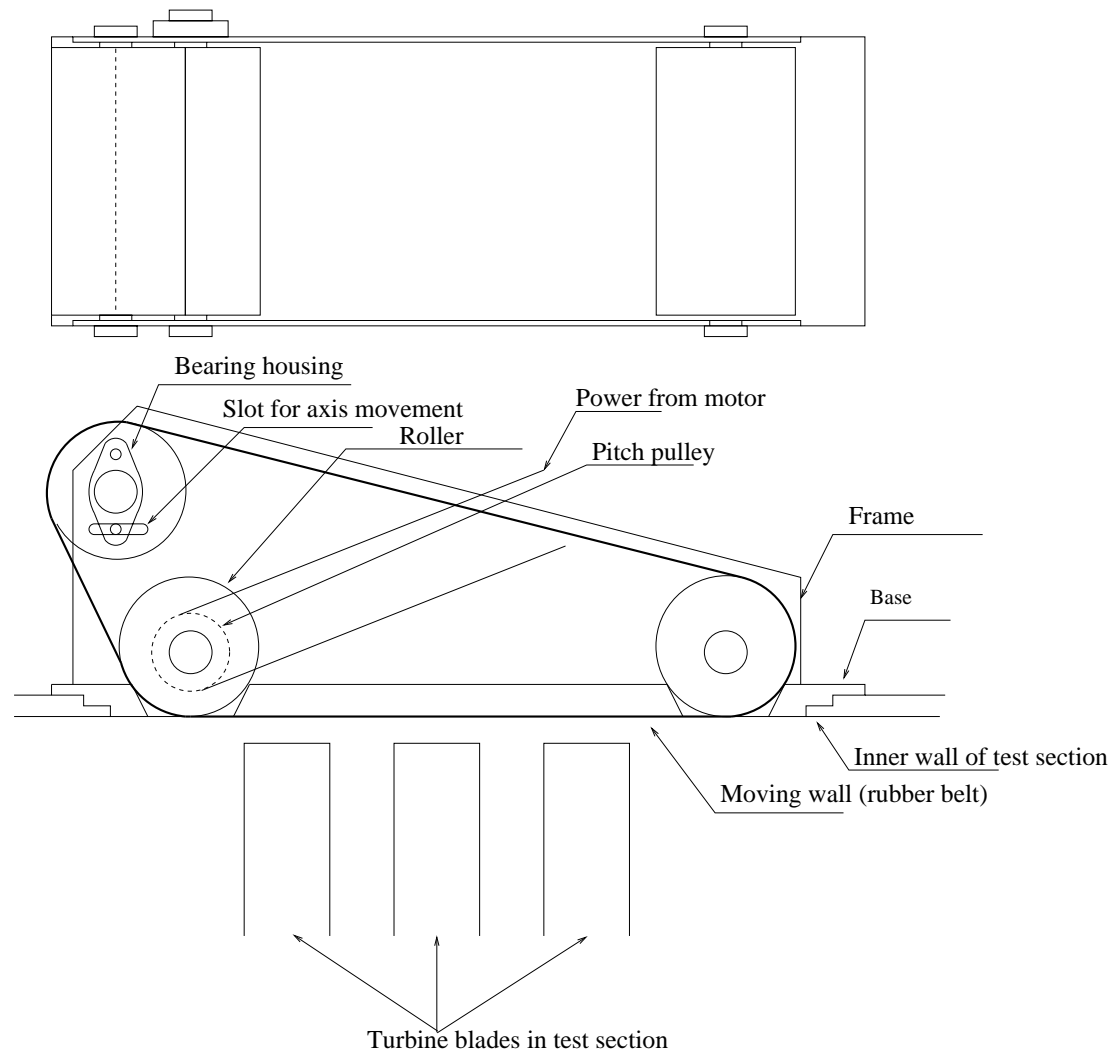


Figure 1. Schematic diagram of the moving wall apparatus

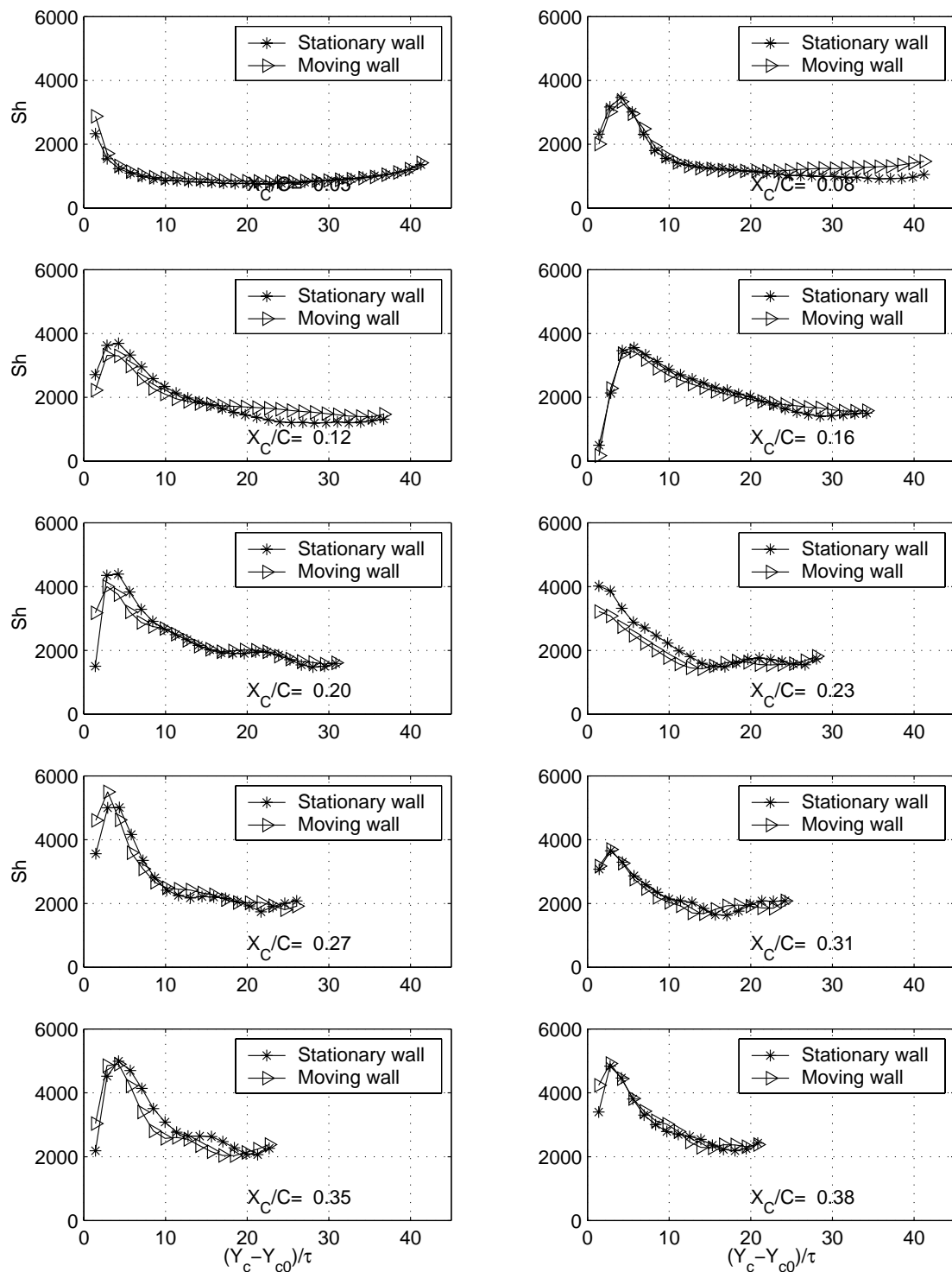


Figure 2. Sherwood number for the forward half of the blade for  $\tau/C=0.6\%$

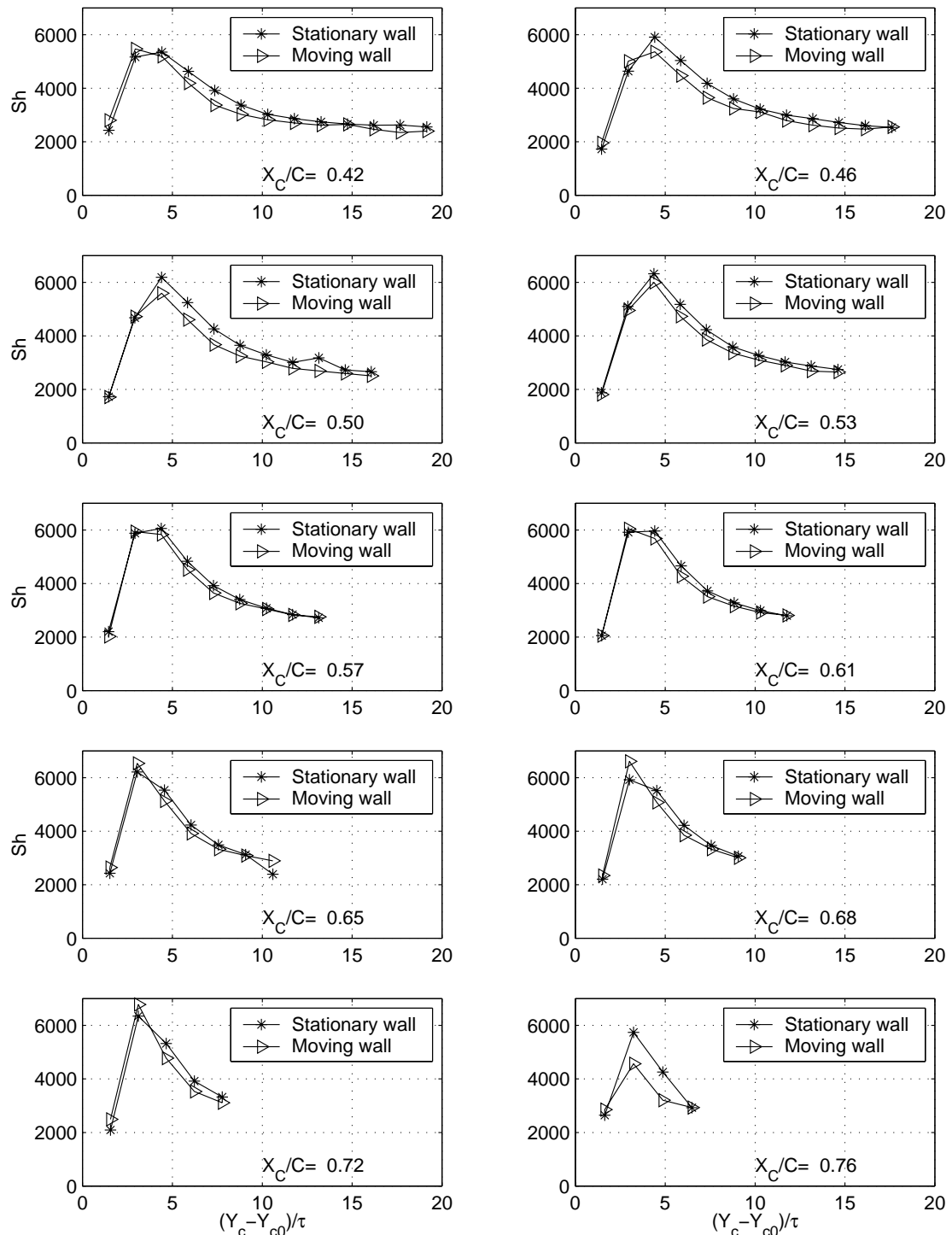


Figure 3. Sherwood number for the rear half of the blade for  $\tau/C=0.6\%$

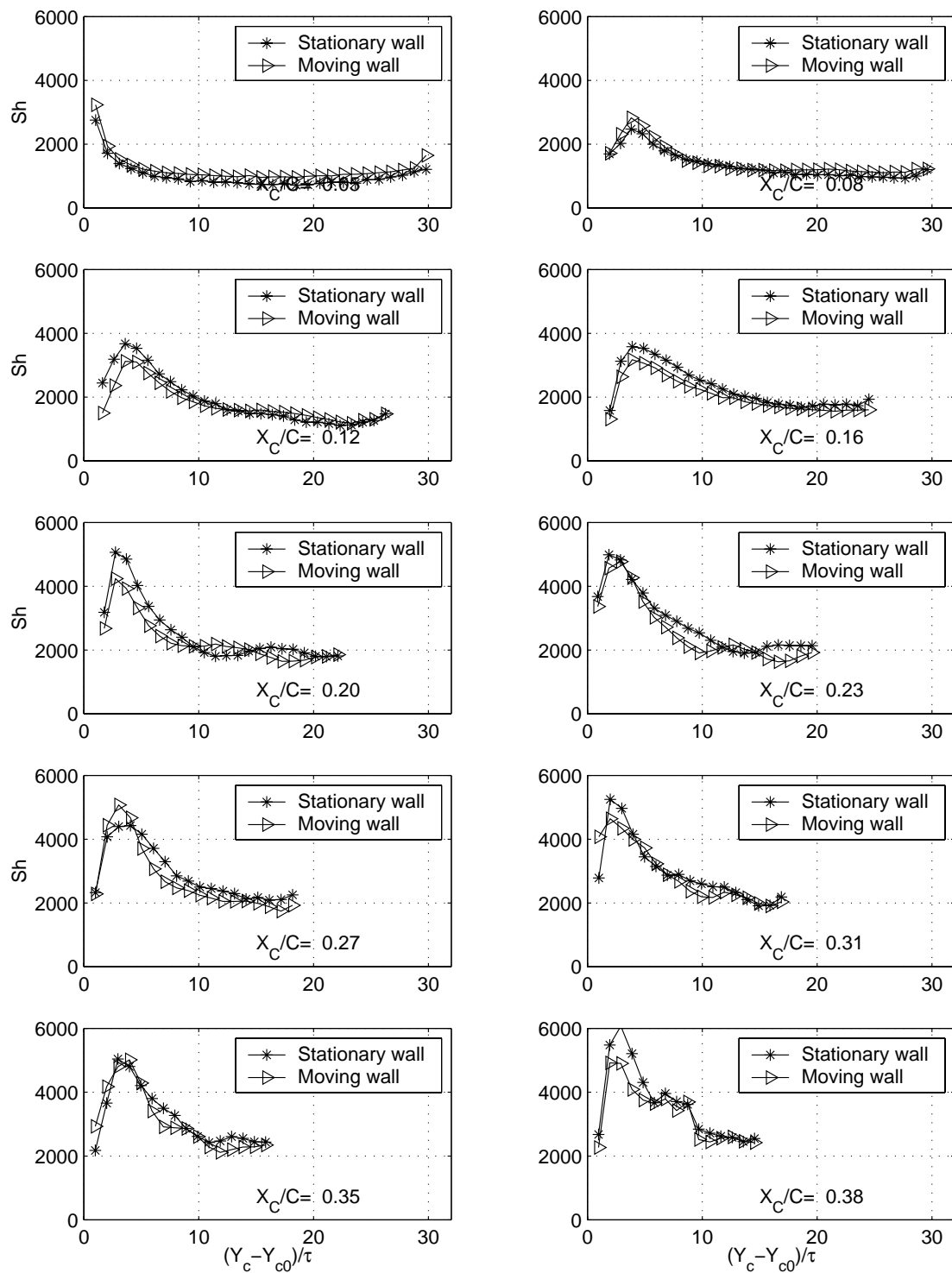


Figure 4. Sherwood number for the forward half of the blade for  $\tau/C=0.86\%$

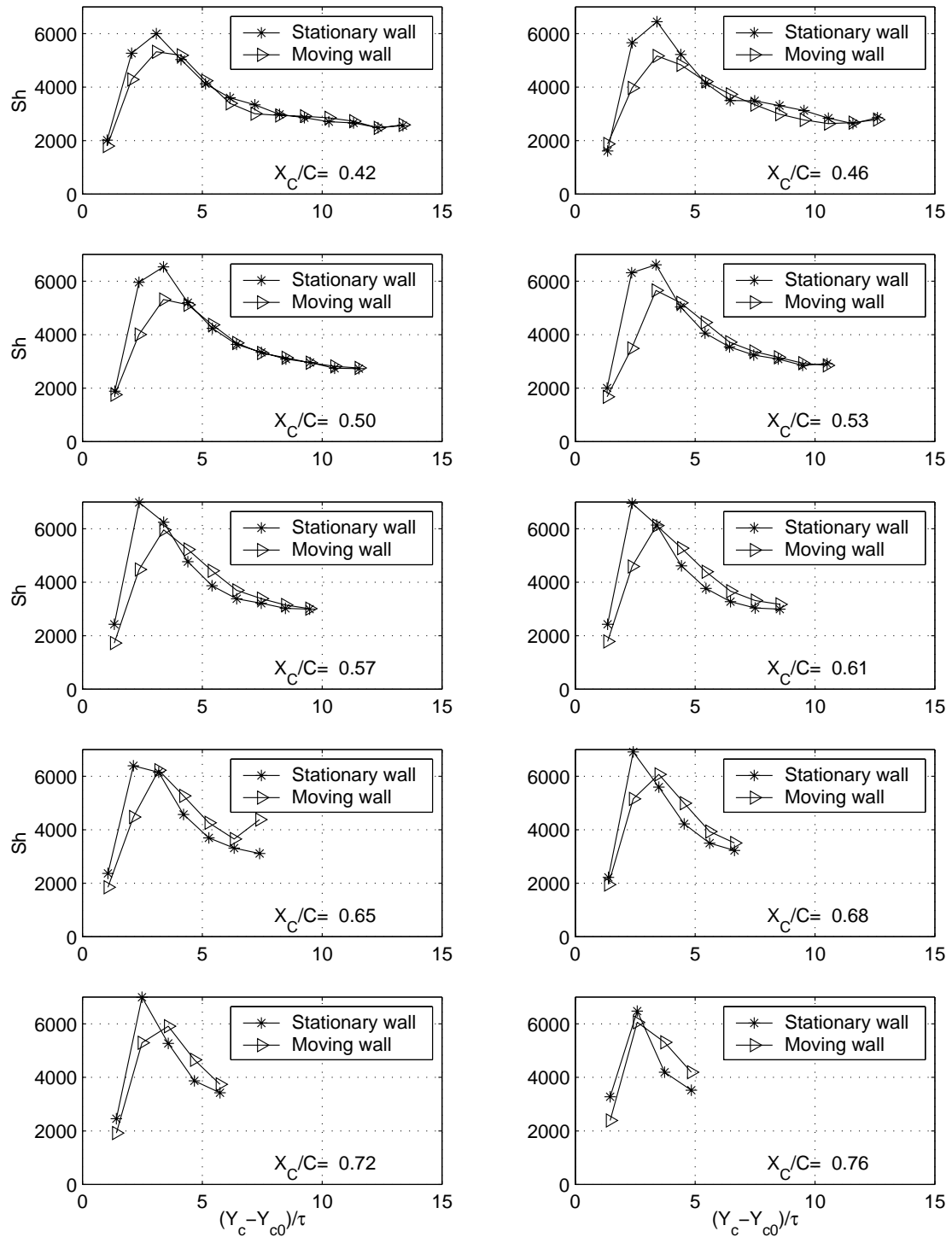


Figure 5. Sherwood number for the rear half of the blade for  $\tau/C=0.86\%$

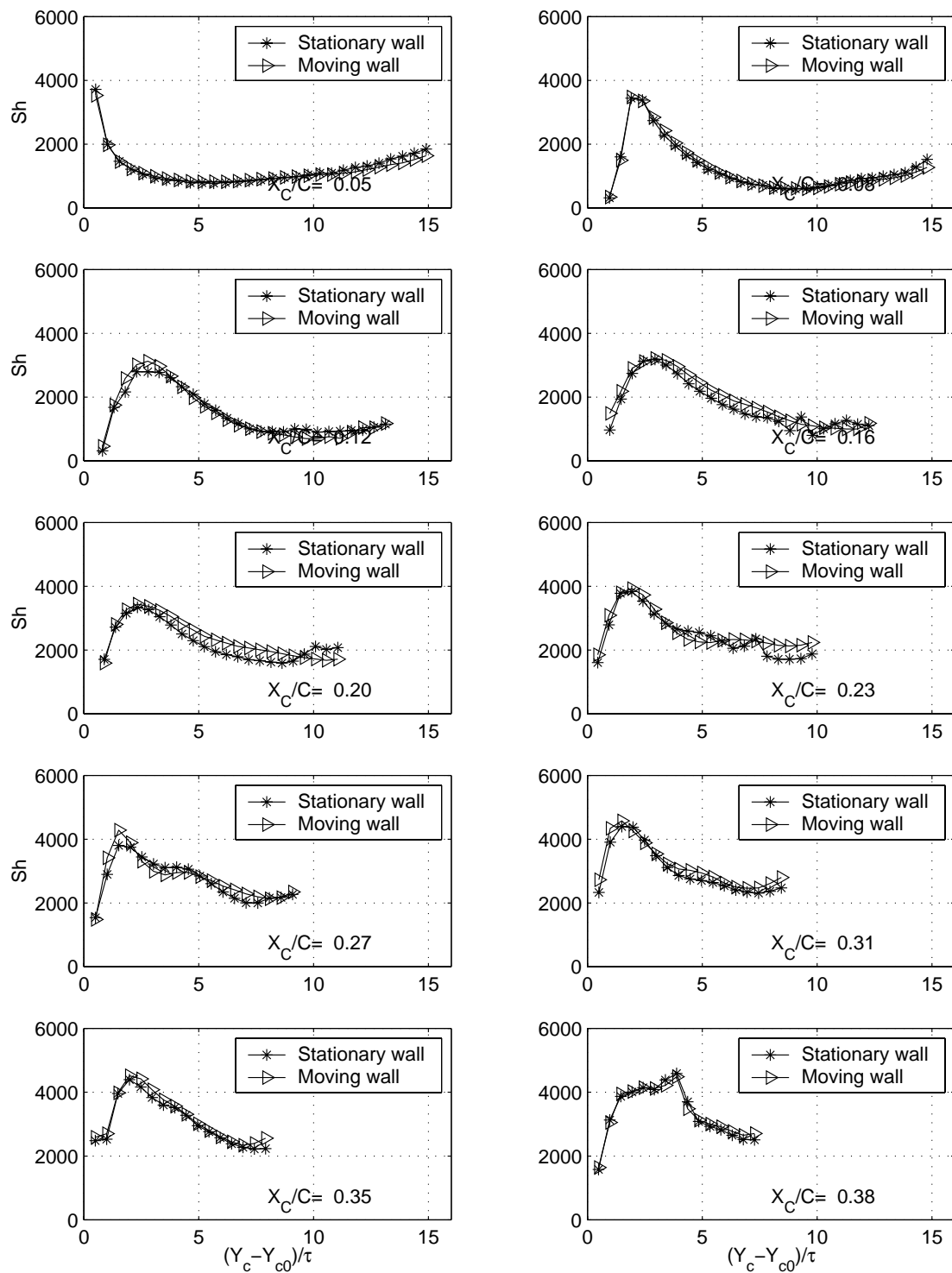


Figure 6. Sherwood number for the forward half of the blade for  $\tau/C=1.72\%$

## References

Mayle, R.E. and Metzger, D.E., 1982. *Heat Transfer At The Tip Of An Unshrouded Turbine Blade*, Proceedings of the Seventh International Heat Transfer Conference, vol. 3, pp. 87-92.

Yaras, M.I. and Sjölander, S.A., 1992a. *Effects of Simulated Rotation on Gap Leakage Flow in a Planar Cascade of Turbine Blades: Part I- Tip Gap Flow*, Journal of Turbomachinery, vol. 114, pp. 652-659.

Yaras, M.I. and Sjölander, S.A., 1992b. *Effects of Simulated Rotation on Gap Leakage Flow in a Planar Cascade of Turbine Blades: Part I- Downstream Flow Field and Blade Loading*, Journal of Turbomachinery, vol. 114, pp. 660-667.

Srinivasan, V., 2000. *Effect of Simulated Rotation on the Mass/Heat Transfer From the Tip of a Turbine Blade*, Master's Thesis, University of Minnesota.

**Interaction of Steam/Air Mixtures  
With Turbine Airfoil Alloys and Coatings**

1 February 2001 – 31 July 2001

Semi-Annual Report

Gerald H. Meier and Frederick S. Pettit, Principal Investigators  
Kivilcim Onal, Student Researcher

Department of Materials Science & Engineering  
848 Benedum Hall  
University of Pittsburgh  
Pittsburgh, PA 15261

Subcontract No. 99-01-SR077  
Clemson University Research Foundation  
South Carolina Energy Research and Development Center  
Clemson, South Carolina 29634-5181

September 1, 2001

This report was prepared with the support of the US Department of Energy,  
Morgantown Energy Technology Center, Contract Number DE-FC21-92MC29061

## **Executive Summary**

AGSTR Semi-Annual Report

Department of Materials Science and Engineering

848 Benedum Hall

University of Pittsburgh

Pittsburgh, PA 15261

Ph: (412) 624-9720 or 624-9730                  Fax: (412) 624-8069

Project Title: Interaction of Steam/Air Mixtures With  
Turbine Airfoil Alloys and Coatings

AGSTR Subcontract No. 99-01-SR077

Principal Investigators: F. S. Pettit ([pettit@engrng.pitt.edu](mailto:pettit@engrng.pitt.edu))  
G. H. Meier ([ghmeier@engrng.pitt.edu](mailto:ghmeier@engrng.pitt.edu))

Research Student: Kivilcim Onal

Subcontract Inf:      Department of Mechanical Engineering  
                          Carnegie Mellon University  
                          5000 Forbes Avenue  
                          Pittsburgh, PA 15213-3890  
                          Jack L. Beuth ([beuth@andrew.cmu.edu](mailto:beuth@andrew.cmu.edu))

Start Date:      February 1, 1999

## **Status and Results for the Reporting Period**

Some gas turbine engines use steam injection to augment power and reduce emissions. Field experience shows that hot section distress is typically more severe in these steam injection engines. The interaction of steam/air mixtures with the turbine airfoil materials and/or coatings is not understood. This program seeks to discover how high temperature and pressure steam affects the oxidation characteristics of current and future alloy/coating systems on external airfoil surfaces. In order for the results from such studies to be applicable to actual gas turbines, testing will be performed under simulated dynamic operating conditions. The program plan is to study the oxidation of the relevant alloys/coatings in three existing apparatuses, two at the University of Pittsburgh and the third at Oak Ridge National Laboratory. All three apparatuses are currently operational. By using these three apparatuses, studies can be performed that will permit the effects of temperature, gas velocity, steam-air ratios, and total pressures on oxidation to be understood. An important feature of this program is that the test conditions extend over ranges that will permit oxidation mechanisms and models to be developed, while also permitting alloy performances to be ranked and models tested under conditions simulating operating conditions in gas turbines.

In this program it is also planned to experimentally determine the effects of steam on the adhesion of the oxide layers to the various alloys and coatings, and also to determine if applied stresses affect the oxidation of these alloys in steam. These studies are being performed at Carnegie Mellon University.

The data generated in this program is to be used as follows:

1. Mechanisms will be developed to describe how water vapor influences the growth rates and adherence of alumina and chromia scales on superalloys/coatings.
2. The effect of temperature, over the ranges 700-1100°C (1292-2012°F) for alumina-forming alloys/coatings and 700-900°C (1292-1652°F) for chromia-forming alloys, on oxidation degradation will be determined.
3. The effect of water vapor partial pressure at total pressures extending from 1 to 15 atm on the degradation rates of superalloys/coatings will be described.
4. The effect of gas velocity (from 0.07 cm/s to Mach 0.5) on the degradation rates of superalloys/coatings will be described.
5. The oxidation behavior of the various alloys/coatings will be ranked under conditions simulating gas turbine operating conditions, and the effects of items 2 to 4 will be used to attempt to formulate life prediction models.
6. The technology and understanding developed in this program will be transferred to the industrial collaborators and other ATS participants.

This program has been worked upon for 2 ½ years. Cyclic oxidation tests at 900°C in dry air and in air with 0.3 atm of steam have been performed for 1600 hrs on Mar M 247, X-40, IN 738, CM 186, N5 and PWA 1484. These alloys have also been exposed isothermally at 900°C to steam at a pressure of 250 psi. The major effects of steam at 900°C has been to cause more severe cracking and spalling of oxide scales. This cracking and spalling of oxide occurs at water vapor pressures of 0.3 atm under cyclic conditions and higher pressures of steam (250 psi) under isothermal conditions did not cause more severe degradation. The alloys that developed Cr<sub>2</sub>O<sub>3</sub> during oxidation (i.e. X-40, IN 738) were degraded more than alloys that developed α-Al<sub>2</sub>O<sub>3</sub> scales (i.e. N5, PWA 1484, CM 186).

Water vapor also caused increased degradation at 700°C but the major cause of this degradation was due to less effective selective oxidation of aluminum in the alloys. The alumina-formers were more substantially affected by this phenomenon than the chromia-formers. These effects occurred during cyclic oxidation with a water vapor pressure of 0.3 atm. As observed at 900°C, the presence of steam at 250 psi during isothermal oxidation did not cause as much degradation as steam at lower pressures under cyclic oxidation conditions.

Experiments have also been performed to examine the effects of gas velocity and externally applied stresses during oxidation in dry and wet air. More work must be done but currently these two factors have not been found to substantially affect the oxidation behavior of the alloys that have been studied.

Finally, the influence of steam on the failure of TBCs using an indent test have been studied. Initial results indicated that steam may cause the fracture toughness of TBCs to decrease more rapidly than dry air during exposures at 1100°C. However, the as processed fracture toughnesses of the TBC specimens have been determined to vary and this may have been the cause of the effects observed in the tests with steam.

Over the next six months of the program the technical efforts on all tasks will be completed.

## Introduction

Hot section distress in gas turbines is typically more severe when steam injection is used. The data that exists in the literature shows that steam, or water in the gaseous state, can have a variety of effects on the oxidation of alloys.<sup>1-9</sup> These effects depend upon the alloy under consideration, the oxidation temperature, the water vapor pressure, and the gas flow rate. Water vapor has been found to affect the high temperature oxidation of alloys in the following ways through the following mechanisms:

- The presence of water vapor permits a H<sub>2</sub>-H<sub>2</sub>O mixture to be formed in voids which facilitates a rapid inward transport of oxygen across the pores via dissociative gas transport (an oxidation-reduction process).<sup>1, 2</sup>
- Water vapor can affect the plasticity of oxide scales. Some investigators propose that the plasticity of oxide scales is decreased and, consequently, the spalling of scales is increased.<sup>3</sup> Other investigators have proposed that plasticity of oxide scales is increased<sup>2, 4</sup> with increased oxidation rates<sup>2</sup> or improved adherence.<sup>4</sup>
- The presence of water vapor adversely affects the selective oxidation of elements such as aluminum and chromium from iron-base alloys.<sup>5</sup> It has also been found that water vapor affects the selective oxidation of aluminum from TiAl.<sup>6</sup>
- Water vapor can affect transport through oxides such as SiO<sub>2</sub> by causing the network structure to be changed.<sup>7</sup>
- Water vapor can cause the vaporization of some oxides to be increased because of the formation of hydrated species with high vapor pressures.<sup>8-10</sup>
- Water vapor causes the concentration of proton defects in oxide scales to be increased which can influence defect-dependent properties such as high temperature creep and diffusion.<sup>11, 12</sup>

The effects of water vapor on hot corrosion processes, and on mixed gas corrosion (e.g., in SO<sub>2</sub>-O<sub>2</sub>-SO<sub>3</sub> gas mixtures), have not been examined but, in view of the results obtained from

oxidation experiments, water vapor can be expected to influence these more complex high temperature corrosion processes.

Two of the most serious effects of water vapor or steam on the high temperature oxidation of alloys is the increased spalling tendencies of  $\text{Al}_2\text{O}_3$  and  $\text{Cr}_2\text{O}_3$  scales<sup>13</sup>, and the increased volatilization of certain oxides<sup>8-10</sup>. In this program  $\text{Al}_2\text{O}_3$  and  $\text{Cr}_2\text{O}_3$  scales are being emphasized because these two oxides are the basis for development of oxidation resistance in modern superalloys. Of course, as such alloys degrade, other oxides become important, but, usually, when oxides other than  $\text{Al}_2\text{O}_3$  or  $\text{Cr}_2\text{O}_3$  begin to predominate, the alloys' degradation rates are too high for continued service.

This program is directed at determining how high temperature and pressure steam affect the oxidation of materials proposed for use in current and advanced gas turbines. The approach is to first quantify how steam affects the oxidation of selected alloys and coatings by investigating the dependence of oxidation rates on temperature, steam pressure in air, and the gas mixture flow rates, and to then attempt to understand the changes in oxidation mechanisms that lead to the observed oxidation rate changes. The temperatures, steam pressures, and gas velocities being studied will extend over ranges that will permit results and conclusions to be applicable to dynamic operating conditions in gas turbines, but will also permit the oxidation processes to be understood because the conditions are well defined and controlled. Dynamic burner rigs will not be used. Testing is being performed in less simulative but more controlled environments. Three existing pieces of equipment are being used to investigate the oxidation of the selected alloys over the required ranges of conditions. The range of experimental conditions that can be established by these three apparatuses is summarized in Table I. Apparatus 1 is shown in Figure 1. It permits testing at steam pressures up to one atmosphere at temperatures up to 1100°C with gas velocities between 0.07 and 10 cm/s. Apparatus 2 is located at Oak Ridge National Laboratory. It permits testing at steam pressures greater than one atmosphere at temperatures between 700° and 1100°C at a flow rate of 0.07 cm/s. Apparatus 3 is shown in Figure 2 and is located at the University of Pittsburgh and permits testing at high gas velocities at temperatures between 700° and 900°C with steam pressures between 0.1 and 0.3 atm..

The compositions of the alloys being studied in this program are presented in Table II. All alloys will not be subjected to all tests. However, the testing of all alloys will be sufficiently extensive to describe and rank the alloys in steam at different temperatures and pressures. Aluminide coatings on CMSX 4 and on N5 will also be tested in this program.

This program consists of the following eight tasks that are being performed over a period of three years as indicated in Figure 3:

Task 1: Specimen Procurement

Task 2: Investigate the effects of steam pressure, gas flow rates, and temperature on the oxidation of selected alloys and coatings using Apparatus 1 at the University of Pittsburgh.

Task 3: Investigate the effects of high steam pressure (>1 atm) on the oxidation of selected alloys and coatings using Apparatus 2 at Oak Ridge National Laboratory.

Task 4: Investigate the effects of high gas velocities on the oxidation of selected alloys and coatings using Apparatus 3 at the University of Pittsburgh.

Task 5: Perform detailed analyses of all exposed specimens and formulate mechanisms for the degradation of alloys in steam.

Task 6: Investigate the effects of steam on the degradation of selected thermal barrier coatings.

Task 7: Investigate the effects of applied stresses on the oxidation of alloys in a steam-air mixture

Task 8: Communication and coordination of efforts and results with industrial partners and national laboratories.

The data generated will be used to study and resolve the following issues with regard to steam effects on the oxidation of turbine alloys and coatings:

1. Mechanisms will be developed to describe how water vapor influences the growth rates and adherence of alumina and chromia scales on superalloys/coatings.
2. The effect of temperature, over the ranges 700-1100°C (1292-2012°F) for alumina-forming alloys/coatings and 700-900°C (1292-1652°F) for chromia-forming alloys, on oxidation degradation will be determined.
3. The effect of water vapor partial pressure at pressures extending from 0.1 to about 15 atm on the degradation rates of superalloys/coatings will be described.
4. The effect of gas velocity (from 0.07 cm/s to Mach 0.5) on the degradation rates of superalloys/coatings will be described.
5. The oxidation behavior of the various alloys/coatings will be ranked under conditions simulating gas turbine operating conditions, and the effects of items 2 to 4 will be used to attempt to formulate life prediction models.
6. The technology and understanding developed in this program will be transferred to the industrial collaborators and other ATS participants.

**Discussion of Results  
Obtained During Current  
Report Period**

Task 1      Specimen Procurement

Sufficient quantities of the alloys and coatings to be used in this program have been obtained. The composition of the alloys being studied are given in Table II.

Task 2      Investigate the Effects of Steam Pressure, Gas Flow Rates, and Temperature on the Oxidation of Selected Alloys and Coatings Using Apparatus 1.

The experiments performed in Apparatus 1 have been used to compare the cyclic oxidation of a number of alloys at 900° and 700°C in dry and wet air ( $P_{H_2O} = 0.3\text{atm}$ ). In previous semi-annual reports<sup>(14,15)</sup> it was shown that the degradation of X-40, IN 738, Mar M 247, N5 and CM 186 at 900°C was more severe in wet air compared to dry air. For these alloys the cracking and spalling of the oxide scales was more severe in wet air. In the case of PWA 1484 significant attack was observed in wet air at 900°C, but substantial attack was also observed in localized areas in dry air, Figure 4. Inspection of the scanning micrographs for PWA 1484 specimens exposed in dry air show, Figure 4a, that a continuous  $\alpha\text{-Al}_2\text{O}_3$  scale did not develop in some areas and consequently oxide pits developed. In wet air a continuous  $\alpha\text{-Al}_2\text{O}_3$  did eventually develop, Figure 4b, and localized pits were not observed. The large oxide pits that formed in dry air may be due to localized composition changes that were present only in the specimen tested in dry air.

In the current report period results are presented for the cyclic oxidation of CM 186, N5, PWA 1484, IN 738 X-40 and Mar M 247 in dry air and wet air at 700°C. Weight change versus time data for the cyclic oxidation of PWA 1484 in wet and dry air at 900° and 700°C are compared in Figure 5. The weight changes are very large for the cyclic oxidation of PWA 1484 at 700°C in wet air. Scanning micrographs showing specimens of this alloy after exposure at 700°C in dry and wet air are presented in Figure 6. Significant internal oxidation in both dry and wet air is evident, however in dry air an external scale of Cr<sub>2</sub>O<sub>3</sub> has developed, Figure 6a, but in wet air a continuous layer of Cr<sub>2</sub>O<sub>3</sub> has not developed and a thick scale containing nickel and cobalt has been formed, Figure 6b. As will be discussed for some of the other alloys subsequently, the alumina-forming alloys such as PWA 1484 and N5 become less effective in developing continuous layers of alumina as the oxidation temperature is decreased and steam exacerbates this condition.

Data comparing the cyclic oxidation of N5 in dry and wet air at 900°C and 700°C are presented in Figure 7. The weight changes are small and scanning micrographs of exposed specimens must also be considered when comparing oxidation-induced degradation. In Figures 8 and 9 scanning micrographs are presented to compare the degradation of N5 after cyclic oxidation at 900°C in dry air, Figure 8, and in wet air, Figure 9. More severe oxidation is evident in wet air where thicker scales are formed before the α-Al<sub>2</sub>O<sub>3</sub> develops continuity, Figure 9. Scanning micrographs showing N5 specimens after cyclic oxidation at 700°C in dry and wet air are presented in Figures 10 and 11, respectively. It appears that most of the external oxide scales have spalled from the specimens. Internal oxidation is evident in both specimens exposed in dry and wet air. This internal oxidation occurs where phases rich in refractory elements (e.g. Ta, W) are present in the superalloy. Such attack is more extensive in wet air and the attack also extends deeper in the alloy for wet air conditions. The reason that alumina is formed along the boundaries of the refractory metal rich phases is not understood. Evidently oxygen must have access along the boundaries of this phase and the alumina that is formed must not block this access.

The cyclic oxidation behavior of both CM 186 and Mar M 247 at 700°C was similar to that described previously for N5 and PWA 1484. Weight change versus time data in wet air was greater at 700°C compared to 900°C, Figures 12, 13 and 14. Substantial amounts of oxidation were evident at both 900° and 700°C as is evident for Mar M 247 in Figures 15, 16, 17 and 18 but it was not possible to always observe less attack at 900°C compared to 700°C. However, at both temperatures more degradation was always evident in wet conditions compared to dry. Internal oxidation of aluminum tended to be greater at 700°C compared to 900°C and often this internal oxidation was associated with refractory metal rich phases in these alloys as shown in Figure 17 for Mar M 247 exposed to cyclic oxidation conditions using dry conditions at 700°C.

As discussed in previous reports both X-40 and IN 738 were severely degraded during cyclic oxidation in wet air at 900°C. These two alloys were not degraded substantially during cyclic oxidation at 700°C and there was not a significant difference between cyclic oxidation in wet and dry air, Figures 19, 20 and 21.

**Task 3      Investigate the Effects of High Pressure Steam on the Oxidation of Selected Alloys and Coatings Using Apparatus 2**

All of the specimens that have been exposed to 250 psi steam at 700°C and 900°C have been examined metallographically with the exception of those specimens that are planned to be exposed longer times at 900°C and 250 psi. As discussed previously high pressures of steam do not appear to have caused increased degradation. For example, scanning micrographs of Mar M 247 after exposure to 250 psi of steam at 700°C and 900°C are presented in Figures 22 and 23. These micrographs can be compared to those presented in Figures 16 and 18 where there is not a substantial difference in the amount of oxidation.

**Task 4      Investigate the Effects of High Gas Velocities on the Oxidation of Selected Alloys and Coatings Using Apparatus 3**

Results obtained previously in this program have not shown any effect of gas velocity on the oxidation of alloys in dry air. Some difficulty has been experienced in obtaining gas velocities of about 100 m/s at a temperature of 900°C. Since a substantial amount of data has been obtained at 700°C in cyclic oxidation tests and isothermally at a steam pressure of 250 psi, the high gas velocity experiments are to be performed at 700°C in dry and wet air. These experiments will be completed in the next six months of this program.

**Task 5      Perform a Detailed Analysis of All Exposed Specimens and Formulate Mechanisms for the Degradation of Alloys in Steam**

The evaluation of exposed alloys is continuing and as has been discussed in previous reports, mechanisms are being developed to account for the behavior of the various alloys in steam environments at 900°C and 700°C.

All of the alloys that have been studied exhibited more severe oxidation at 900°C in wet air compared to dry air. Water vapor caused the oxide scales to crack and spall during cyclic oxidation testing. The alloys X-40 and IN 738 were more severely degraded compared to PWA 1484, N5 and CM 186. This is believed to occur due to the presence of thicker scales on the former alloys which rely on Cr<sub>2</sub>O<sub>3</sub> scales for oxidation protection compared to the latter alloys which develop α-Al<sub>2</sub>O<sub>3</sub> scales during oxidation.

At 700°C adverse effects on oxidation behavior were observed for exposures in water vapor but α-Al<sub>2</sub>O<sub>3</sub> scales were not formed on alloys such as PWA 1484, CM 186 and Mar M 247 and water vapor as well as the lower temperature inhibited the selective oxidation of aluminum in these alloys. Since Cr<sub>2</sub>O<sub>3</sub> developed on X-40 and IN 738 these alloys were not adversely affected at 700°C.

The conditions that caused the most severe degradation of all of these alloys were the combined presence of water vapor and cyclic oxidation conditions. The steam pressure did not appear to be an important factor. However, the high pressure experiments were performed under isothermal conditions. The results obtained did not indicate more severe oxidation because of the high steam pressure.

Task 6      Studies to Examine the Effects of Steam-Air Gas Mixtures on the Degradation of Thermal Barrier Coatings

As discussed in the previous annual report for this program, by using an indent test<sup>(16)</sup>, results were obtained that suggested the fracture toughness loss of thermal barrier coatings exposed at 1100°C was greater for the case of exposure in water vapor (air with  $P_{H_2O} = 0.1\text{atm}$ ) compared to dry air. Additional TBCs have been tested where the as processed TBCs had the same initial fracture toughness. A significant effect of water vapor was not observed in these tests. Work is continuing to attempt to determine the variation of fracture toughness in as processed TBCs, and the effectiveness of steam on the loss of fracture toughness with exposure of such specimens to oxidizing conditions at 1100°C.

Task 7      Investigate the Effects of Externally Applied Stress on the Oxidation of Alloys in Steam

A fixture has been prepared, Figure 24, whereby a specimen can be bent and exposed to oxidizing conditions. The alloy used in this experiment was Alfa 4, an Fe-Cr-Al alloy upon which continuous scales of  $\alpha\text{-Al}_2\text{O}_3$  are formed during oxidation. The thickness and length of the specimens were such that the stresses developed at the point of maximum curvature were less than the yield strength of Alfa 4 at 1000°C. Two specimens were exposed in this fixture at 1000°C for 100 hrs isothermally. One was exposed in dry air, the other in air with water vapor ( $P_{H_2O} = 0.3\text{atm}$ ). The specimens crept at temperature and consequently the stress in the specimens were relieved. No effect of the stresses in the specimens upon the oxidation of the alloy was evident. As shown in Figure 25, more spalling of oxide was evident on the specimens exposed in wet air. These exposed specimens will be examined metallographically to determine if the oxide thickness varies along the specimen length where at least initially there was a stress gradient.

Task 8      Communication and Coordination of Efforts and Results with Industrial Partners and National Laboratories

The PIs are collaborating with the investigators at Oak Ridge National Laboratory and results are being distributed via reports.

#### Summary and Plan for Next Six Months of the Program

In this program it has been found that the major effects of steam or water vapor on the oxidation of superalloys is to cause increased cracking and spalling of oxide scales and to inhibit the selective oxidation of elements such as aluminum. The cracking and spalling of oxide scales becomes more severe as temperature increases whereas the inhibition of selective oxidation becomes more of a problem as temperature is decreased. Over the next six months work will be directed upon completing all of the technical tasks in this program. This will include examining the specimens that are to be exposed at a steam pressure of 250 psi, continuing work on TBC

failures in steam, and examining the effect of gas velocity on oxidation in the presence of water vapor.

### References

1. A. Rahmel and J. Tobolski, Corros. Sci., 5, 33 (1965).
2. C. W. Tuck, M. Odgers, and K. Sachs, Corros. Sci., 9, 271 (1969).
3. R. L. McCarron and J. W. Shulz, "The Effects of Water Vapor on the Oxidation Behavior of Some Heat Resistant Alloys," Proc. of Symposium on High Temperature Gas-Metal Reactions in Mixed Environments, AIME, New York, 1973, p. 360.
4. H. Bouaouine, F. Armanet, and C. Coddet International Congress on Metallic Corrosion, Toronto, Canada, 1989, p. 379.
5. I. Kvernes, M. Oliveira, and P. Kofstad, Corros. Sci., 17, 237 (1977).
6. R. Kremer and W. Auer, Materials and Corrosion, 48, 35 (1997).
7. E. A. Irene, J. Electrochem. Soc., 121, 1613 (1974).
8. J. F. Cullinan, "The Oxidation of Carbon-Carbon Composites between 300°C and 900°C in Oxygent and Oxygen/Water Vapor Atmospheres," M.S. Thesis, University of Pittsburgh, 1989.
9. E. J. Oplia and R. E. Hann, J. Amer. Ceram. Soc. 80, 197 (1997).
10. J. L. Smialek, R. C. Robinson, E. J. Opika, D. S. Fox and N. S. Jacobson, Adv. Composite Mater., 8, 33 (1999).
11. A. J. Sedriks, "Corrosion of Stainless Steels," 2<sup>nd</sup> Edition, John Wiley and Sons, Inc., New York, 1996.
12. P. Kofstad, in Microscopy of Oxidation, M. J. Bennett and G. W. Lorimer, eds., The Institute of Metals, London, 1991, p. 2.
13. R. Janakiraman, G. H. Meier, and F. S. Pettit, Metall. and Mater. Trans. A, 30A, 2905 (1999).
14. G. H. Meier, F. S. Pettit, and K. Onal, "Interaction of Steam/Air Mixtures with Turbine Airfoil Alloys and Coatings", Semi-Annual Report on AGTSR Subcontract No. 99-01-SR077, University of Pittsburgh, September 1, 2000.
15. G. H. Meier, F. S. Pettit and K. Onal, "Interaction of Steam/Air Mixtures with Turbine Airfoil Alloys and Coatings", Semi-Annual REport on AGTSR Subcontract No. 99-01-SR077, University of Pittsburgh, March 5, 2001.
16. A. Vasinonta and J. L. Beuth, "Measurement of Interfacial Toughness in Thermal Barrier Coating Systems by Indentation", *Engineering Fracture Mechanics*, in print.

Table 1

Experimental Conditions to be Established by the Three Apparatuses to be Used in the Program

	Apparatus 1	Apparatus 2	Apparatus 3
Temperature	700°C - 1100°C	700°C - 1100°C	700°C - 900°C
Steam Pressure Range	0.1 – 1 atm	0.1 – 20 atm	0.1 – 0.3 atm
Gas Velocity Range	0.07 – 10 cm/s	0.07 – cm/s	50 – 150 m/s

Table 2

Composition in Weight Percent

Alloy	Ni	Cr	Al	Co	Ta	W	M <sub>o</sub>	Ti	B	C	Hf	Zr	Nb	Re
IN 738	Bal	16.0	3.4	8.5	1.7	2.6	7.1	3.4	0.001	0.11		0.05	0.9	
X-40	10	25.5		Bal		7.5				0.5				
CM186	Bal	6.6	5.7	9.2	3.2	8.5	0.5	0.7	0.01	0.07	1.4			
Mar M247	Bal	8.2	5.4	9.9	3.0	9.8	0.7	1.05	0.01	0.13	1.3	0.4	0.2	
CMSX-4	Bal	6.5	5.6	9.0	6.5	6.0	0.6	1.0			0.1			3.0
N5	Bal	7.0	6.2	7.5	6.5	6.0	1.0				0.1			3.0
PWA1484	Bal	5.0	5.6	10.0	8.7	6.0	2.0				0.1			3.0

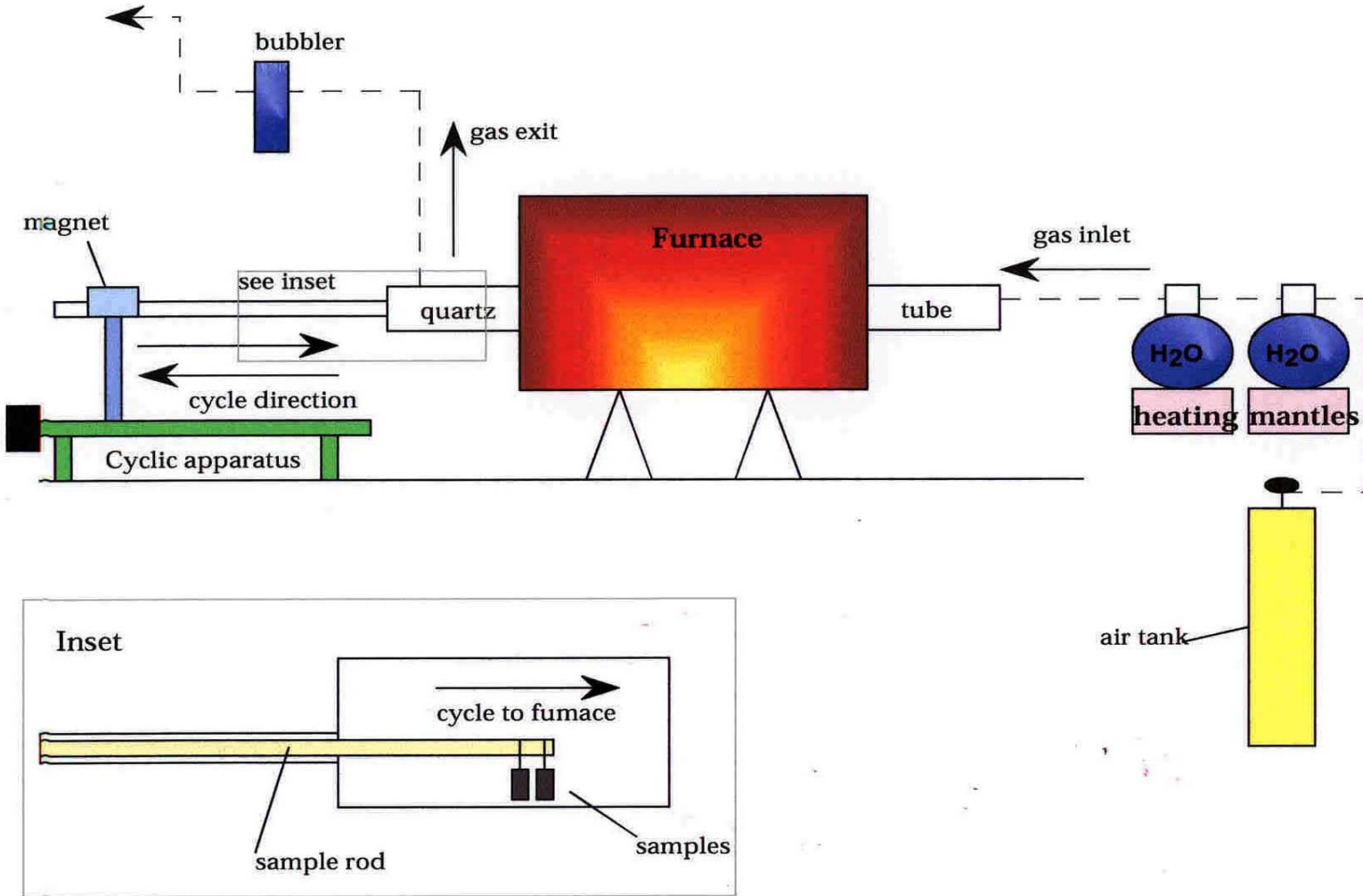


Figure 1. Schematic diagram to show the apparatus to cyclically oxidize coupon specimens in gases with defined and controlled amounts of water vapor.

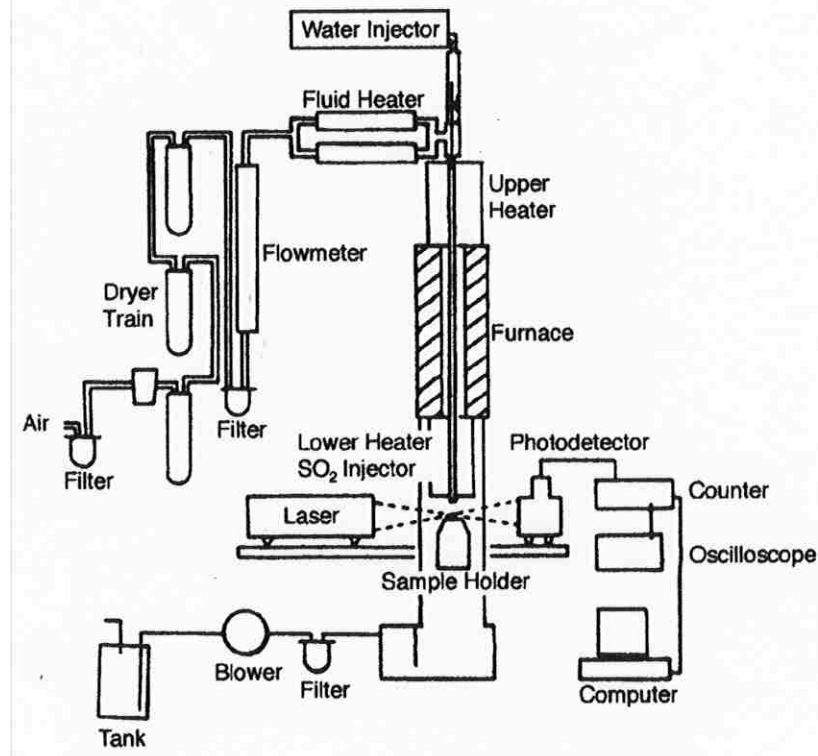


Figure 2. Schematic diagram showing apparatus 3 in which specimens can be oxidized at 700°C and 900°C in steam-air mixtures (total pressure 1 atm.) at gas velocities up to 150 m/s. The laser is used to measure gas velocities by adding Al<sub>2</sub>O<sub>3</sub> to the gas stream.

	Year 1	Year 2	Year 3
<b>Task 1</b> Specimen Procurement	→		
<b>Task 2</b> Determine Effects of Steam Pressure, Gas Flow Rate and Temperature on Oxidation of Alloys in Apparatus 1	→	→	
<b>Task 3</b> Investigate the Effects of High Steam Pressure on the Oxidation of Alloys Using Apparatus 2	—	—	→
<b>Task 4</b> Investigate the Effects of High Gas Velocities on the Oxidation of Alloys in Steam-Air Mixture Using Apparatus 3	—	—	→
<b>Task 5</b> Detailed Analysis of Results and Formulation of Mechanisms for Oxidation of Alloys in Steam Under Simulated Dynamic Conditions	—	—	→
<b>Task 6</b> Studies to Examine the Effects of Steam-Air Mixtures on the Degradation of Thermal Barrier Coatings			→
<b>Task 7</b> Investigate the Effects of Applied Stresses on the Oxidation of Alloys in a Steam-Air Mixture			→
<b>Task 8</b> Coordination with Industrial Partners and National Laboratories	—	—	→

**Figure 3.** Proposed schedule for the eight tasks in the program

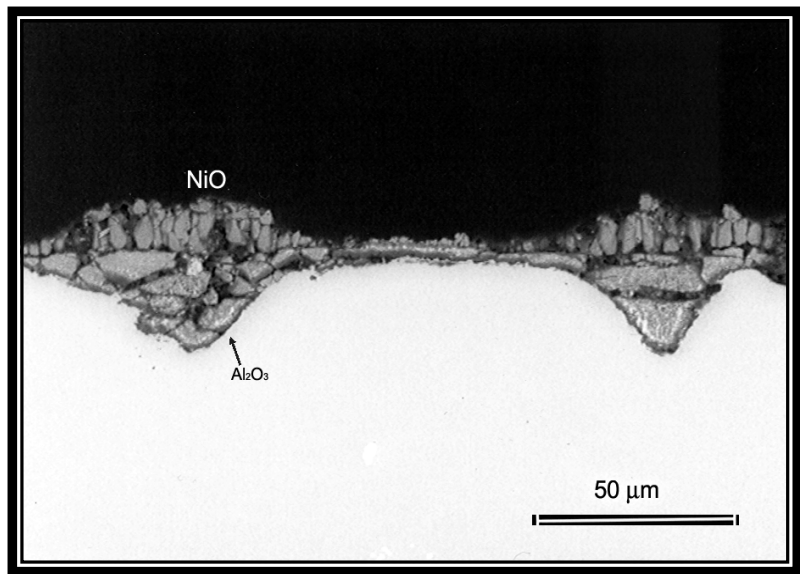


Figure 4 a. SEM micrograph of PWA 1484 at 900°C in dry air after 3200 cycles (2400 hr hot time)

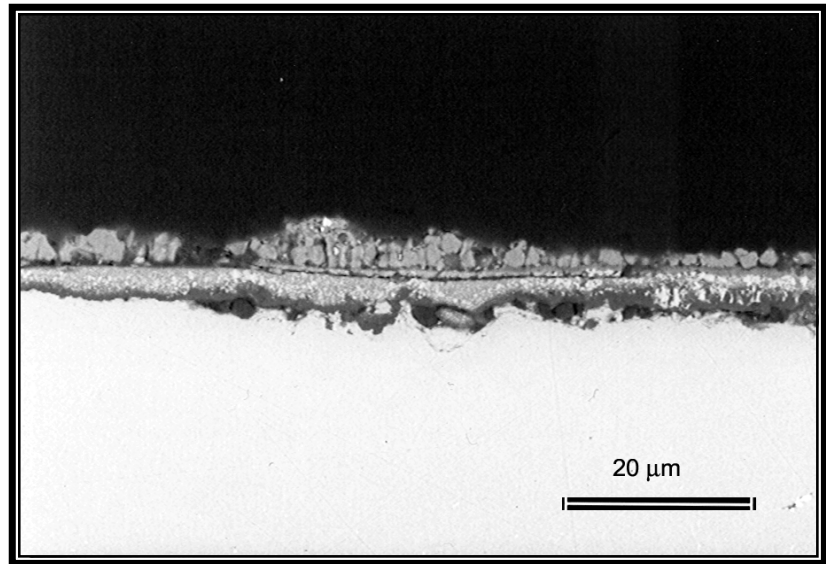
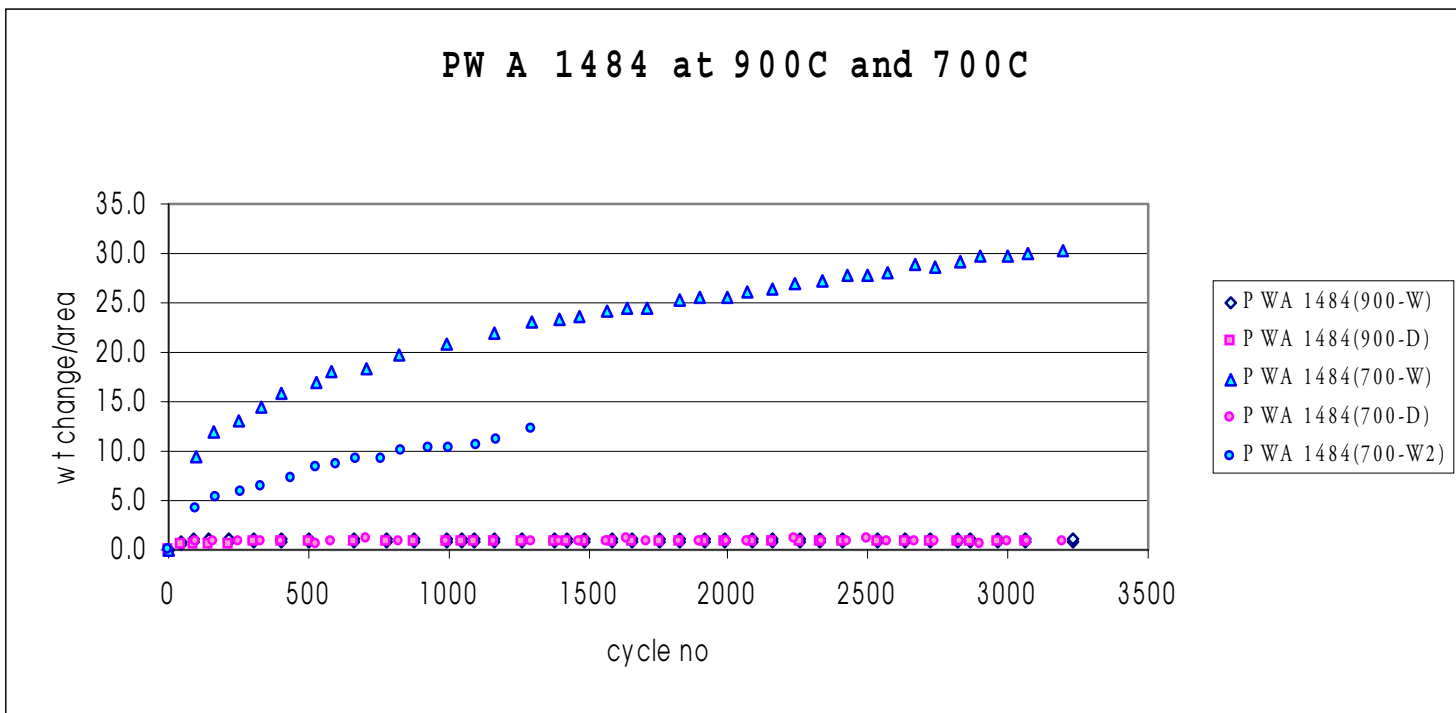


Figure 4 b. SEM micrograph of PWA 1484 at 900°C in air with  $P_{H_2O} = 0.3$  atm after 3200 cycles



**Figure 5. Weight change vs time plot for the alloy PWA 1484 at 700C and 900C.**

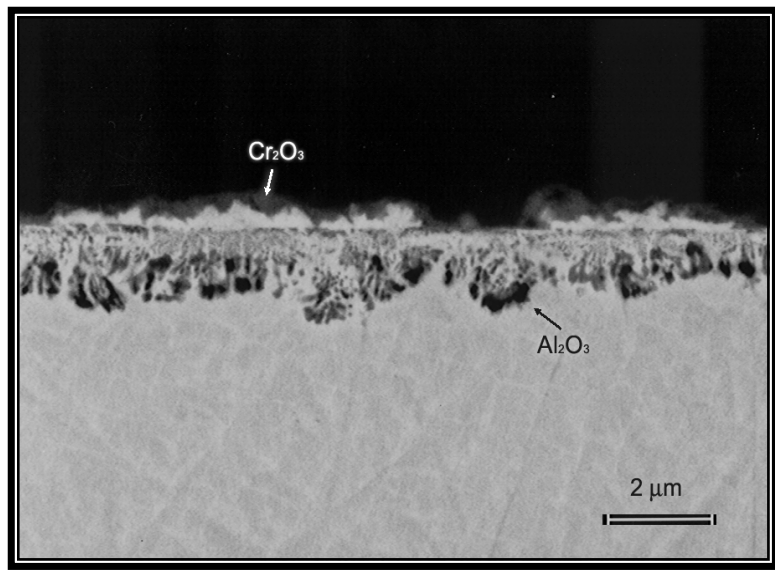


Figure 6 a. SEM micrograph of PWA 1484 at  $700^\circ\text{C}$  in dry air after 3200 cycles

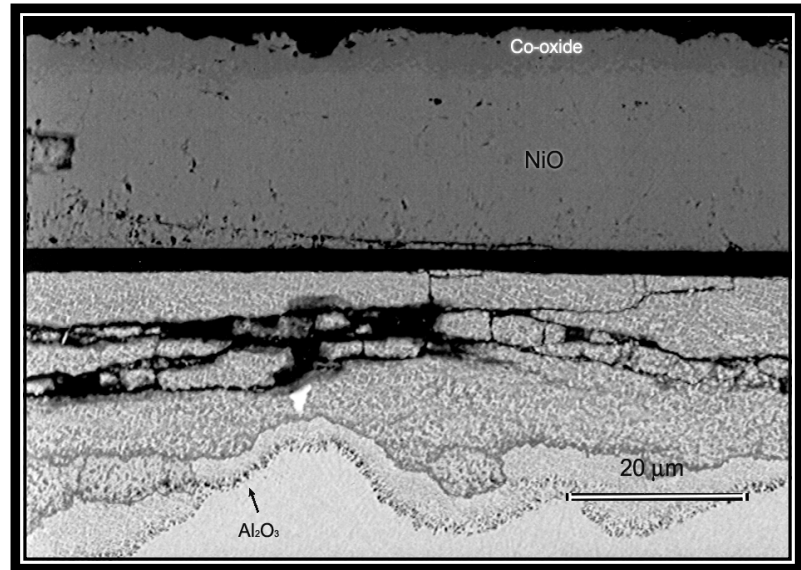
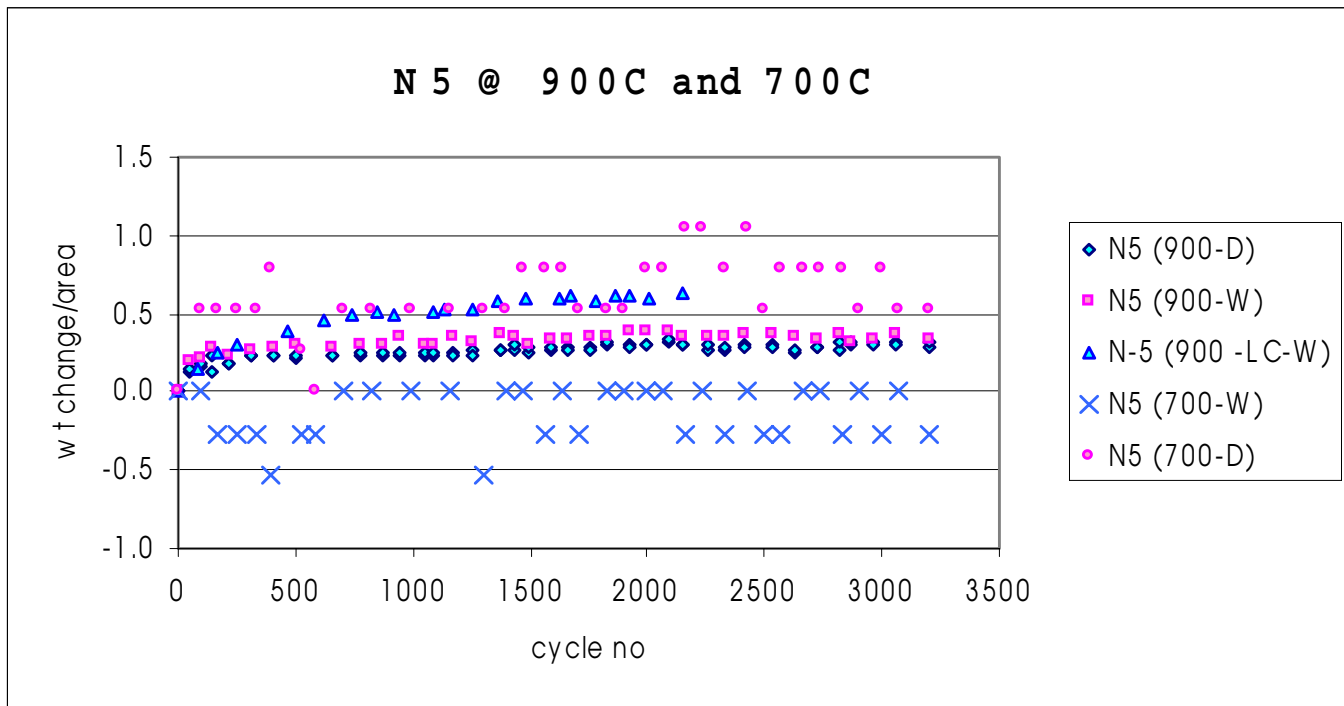


Figure 6 b. SEM micrograph of PWA 1484 at  $700^\circ\text{C}$  in air with  $P_{\text{H}_2\text{O}} = 0.3 \text{ atm}$  after 3200 cycles



**Figure 7. Weight change over time plots for the alloy N5 at 700C and 900C.**

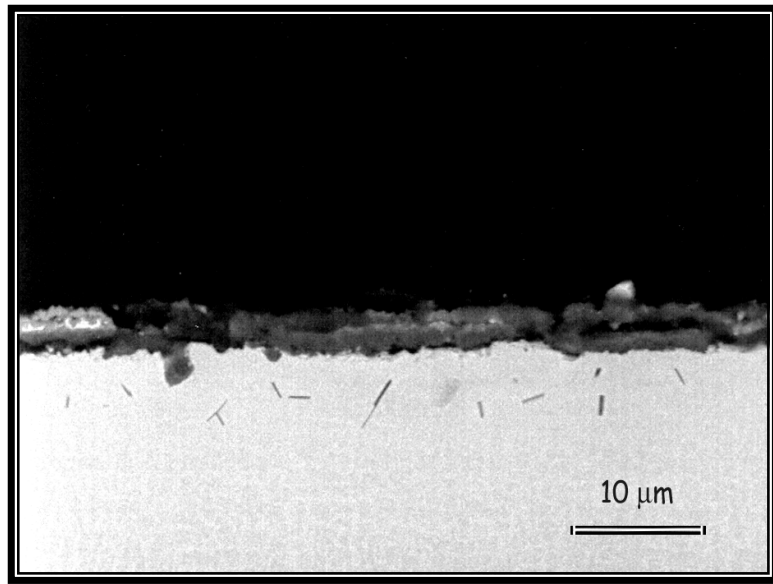


Figure 8. SEM micrograph of N5 at 900C in dry air after 3200 cycles

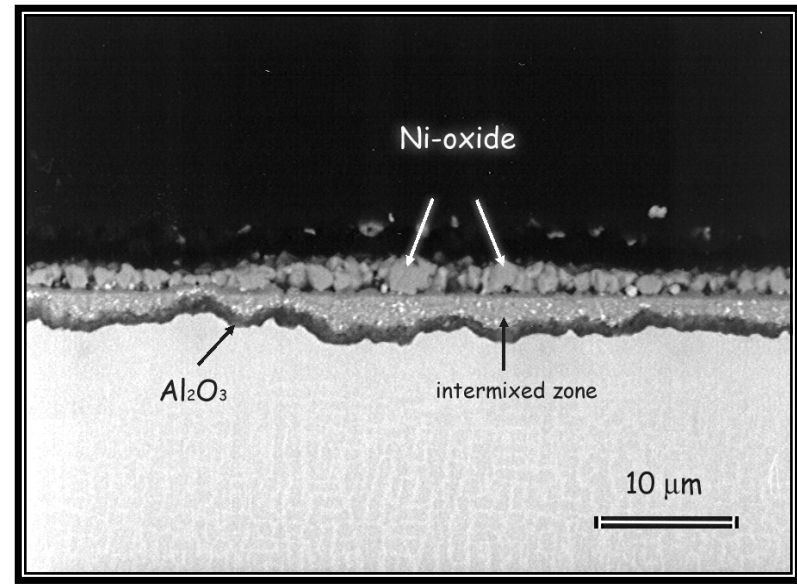


Figure 9. SEM micrograph of N5 at 900C in wet air after 3200 cycles

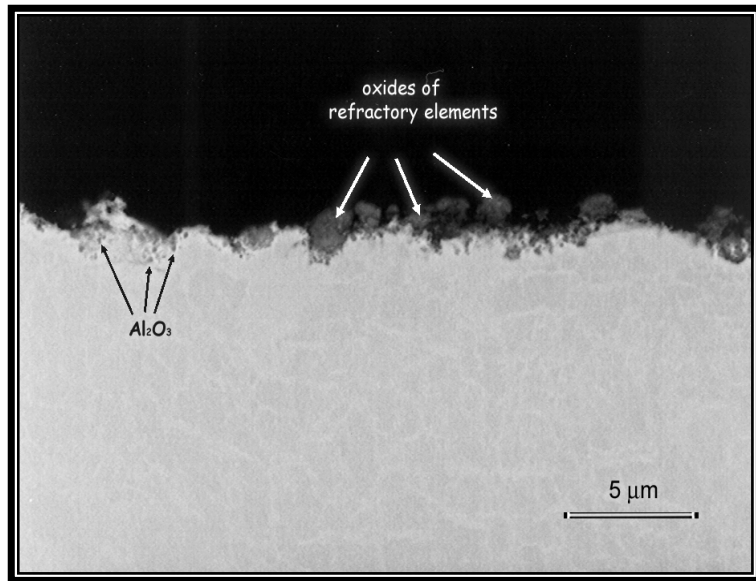


Figure 10. SEM micrographs of N5 at 700C in dry air after 3200 cycles

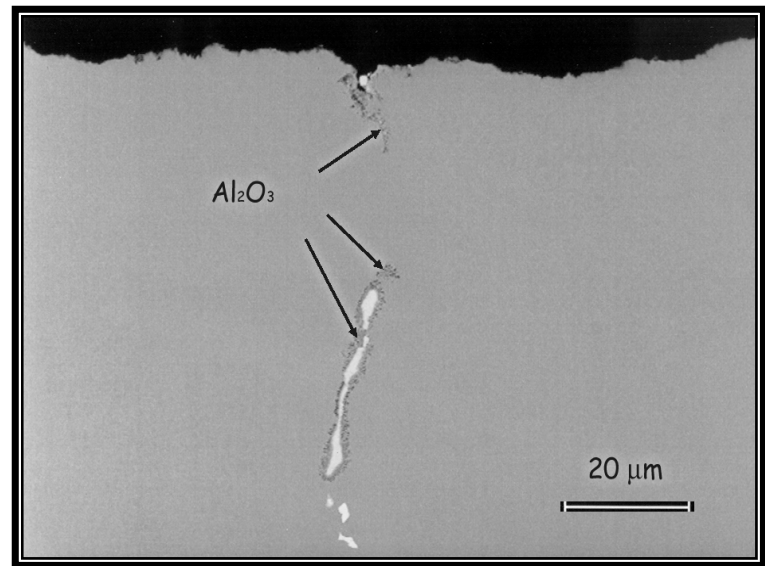
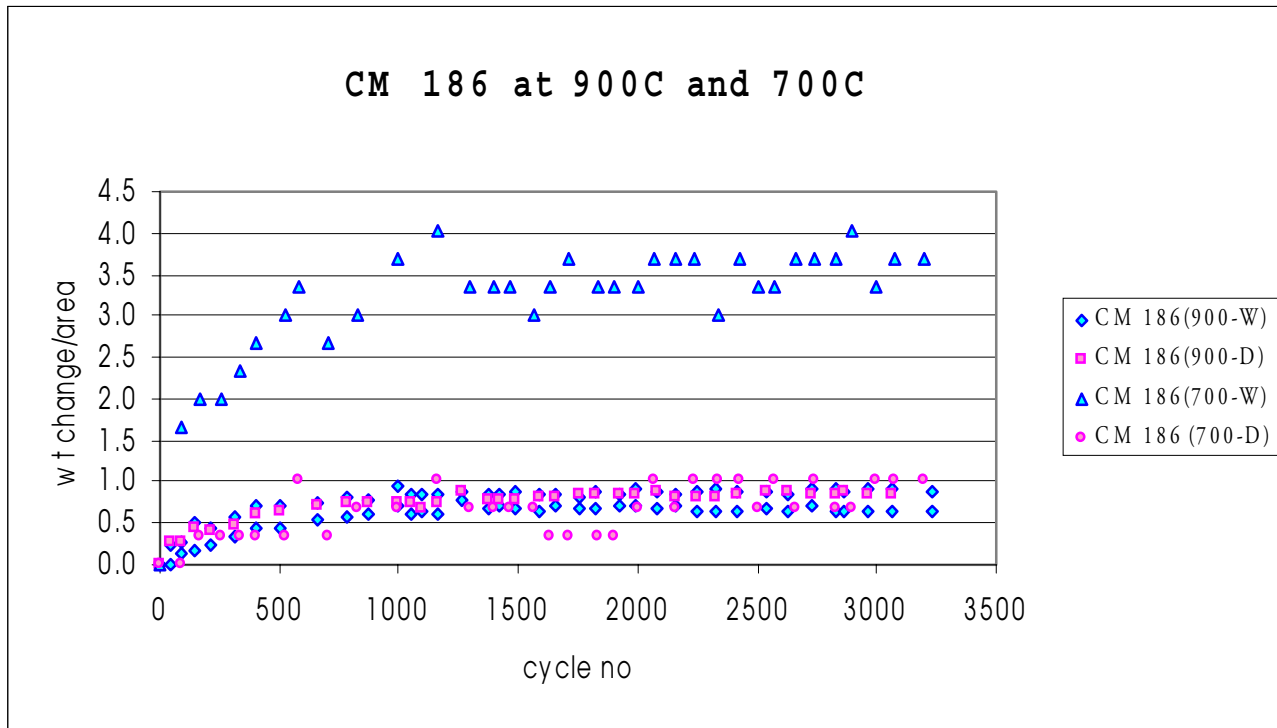


Figure 11. SEM micrographs of N5 at 700C after 3200 cycles in wet air



**Figure 12. Weight change vs time plot for the alloy CM186 at 700C and 900C**

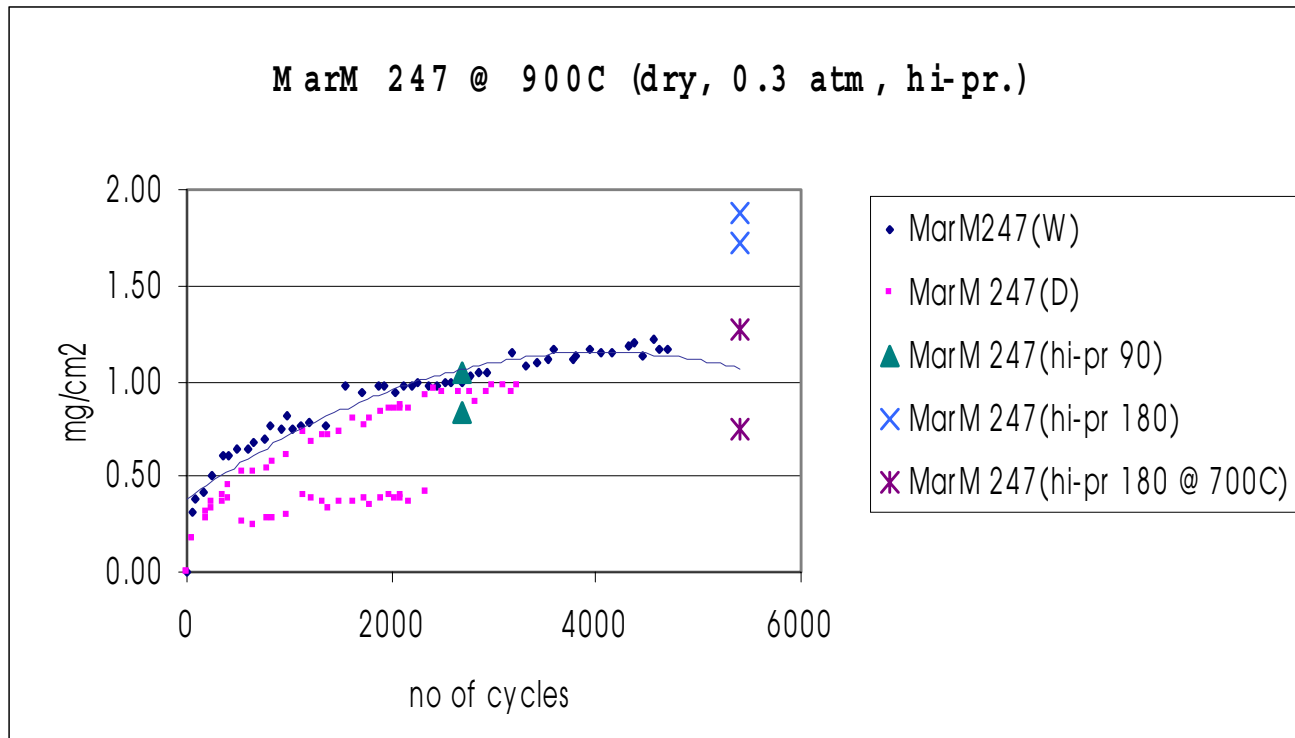


Figure 13. Weight change vs time plot for the alloy  
MarM 247 at 900C.

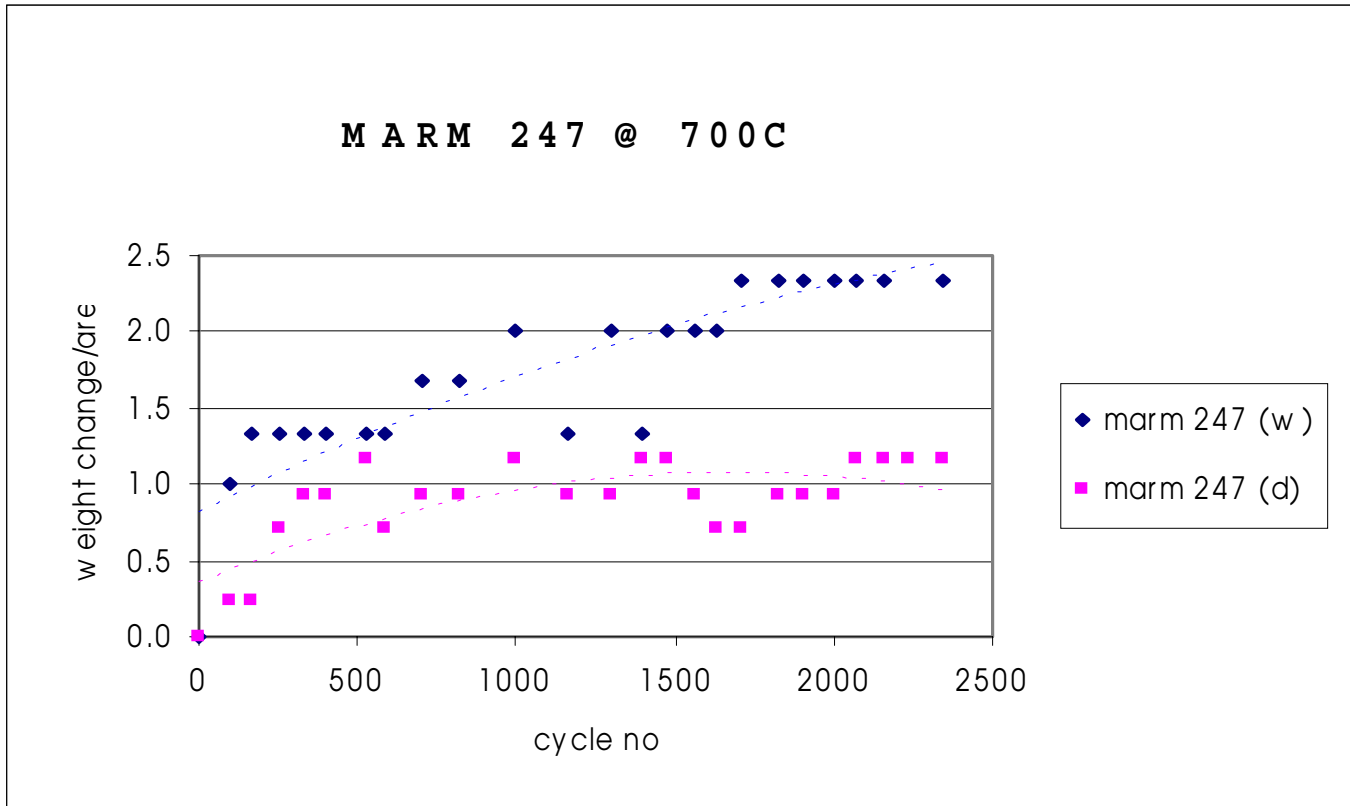


Figure 14. Weight change vs time for the alloy  
MarM 247 at 700C.

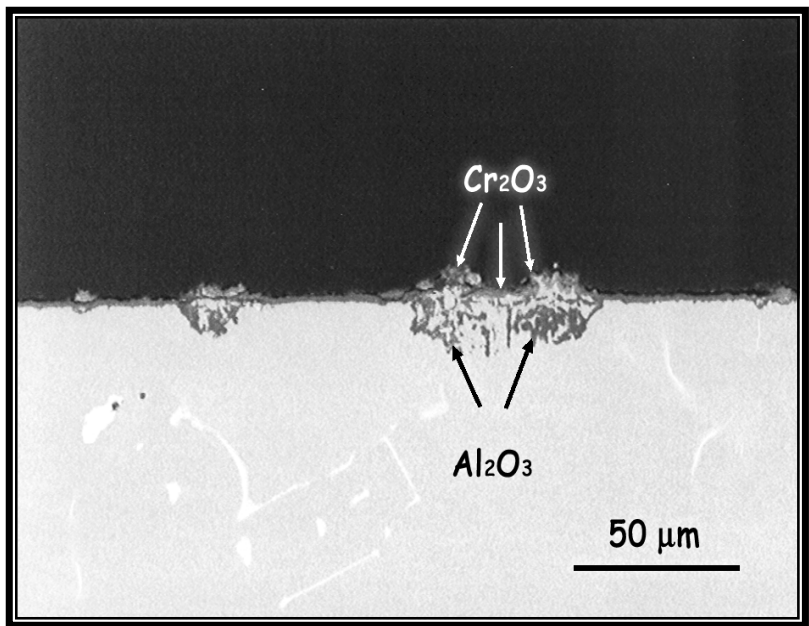


Figure 15. MarM 247 at 900C in dry air after 2340 cycles

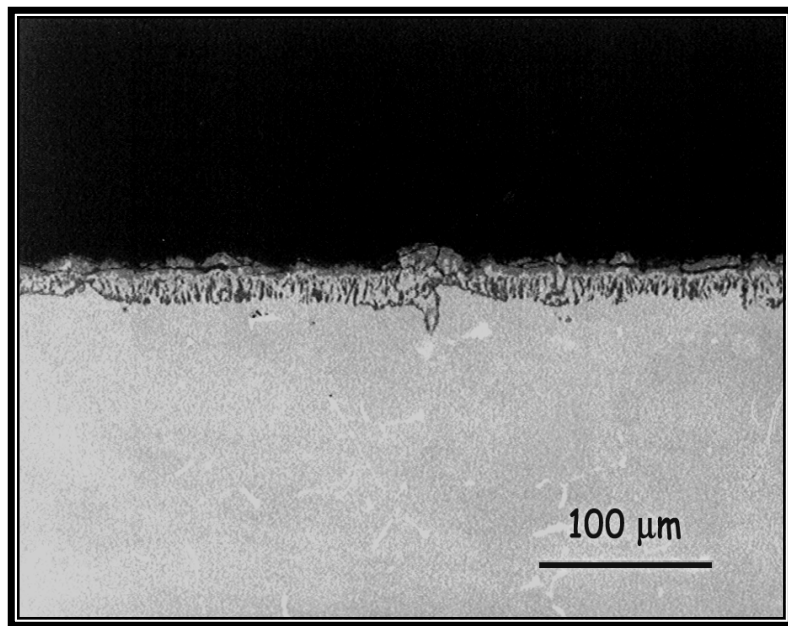


Figure 16. MarM 247 at 900C in wet air after 2340 cycles

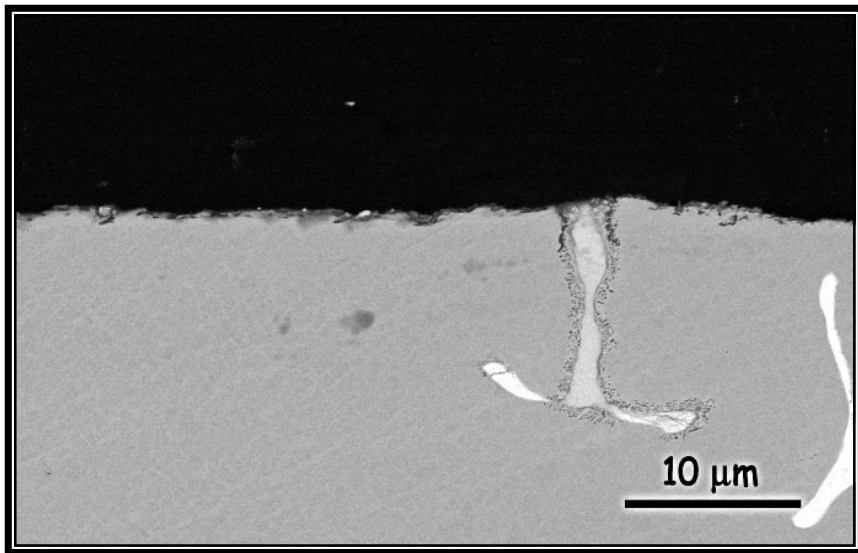


Figure 17. Marm 247 at 700C in dry air after 2340 cycles

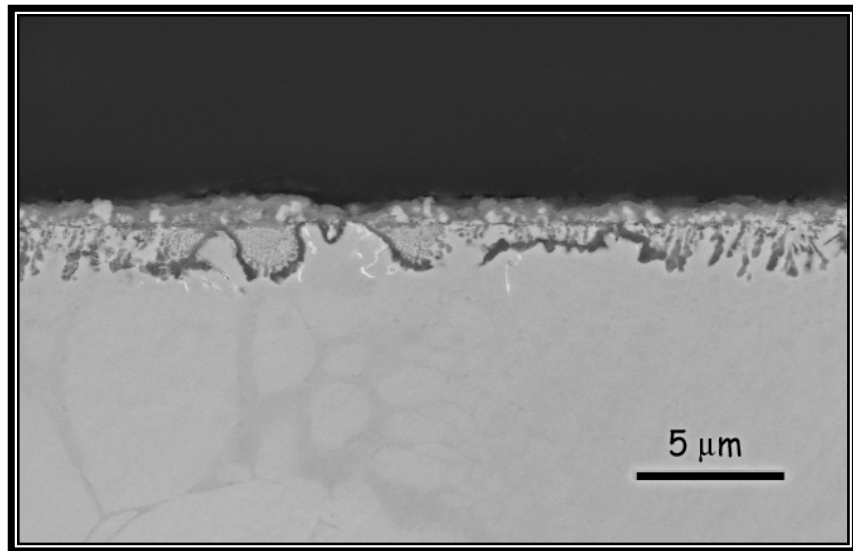


Figure 18. MarM 247 at 700C in wet air after 2340 cycles

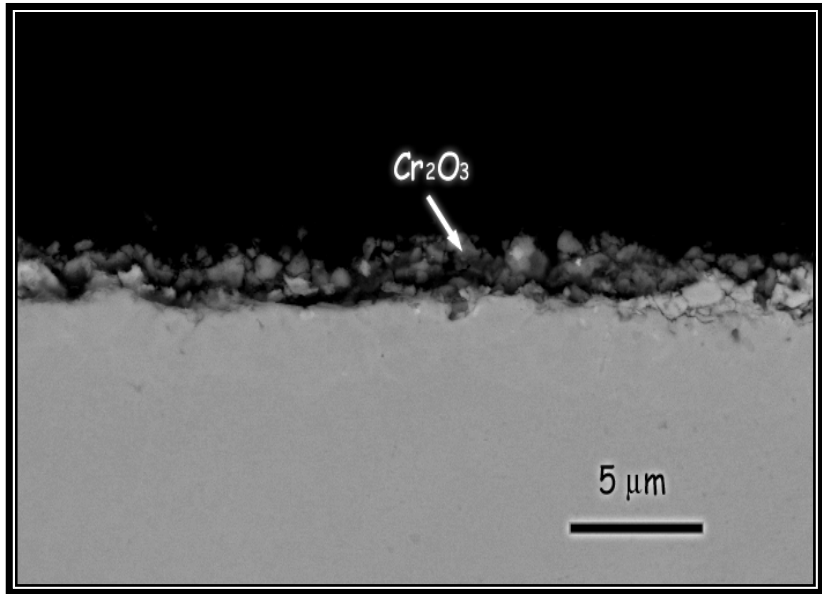


Figure 19. X-40 at 700C in dry air  
after 3200 cycles

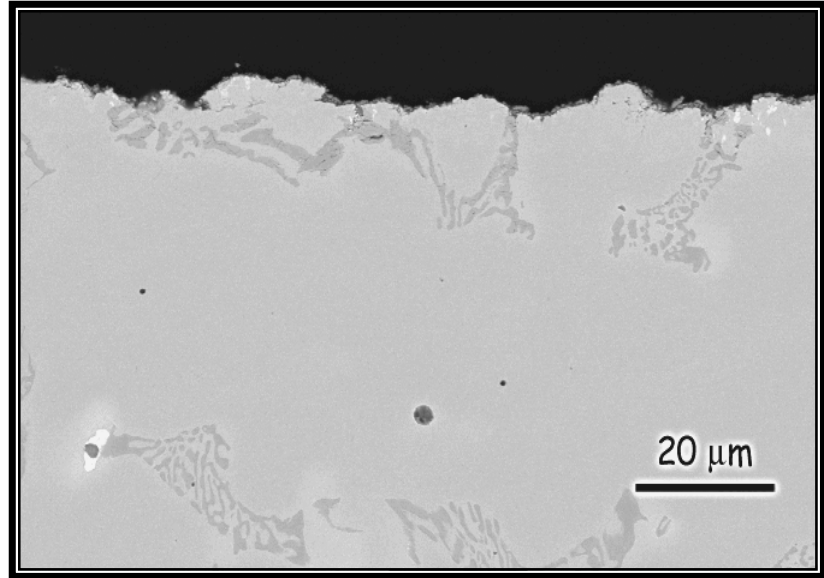


Figure 20. X-40 at 700C in wet air  
after 3200 cycles

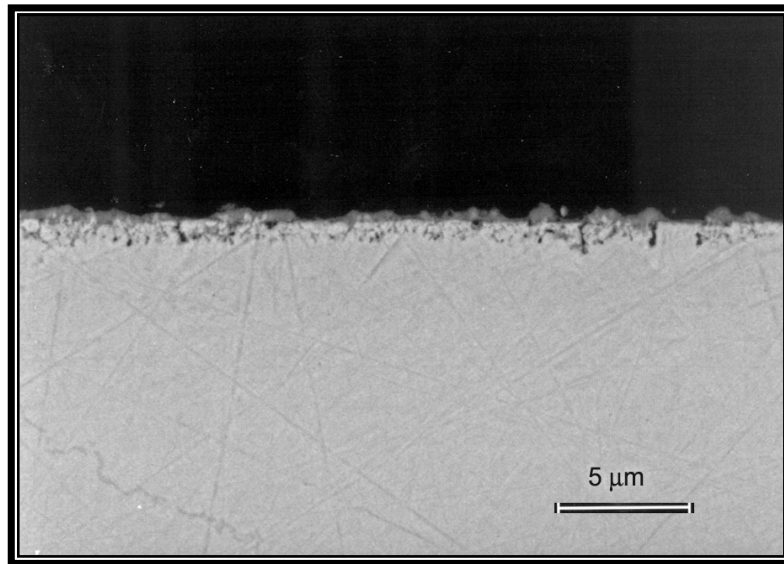


Figure 21. SEM micrograph of IN 738 at 700°C in dry air after 2520 cycles (1890 hr hot time)

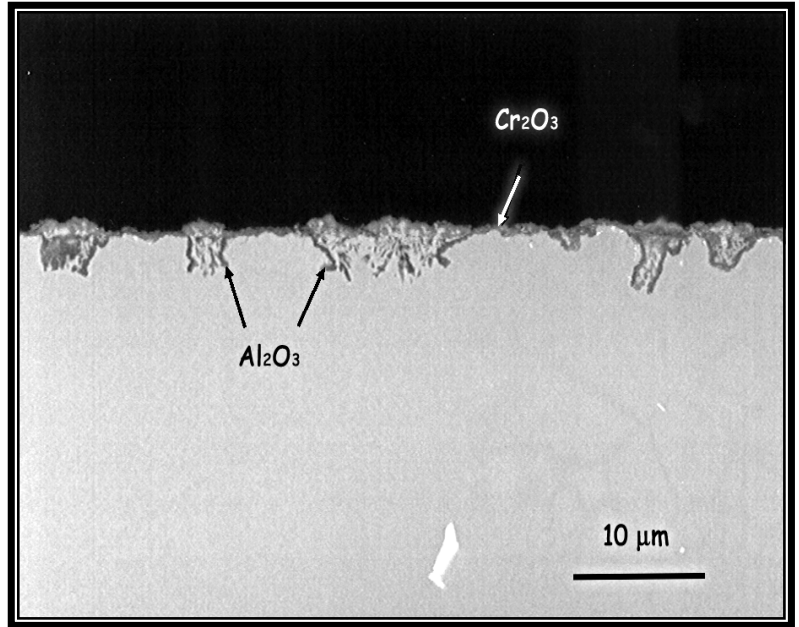
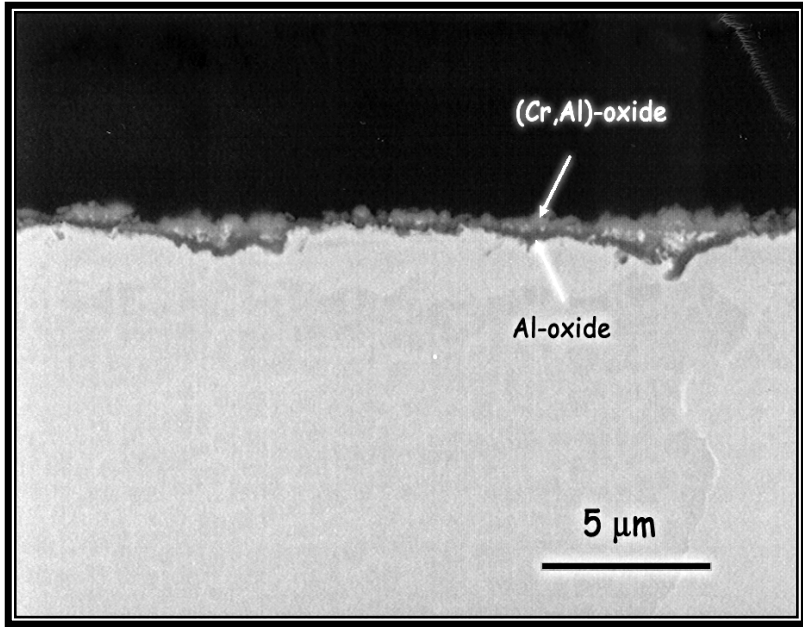


Figure 22. MarM 247 at 700C in 100% steam at 250 psi after 180 days

- continuous protective scale predominates
- some internal oxidation is also observed

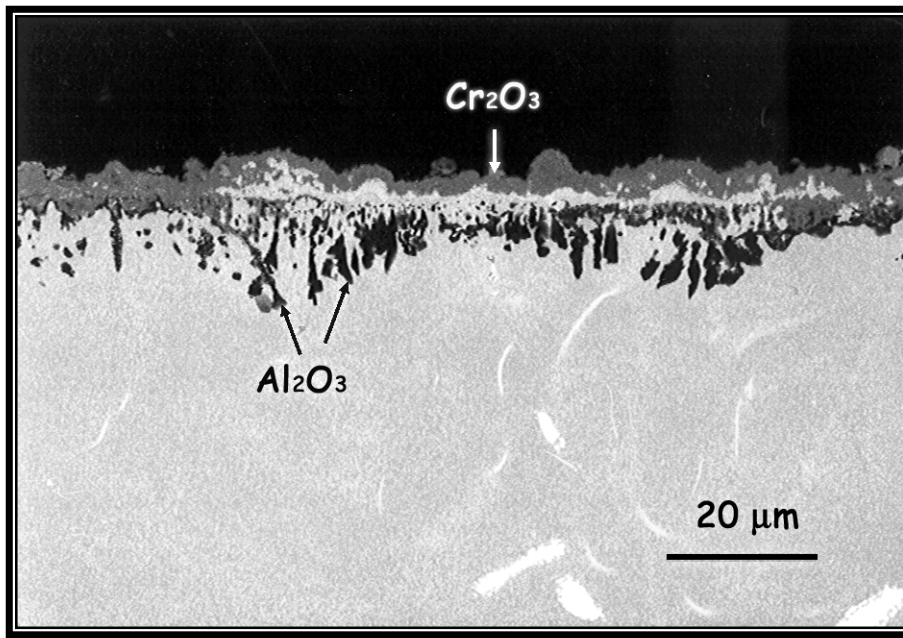


Figure 23. MarM 247 at 900C in 100% steam at 250 psi  
after 180 days

- chromia forms a protective external scale
- internal alumina formation

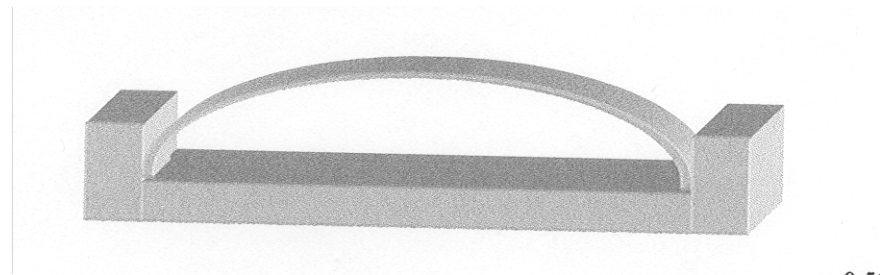


Figure 24. Fixture to perform oxidation test on stressed specimens

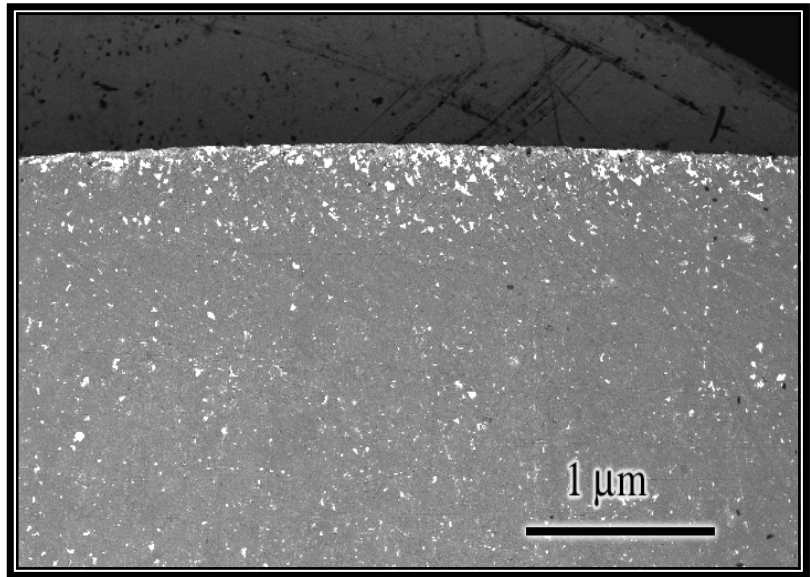
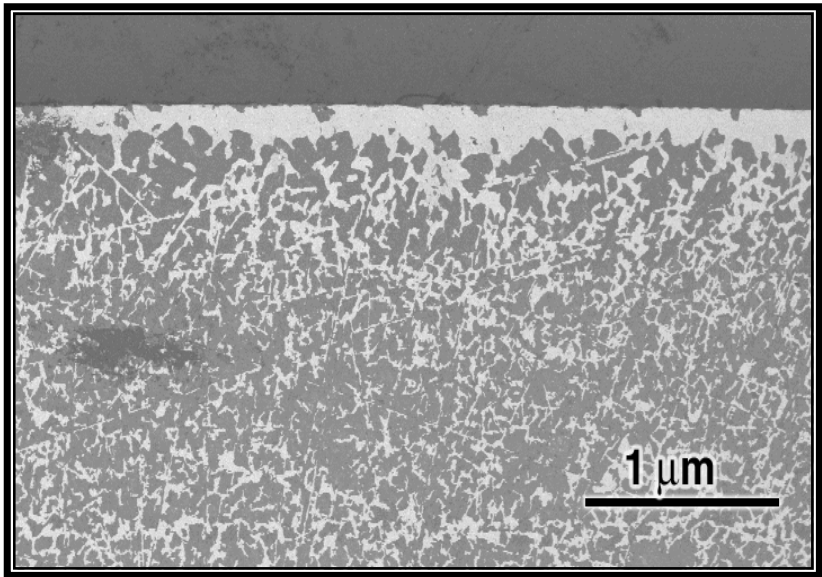


Figure 25. Exposed alfa 4 in wet (left) and dry (right) air.